



**Jorge Virgilio de Almeida**

**Data and Power Transmission for Underwater  
Monitoring Systems Using Metamaterials**

**Tese de Doutorado**

Thesis presented to the Programa de Pós-graduação em Engenharia Elétrica of PUC-Rio in partial fulfillment of the requirements for the degree of Doutor em Engenharia Elétrica.

Advisor: Prof. Eduardo Costa da Silva

Co-advisor: Prof. Carlos Antonio França Sartori

Rio de Janeiro  
April 2021



**Jorge Virgilio de Almeida**

**Data and Power Transmission for Underwater  
Monitoring Systems Using Metamaterials**

Thesis presented to the Programa de Pós-graduação em Engenharia Elétrica of PUC-Rio in partial fulfillment of the requirements for the degree of Doutor em Engenharia Elétrica. Approved by the Examination Committee:

**Prof. Eduardo Costa da Silva**

Advisor

Departamento de Engenharia Elétrica - PUC-Rio

**Prof. Carlos Antonio França Sartori**

Co-advisor

EPUSP

**Prof. Marbey Manhães Mosso**

Centro de Estudos em Telecomunicações – PUC-Rio

**Prof. Marco Antonio Grivet Mattoso Maia**

Centro de Estudos em Telecomunicações – PUC-Rio

**Dr. Alexandre Manoel Pereira Alves da Silva**

UNICAMP

**Prof. Maurício Weber Benjó da Silva**

UFF

**Prof. Úrsula do Carmo Resende**

CEFET-MG

Rio de Janeiro, April 9th, 2021

All rights reserved.

## Jorge Virgilio de Almeida

The author received the B.S. degree in Electrical Engineering from Pontifícia Universidade Católica do Rio de Janeiro (PUC-Rio) in 2015, the Ingénieur Diplômé degree from École Centrale de Lyon in 2016 and the M.Sc.Eng. degree in Electrical Engineering from PUC-Rio in 2017.

### Bibliographic data

De Almeida, Jorge Virgilio

Data and Power Transmission for Underwater Monitoring Systems Using Metamaterials / Jorge Virgilio de Almeida ; advisor: Eduardo Costa da Silva ; co-advisor: Carlos Antonio França Sartori. – 2021.

158 f. : il. color. ; 30 cm

Tese (doutorado)–Pontifícia Universidade Católica do Rio de Janeiro, Departamento de Engenharia Elétrica, 2021.

Inclui bibliografia

1. Engenharia Elétrica – Teses. 2. Linhas de transmissão virtuais. 3. Transmissão de energia sem fio subaquática. 4. Metamaterial. 5. Comunicação subaquática. I. Da Silva, Eduardo Costa. II. Sartori, Carlos Antonio França. III. Pontifícia Universidade Católica do Rio de Janeiro. Departamento de Engenharia Elétrica. IV. Título.

CDD: 621.3

To my unborn son, Francisco Virgilio de Almeida.

## Acknowledgements

I would like to acknowledge and thank my advisors, prof. Eduardo Costa da Silva and prof. Carlos Antonio França Sartori, for supporting me during my studies; Conselho Nacional de Desenvolvimento Científico e Tecnológico (CNPq) and Pontifícia Universidade Católica do Rio de Janeiro (PUC-Rio), for the scholarship and support; all my laboratory fellows and professors from the Centro de Estudos em Telecomunicações (CETUC), particularly prof. Marbey Manhães Mosso, prof. Marco Antonio Grivet Mattoso Maia, Renato Feitoza, Gidy Florez, Jorge Mitriane, Juliana Carvalho, Marcelo Balisteri, Carolina Maria Amaral and Gelza Barbosa, for their complicity and collaboration with my learning; the staff at the Department of Electrical Engineering, without whom none of this would be possible; and my friends for life, Maria Helena Martins Monteiro, Pedro José Furlani Vidal, Luiz Fernando Bez and Francisco Antonio de Seixas Neto, for their companionship.

Especially, I would like to acknowledge and thank prof. Glácio Lima Siqueira, who was my advisor during the first two years of my Ph.D. studies at PUC-Rio, having contributed to the development of many of the central ideas contained in this work.

Also, I would like to acknowledge and thank all those who have helped me to establish the Sociedade Brasileira de Metamateriais (SBMETA), particularly Dr. Alexandre Manoel Pereira Alves da Silva and prof. Úrsula do Carmo Resende, who have supported the project since its inception.

Moreover, I would like to acknowledge and thank my mother-in-law, Francisca Maria de Aquino, and my parents, Ivete Lobato de Almeida and Jorge Vitoriano de Almeida, for their support and encouragement.

Finally, I would like to acknowledge and thank my wife, Maria D. Freire de Almeida, for her love and dedication.

This study was financed in part by the Coordenação de Aperfeiçoamento de Pessoal de Nível Superior - Brasil (CAPES) - Finance Code 001.

## Abstract

De Almeida, Jorge Virgilio; Da Silva, Eduardo Costa (Advisor); Sartori, Carlos Antonio França (Co-advisor). **Data and Power Transmission for Underwater Monitoring Systems Using Metamaterials**. Rio de Janeiro, 2021. 158p. Tese – Departamento de Engenharia Elétrica, Pontifícia Universidade Católica do Rio de Janeiro.

Most modern underwater drones (UDs) employed in military and environmental monitoring operate in the ocean and are conceived as intermediary transceivers between their base station (BS) and underwater wireless sensor networks (UWSNs). Due to the salinity and consequently the conductivity of seawater, UD cannot use conventional radiofrequency (RF) transmissions, either for powering or communicating with the sensor nodes (SNs). Trying to overcome these limitations, inductive power transmission (IPT) systems have been pointed out as an alternative for reliable UD-assisted UWSNs. IPT presents lower losses than far-field-based techniques in complex media but is extremely limited in terms of operating distance. Based on that, the present thesis aims an all-integrated solution for UD-assisted monitoring systems based on IPT systems using metamaterial (MTM) lenses and reflectors dedicated to improving both the power transfer efficiency and the signal-noise ratio of the transmitted data. A new model of the magnetic channel, based on the virtual magnetic transmission line model, incorporating the MTM gains and the seawater losses, is also presented in order to facilitate the future systematization of UWSNs.

## Keywords

Virtual transmission lines; underwater wireless power transmission; metamaterial; underwater communication.

## Resumo

De Almeida, Jorge Virgilio; Da Silva, Eduardo Costa (Orientador); Sartori, Carlos Antonio França (Co-orientador). **Transmissão de Dados e Energia em Sistemas de Monitoramento Subaquático Usando Metamateriais**. Rio de Janeiro, 2021. 158p. Tese – Departamento de Engenharia Elétrica, Pontifícia Universidade Católica do Rio de Janeiro.

Muitos drones subaquáticos (DSs) modernos usados no monitoramento militar e ambiental operam no oceano e são concebidos como transceptores intermediários entre sua estação base (EB) e redes de sensores sem fio subaquáticas (RSSFSs). Devido a salinidade e conseqüentemente a condutividade da água do mar, DSs não podem usar transmissões de rádio frequência (RF) convencionais, tanto para alimentar quanto para se comunicar com os nós sensores (NSs). Tentando superar essas limitações, sistemas de transmissão indutiva de energia (TIE) têm sido apontados como uma alternativa para RSSFSs assistidas por DSs confiáveis. TIE apresenta perdas menores do que técnicas de campo distante em meios complexos, mas é extremamente limitada em termos de distância de operação. Baseado nisso, a presente tese visa uma solução mais integrada para sistemas de monitoramento assistidos por DSs baseado em sistemas de TIE usando lentes e refletores de metamaterial (MTM) dedicados a aprimorar ambas a eficiência na transmissão de energia e a razão sinal-ruído dos dados transmitidos. Um novo modelo do canal magnético, baseado no modelo de linhas de transmissão magnéticas virtuais, incorporando os ganhos dos MTMs e as perdas da água do mar, também é apresentado de modo a facilitar a futura sistematização das RSSFSs.

## Palavras-chave

Linhas de transmissão virtuais; transmissão de energia sem fio subaquática; metamaterial; comunicação subaquática.

# Table of contents

1	Introduction	27
1.1	Research background	27
1.2	Thesis motivation	30
1.3	Objectives	32
1.4	Methodology	32
1.5	Research impacts and milestones	33
1.6	Thesis structure	34
2	Literature review	36
2.1	Fundamentals of the theory of metamaterials	36
2.2	Fundamentals of inductive power transfer	39
2.2.1	Magnetic coupling	39
2.2.2	Resonant magnetic coupling	42
2.2.3	IPT systems in seawater	43
2.2.4	Compensation topologies	44
2.2.5	Metamaterial-enhanced inductive power transfer	47
2.3	Magneto-inductive waves and MTM-enhanced coupling	48
2.4	Final considerations	51
3	Inductive channel modeling based on VMGTL	52
3.1	Motivation	52
3.2	Theoretical aspects	53
3.2.1	Basic equations	53
3.2.2	Estimation of the model parameters	55
3.2.3	MTM interaction with the inductive channel	57
3.3	Model validation	58
3.4	Parametric study of MTM-assisted VMGTL	62
3.4.1	Channel sensitivity to $F$ and $Q$ parameters	62
3.4.2	Number $N$ of MTM slabs	64

3.4.3	Multiple MTMs set to different operating frequencies	65
3.5	VMGTL in lossy media	67
3.5.1	Effects of lossy dielectric media	67
3.5.2	Effects of lossy magnetic media	71
3.5.3	Estimation of seawater $G_e'$	71
3.6	Final considerations	76
4	MTM design for underwater SIDPT applications	78
4.1	Design of MTM lenses	78
4.1.1	Double-sided spiral resonator unit-cell	78
4.1.2	DSSR equivalent material properties	80
4.1.3	Fine tuning of the unit cell	82
4.1.4	Hybrid MTMs	84
4.1.5	DSRR with coarse tuning control in air, water and seawater	94
4.2	Effect of insulation on efficiency	101
4.3	Artificial magnetic reflectors based on TL-mode coils	105
4.4	Final considerations	111
5	Modulation scheme for efficient MTM-assisted SIPDT	113
5.1	Evaluation using phase modulation	113
5.2	Evaluation using frequency modulation	121
5.2.1	Comparison between FSK and PSK	121
5.2.2	Optimum frequency range for FSK	124
5.2.3	Dual-band MTM-assisted SIPDT	129
5.2.4	Maximum data rate of MTM-assisted SIPDT using FSK	132
5.3	Final considerations	132
6	Conclusion	134
6.1	Final comments	134
6.2	Contributions	135
6.3	Future work	136
6.3.1	Experimental verification of intermediary results	136
6.3.2	Improvement of the VMGTL theory	137
6.3.3	Diversity schemes and MIMO VMGTL	137

6.3.4	Dual-band MTM unit-cells based on TL-modes	137
6.3.5	Implementation and experimental validation of the proposed system	138
6.3.6	Simultaneous magnetic and electric coupling based power and data transmission system, for underwater applications	139
	References	140
	A Published and accepted papers	149
	B Student design competition award	151
	C MATLAB code	152

## List of Figures

Figure 1.1: UD-assisted UWSN	29
Figure 1.2: Propagation losses in different UWC/loUT other than IPT [20]	30
Figure 2.1: MTMs are described by effective parameters like natural materials	37
Figure 2.2: (a) Classification of the EM materials and (b) refraction on both DPS and DNG media. Notice that in DNG power flux and phase velocity are inverted	37
Figure 2.3: WPT main technologies and research areas [42]	40
Figure 2.4: Antenna field regions	41
Figure 2.5: Near-field limit $r_{NF}$ as a function of the frequency	42
Figure 2.6: Block diagram of a typical IPT system configuration [26]	43
Figure 2.7: Classification of the compensation topologies [42]	44
Figure 2.8: The four basic compensation topologies of IPT systems: (a) SS, (b) SP, (c) PS and (d) PP [26]	44
Figure 2.9: (a) Double-sided LCC and (b) double-sided LCL topologies [42]	45
Figure 2.10: LC/S compensation topology	45
Figure 2.11: Symbol period $T_s$ must be long enough to ensure that transient effects of the system are negligible	46
Figure 2.12: MTM-based focalization of the magnetic-field evanescent modes	47
Figure 2.13: MTM-based magnetic shielding or reflector: (a) relative position on the inductive link and (b) prototype using SR cells [58]	48
Figure 2.14: (a) Axial and (b) planar orientations [59]	48
Figure 2.15: Dispersion for 1-D axial array with $\kappa_m = 0.1$ : normalized (a) $\beta$ and (b) $\alpha$ [59]	49
Figure 2.16: Dispersion for 1-D planar array with $\kappa_m = -0.1$ : normalized (a) $\beta$ and (b) $\alpha$ [59]	49

Figure 2.17: Developed MTM-integrated driver using a unit-cell with spacing varying according to a Fibonacci sequence	50
Figure 2.18: Schematic representation of a MNG MTM as 2D-array of loaded loops	51
Figure 3.1: The displacement magnetic current $I_m, d$ , between the TX and RX coils, forms a virtual circuit similar to a conventional TL. According to Poynting theorem, power flow in the inductive channel depends on the perpendicular component of the magnetic near field created by the magnetic potential difference between the flux in positions $y_1$ and $y_2$	53
Figure 3.2: VGMTL equivalent circuit of two magnetically coupled coils	55
Figure 3.3: SR-based MTM prototype	59
Figure 3.4: Magnitude of the transfer function as a function of frequency for a VMGTL without MTM: (a) analytical model and (b) numerical simulation, for $r = 4$ cm (blue), $r = 5$ cm (orange) and $r = 6$ cm (yellow)	60
Figure 3.5: Magnitude of the transfer function as a function of frequency for a VMGTL assisted by one MTM slab: (a) analytical model and (b) numerical simulation, for $r = 4$ cm (blue), $r = 5$ cm (orange) and $r = 6$ cm (yellow)	60
Figure 3.6: (a) Attenuation and (b) propagation constants as a function of frequency for a VMGTL without MTM for $r = 4$ cm (blue), $r = 5$ cm (orange) and $r = 6$ cm (yellow)	60
Figure 3.7: (a) Attenuation and (b) propagation constants as a function of frequency for VMGTL assisted by one MTM slab, for $r = 4$ cm (blue), $r = 5$ cm (orange) and $r = 6$ cm (yellow)	61
Figure 3.8: Sensitivity of VMGTL (a) attenuation and (b) propagation constants to F	63
Figure 3.9: Sensitivity of VMGTL (a) attenuation and (b) propagation constants to Q	63

Figure 3.10: Sensitivity of VMGTL transfer function to (a) $F$ and (b) $Q$ . While $F$ governs the bandwidth of the passband, $Q$ regulates only the magnitude of the response	63
Figure 3.11: The bandwidth-gain trade-off when operating at the region of (a) minimum distortion and (b) high gain	64
Figure 3.12: VMGTL transfer function with an increasing number $N$ of MTM slabs	64
Figure 3.13: (a) Attenuation and (b) propagation constants with three MTM slabs, for case 1: $f_{01} = 10$ MHz, $f_{02} = 32$ MHz and $f_{03} = 40$ MHz	66
Figure 3.14: (a) Attenuation and (b) propagation constants with three MTM slabs, for case 2: $f_{01} = 10$ MHz, $f_{02} = 31$ MHz and $f_{03} = 32$ MHz	66
Figure 3.15: Results for the VMGTL transfer function with 3 MTM slabs for (a) case 1 and (b) case 2	67
Figure 3.16: ADS-simulated IPT transfer function (a) without and (b) with a MTM is characterized by three major regions: 1) purely inductive 2) magneto-capacitive and 3) self-resonant, for $r = 4$ cm (blue), $r = 5$ cm (orange) and $r = 6$ cm (yellow)	68
Figure 3.17: Estimation of the transfer function using VMGTL with $G_e' = 4 \cdot 10^5$ (a) without and (b) with one MTM slab, for $r = 4$ cm (blue), $r = 5$ cm (orange) and $r = 6$ cm (yellow)	68
Figure 3.18: Attenuation constant for the VMGTL with $G_e' = 4 \cdot 10^5$ (a) without and (b) with one MTM slab as a function of frequency, for $r = 4$ cm (blue), $r = 5$ cm (orange) and $r = 6$ cm (yellow)	69
Figure 3.19: Propagation constant for the VMGTL with $G_e' = 4 \cdot 10^5$ (a) without and (b) with one MTM slab as a function of frequency, for $r = 4$ cm (blue), $r = 5$ cm (orange) and $r = 6$ cm (yellow)	69
Figure 3.20: MTM gain as a function of $G_e'$	70
Figure 3.21: MTM gain as a function of $G_m'$	71

Figure 3.22: Distribution of the ocean's salinity	72
Figure 3.23: Dielectric loss in seawater: exponential regression estimation (black curve) and data extracted from [74] (red dots). The frequencies of interest for UWPT lies on the left region of the dashed green line	73
Figure 3.24: Ocean water temperature as a function of depth [75]	74
Figure 3.25: Simulated results for the MTM gain in air (solid line), freshwater (circle) and seawater (triangle) for a MTM-assisted WPT system using coils with $r = 5\text{cm}$	75
Figure 3.26: Representation of the interaction of the eddy currents. These eddy currents behave as virtual coils inside the inductive link	75
Figure 4.1: Proposed MTM DSSR unit cell with copper surfaces highlighted in yellow and red. The substrate with thickness $e$ was kept transparent to highlight the metallic vias	79
Figure 4.2: Proposed DSSR unit-cell employed as a lens	81
Figure 4.3: Equivalent (a) $\mu r$ and (b) gain of the proposed unit-cell, when it is employed as a lens in a IPT system. Notice that the gain occurs out of the resonance of the cell	81
Figure 4.4: Geometric optimization of the unit-cell for fine tuning	83
Figure 4.5: Equivalent $\text{Re}\mu r$ of the DSSR unit cell, for gap $g = [0.2, 1.8]$ , in steps of 0.2	83
Figure 4.6: Equivalent $\text{Im}\mu r$ of the DSSR unit cell, for gap $g = [0.2, 1.8]$ , in steps of 0.2	83
Figure 4.7: Enhanced focusing due to non-uniform central and border regions [78]	84
Figure 4.8: Prototypes U1 and U2 with equal central and border regions	85
Figure 4.9: Prototype H1 with a central-region and a border-region	86
Figure 4.10: Prototype H2 with a central-region and a border-region	86
Figure 4.11: $S_{21}$ of the 4 prototypes, compared with the system without MTM	88

Figure 4.12: Average amplitude of the H-field normal to the surface of prototype U1	89
Figure 4.13: Average amplitude of the H-field tangential to the surface of prototype U1	90
Figure 4.14: Average amplitude of the H-field normal to the surface of prototype U2	90
Figure 4.15: Average amplitude of the H-field tangential to the surface of prototype U2	91
Figure 4.16: Average density of power flow through the surface of prototype U1	91
Figure 4.17: Average density of power flow through the surface of prototype U2	91
Figure 4.18: Average amplitude of the H-field normal to the surface of prototype H1	92
Figure 4.19: Average amplitude of the H-field tangential to the surface of prototype H1	92
Figure 4.20: Average amplitude of the H-field normal to the surface of prototype H2	93
Figure 4.21: Average amplitude of the H-field tangential to the surface of prototype H2	93
Figure 4.22: Average density of power flow through the surface of prototype H1	94
Figure 4.23: Average density of power flow through the surface of prototype H2	94
Figure 4.24: P1 system	95
Figure 4.25: P1 system assisted by MTM	95
Figure 4.26: P2 system	96
Figure 4.27: P2 system assisted by MTM	96
Figure 4.28: MTM gain of P1 in air (solid line), freshwater (circle) and seawater (triangle) in comparison with P1 in the air without MTM	97
Figure 4.29: MTM gain of P2 in air (solid line), freshwater (circle) and seawater (triangle) in comparison with P2 in the air without MTM	97

Figure 4.30: S21 of P1 and P2 in different environments	98
Figure 4.31: Misaligned P1 system	99
Figure 4.32: Misaligned P1 system assisted by MTM	99
Figure 4.33: MTM gain of misaligned P1 in air (solid line), freshwater (circle) and seawater (triangle) in comparison with misaligned P1 in the air without MTM	100
Figure 4.34: S21 of the P1 and misaligned P1 in the considered environments	100
Figure 4.35: Non-insulated coils immersed in seawater: $\sigma = 5\text{Sm}$ , $r = 5\text{ cm}$	101
Figure 4.36: Insulated coils immersed in seawater: $\sigma = 5\text{Sm}$ , $r = 5\text{ cm}$	101
Figure 4.37: Transfer function of the non-insulated coils immersed in seawater, with separation distance $D = 1\text{ cm}$ , $D = 5\text{ cm}$ and $D = 15\text{ cm}$	102
Figure 4.38: Transfer function of the air-insulated coils immersed in seawater, with separation distance $D = 1\text{ cm}$ , $D = 5\text{ cm}$ and $D = 15\text{ cm}$	102
Figure 4.39: Transfer function of the freshwater-insulated coils immersed in seawater, with separation distance $D = 1\text{ cm}$ , $D = 5\text{ cm}$ and $D = 15\text{ cm}$	102
Figure 4.40: Comparison between the transfer function with air (green) and freshwater (red) insulation for $D = 5\text{ cm}$	103
Figure 4.41: Average amplitude of the component of the E-field perpendicular to the magnetic flux at $f_0 = 23.90\text{ MHz}$ with air-insulated coils	104
Figure 4.42: Average amplitude of the component of the E-field perpendicular to the magnetic flux at $f_0 = 23.90\text{ MHz}$ with freshwater-insulated coils	104
Figure 4.43: Currents on TL (a) and antenna (b) mode coils	105
Figure 4.44: TL-mode unit cell with coarse tuning control	106
Figure 4.45: TL-mode cells employed as reflectors. Notice that the MTM cells are placed behind the coupled coils	107

Figure 4.46: Simulation of the gain when the TL-mode unit-cell is employed as a reflector	107
Figure 4.47: Equivalent $\mu_r$ of the proposed TL-mode unit-cell	108
Figure 4.48: UWPT system using an array of ferromagnetic bars as a reflector [79]	108
Figure 4.49: TL-mode gain regions cells with $C_{added} = 10$ pF (a) and $C_{added} = 1$ nF (b). Notice that the second resonance is not affected by $C_{added}$	109
Figure 4.50: 3x3 MTM reflectors	110
Figure 4.51: Transfer function of the TX and RX coils assisted by 3x3 MTM reflectors	110
Figure 4.52: TX and RX coils assisted by 3x3 MTM reflectors. Notice that the vortex-like behavior around the MTM surface creates the apparent magnetic-flux reflection	110
Figure 5.1: Data flow cosimulation on ADS for BPSK and QPSK	114
Figure 5.2: BPSK constellation diagram in air without MTM for FBW values. Notice that input and output symbols are phase-shifted by $90^\circ$ , as expected by Eq. (50)	116
Figure 5.3: BPSK constellation diagram in air with one MTM slab for FBW values. Notice that the MTM slab changes the phase relationship between the input and output symbols for less than $90^\circ$ . Besides, copies of the output symbols are generated by the MTM	116
Figure 5.4: BPSK constellation diagram in freshwater with one MTM slab for FBW values. Notice that the results for air and freshwater are the same	116
Figure 5.5: BPSK constellation diagram in seawater with one MTM slab for FBW values. Notice that the seawater losses reduce that MTM-induced repetition of the symbols due to the reduction of the MTM gain	117
Figure 5.6: EVM of the MTM-assisted IPT in air (red dash), in freshwater (blue dot) and seawater (green dot) compared	

with the IPT system without MTM in air (solid black) using BPSK modulation	117
Figure 5.7: QPSK constellation diagram in air without MTM for FBW values. Notice that the output symbols are also rotated in $90^\circ$ in relation to the input ones although it is disguised by the symmetry of the QPSK constellation	119
Figure 5.8: QPSK constellation diagram in air with one MTM slab for FBW values. Notice that the QPSK symbols are repeated by the MTM lattice	119
Figure 5.9: QPSK constellation diagram in freshwater with one MTM slab for FBW values. Notice that the results in air and freshwater are the same	119
Figure 5.10: QPSK constellation diagram in seawater with one MTM slab for FBW values	120
Figure 5.11: EVM of the MTM-assisted IPT in air (red dash), freshwater (blue dot) and seawater (green dot), compared with the IPT system without MTM in air (solid black) using QPSK modulation	120
Figure 5.12: Amplitude fluctuations due to fast phase shifts during symbol transitions	121
Figure 5.13: Comparison between typical (a) ASK, (b) PSK and (c) FSK spectra	122
Figure 5.14: Normalized bit rate as a function of the normalized bit energy using different modulation schemes, for BER = $10^{-5}$ [83]. Notice that FSK only outstands bit power efficiency of PSK systems when the number of symbols $M > 4$	123
Figure 5.15: Comparison between the transfer functions of the 2-coil IPT system, in air and seawater ( $\sigma = 5 \text{ S/m}$ ), for separation distance $D = r$ and $D = 2r$	125
Figure 5.16: Normalized skin depth $\delta_n$ as a function of frequency, for $\sigma$ varying from 1 to 6 S/m, in steps of 1 S/m, and $D = r$	125
Figure 5.17: Transfer function divergence between a 2-coil IPT system in air and seawater as a function of frequency, for $\sigma$	

varying from 1 to 6 S/m, in steps of 1 S/m, and  $D = r$ . The results are presented in a frequency range (a) from 0.1 MHz to 100 MHz and (b) zoomed in the frequency range where all curves present  $\delta n < 1$  126

Figure 5.18: 2-coil IPT system insensitivity range to the medium properties, for  $D = r$  127

Figure 5.19: 2-coil IPT system loss in seawater in comparison with air-medium case, for  $\sigma$  varying from 1 to 6 S/m, in steps of 1 S/m, and  $D = r$ . Notice that after the frequency range achieves  $\delta n < 1$  the relative loss varies linearly with  $\sigma$  127

Figure 5.20: Magneto-inductive factor as a function of frequency, for  $P_{IN} = 1$  W 128

Figure 5.21: Proposed dual-band strategies using (a) two MTM lenses and (b) one MTM lens and two reflectors 130

Figure 5.22: Transfer function of the system using two MTM lenses with different  $f_0$  with optimal frequency deviation for maximum dual-band gain 130

Figure 5.23: Transfer function of the system using a combination of one MTM and two MTM reflectors 131

Figure 5.24: Transfer function of the system using two MTM lenses with different  $f_0$  with sub-optimal frequency deviation 131

Figure 6.1: Manufactured MTM (a) lenses and (b) reflectors 136

Figure 6.2: Purchased UD, PowerVision PowerRay 139

## List of Tables

Table 1: Comparison between MTM uniform and hybrid topologies	87
Table 2: Comparison between the data rates of the MTMs	132
Table 3: UD-assisted UWSN	139

## Acronyms

<b>ADS</b>	Advanced Design System
<b>APDT</b>	Acoustic Power and Data Transmission
<b>ASK</b>	Amplitude Shift Keying
<b>AUT</b>	Autonomous Underwater Technology
<b>AUV</b>	Autonomous Underwater Vehicle
<b>BER</b>	Bit Error Rate
<b>BPSK</b>	Binary Phase-Shift Keying
<b>BS</b>	Base Station
<b>BW</b>	Bandwidth
<b>CMT</b>	Coupled mode theory
<b>CST</b>	Computer Simulation Technology
<b>DNG</b>	Double Negative
<b>DPS</b>	Double-Positive
<b>DSSR</b>	Double-sided Spiral Resonator
<b>EM</b>	Electromagnetic
<b>EMF</b>	Electromotive Force
<b>ENG</b>	Electric Negative
<b>ESA</b>	Electrically Small Antenna
<b>EVM</b>	error vector magnitude
<b>FBW</b>	Fractional Bandwidth
<b>FSK</b>	Frequency-Shift Keying
<b>IoT</b>	Internet of Things
<b>IoUT</b>	Internet of Underwater Things
<b>IPT</b>	Inductive Power Transmission
<b>MI</b>	Magnetoinductive
<b>MIMO</b>	Multiple-Input Multiple-Output
<b>MIR</b>	Medium Insensitivity Range
<b>MMF</b>	Magnetomotive Force
<b>MNG</b>	Magnetic Negative
<b>MTM</b>	Metamaterial
<b>PA</b>	Power Amplifier

<b>PDL</b>	Power Delivered to the Load
<b>PEC</b>	Perfect Electrical Conductor
<b>POC</b>	Power Output Capacity
<b>PP</b>	Parallel-Parallel
<b>PS</b>	Parallel-Series
<b>PTE</b>	Power Transfer Efficiency
<b>QPSK</b>	Quadrature Phase-Shift Keying
<b>RF</b>	Radiofrequency
<b>RMC</b>	Resonant Magnetic Coupling
<b>ROV</b>	Remote Underwater Vehicle
<b>RX</b>	Receiver
<b>SAR</b>	Specific Absorption Rate
<b>SCMR</b>	Strong Coupling Magnetic Resonance
<b>SIPDT</b>	Simultaneous Inductive Power and Data Transmission
<b>SMD</b>	Surface-Mount Device
<b>SN</b>	Sensor Node
<b>SP</b>	Series-Parallel
<b>SR</b>	Spiral Resonator
<b>SRR</b>	Split-Ring Resonator
<b>SS</b>	Series-Series
<b>SUT</b>	Society for Underwater Technologies
<b>SWIPT</b>	Simultaneous Wireless Information and Power Transmission
<b>TE</b>	Transformational Electromagnetics
<b>TL</b>	Transmission Line
<b>TX</b>	Transmitter
<b>UD</b>	Underwater Drones
<b>UWC</b>	Underwater Communications
<b>UWOC</b>	Underwater Wireless Optical Communication
<b>UWSN</b>	Underwater Wireless Sensor Network
<b>VMGTL</b>	Virtual Magnetic Transmission Line
<b>WPT</b>	Wireless Power Transfer
<b>ZPA</b>	Zero-phased Angle
<b>ZVS</b>	Zero-voltage Switching

## List of Symbols

$\mathcal{R}'_m$	VMGTL Distributed Magnetic Reluctance
$C'$	VMGTL Distributed Capacitance
$C_0$	Equivalent Capacitance of the Coils
$C_{SMD}$	Coarse Tuning Capacitor
$G'_e$	VMGTL Distributed Electrical Conductance
$G'_m$	VMGTL Distributed Magnetic Conductance
$I_{IN}$	Input Current
$I_{e,d}$	Electric Displacement Current
$I_{m,d}$	Magnetic Displacement Current
$L'$	VMGTL Distributed Inductance
$L_0$	Equivalent Inductance of the Coils
$L_{cell}$	Unit-Cell Inductance
$M_{RX-TX}$	Mutual Inductance between TX and RX Coils
$N_{turns}$	DSSR Unit-Cell Number of Turns
$P_{IN}$	Input Power
$R_L$	Load Resistance
$R_b$	Bit Rate
$R_i$	Internal Resistance of the Source
$R_s$	Symbol Rate
$S_{21}$	Transmission Gain / Channel Transfer Function
$T_s$	Symbol Period
$V_m$	Magnetic Potential
$Y_m$	Shunt Magnetic Admittance
$Z_0$	Characteristic Electrical Impedance
$Z'_{MTM}$	VMGTL Equivalent Distributed MTM Impedance
$Z_m$	Series Magnetic Impedance
$d_{mtm1}$	DSSR Unit-Cell Outer Dimension 1
$d_{mtm2}$	DSSR Unit-Cell Outer Dimension 2
$d_{via}$	DSSR Unit-Cell Diameter of the Electric Via
$f_0$	Operating Frequency

$f_R$	Unit-Cell Resonance Frequency
$f_{sat}$	Saturation Frequency
$r_{NF}$	Near-Field Region
$t_{dP}$	Transient Response of Parallel RLC Circuits
$t_{dS}$	Transient Response of Series RLC Circuits
$t_d$	Transient Delay
$v_g$	Group Velocity
$v_p$	Phase Velocity
$v_s$	Signal Velocity
$J_{e,d}$	Density of Electric Displacement Current
$J_{m,d}$	Density of Magnetic Displacement Current
$\delta_n$	Normalized Skin Depth
$\epsilon_r$	Relative Electric Permittivity
$\kappa_{m,MTM}$	Magnetic Coupling between the MTM and TX and RX Coils
$\kappa_m$	Magnetic Coupling
$\lambda_0$	Wavelength in Free Space
$\lambda_m$	Wavelength in the Medium
$\mu_r$	Relative Magnetic Permeability
$\omega_0$	Operating Angular Frequency
$\phi_e$	Electric Flux
$\phi_m$	Magnetic Flux
$D$	Separation Distance
$F$	Coupling Coefficient between Adjacent Cells of the Lattice
$L$	Inductance
$M$	Number of Symbols
$N$	Number of MTMs
$Q$	Quality Factor
$R$	Resistance
$T$	Temperature
$Z$	Electrical Impedance
$a$	Array Periodicity
$e$	DSSR Unit-Cell Substrate's Thickness

$g$	DSSR Unit-Cell Gap
$n$	Reflection Index
$p$	Diameter of the Coil's Wire
$r$	Coil's Radius
$\tan \delta$	Loss Tangent of the Medium
$w$	DSSR Unit-Cell Conductor's Width
$\mathbf{B}$	Density of Magnetic Flux
$\mathbf{D}$	Density of Electric Flux
$\mathbf{E}$	Electric-Field Vector
$\mathbf{H}$	Magnetic-Field Vector
$\mathbf{S}$	Poynting Vector
$\mathbf{k}$	Wave Vector
$\mathbf{u}$	Total Energy Density
$\Gamma$	Reflection Coefficient
$\alpha$	Attenuation Constant
$\beta$	Propagation or Phase Constant
$\gamma$	Complex Propagation Constant
$\varepsilon$	Electric Permittivity
$\mu$	Magnetic Permeability
$\sigma$	Conductivity
$\omega$	Angular Frequency

*Todos cantam sua terra,  
Também vou cantar a minha,  
Nas débeis cordas da lira  
Hei de fazê-la rainha;  
— Hei de dar-lhe a realeza  
Nesse trono de beleza  
Em que a mão da natureza  
Esmerou-se em quanto tinha.*

*Correi pr'as bandas do sul:  
Debaixo dum céu de anil  
Encontrareis o gigante  
Santa Cruz, hoje Brasil;  
— É uma terra de amores  
Alcatifada de flores,  
Onde a brisa fala amores  
Nas belas tardes de abril.*

Casimiro de Abreu, *Primaveras*

*Most of the fundamental ideas of science are essentially simple, and may, as a rule, be expressed in a language comprehensible to everyone.*

Albert Einstein

# 1

## Introduction

### 1.1

#### Research background

More than 71% of the surface of the Earth is covered by oceans and seas, whose temperatures regulate the climate of the planet and the behavior of the winds. Besides that, oceans, seas and coasts are the backbone of the world's economy, since more than 90% of the world's trade is made using sea routes and ports. Usually, ocean economy (also called blue economy) is subdivided in 5 sectors, which includes renewable energy, tourism, biotechnology, deep sea mining and aquaculture. According to the Organisation for Economic Co-operation and Development (OECD), the ocean economy totalized USD 1.5 trillion in 2010 and is expected to double before 2030 [1].

Because of that, underwater drones (UDs), such as remotely operated underwater vehicles (ROVs) and autonomous underwater vehicles (AUVs), have drawn a lot of attention in the last decade for high-end applications as anti-submarine warfare, subsea infrastructure maintenance and marine intelligence, surveillance and reconnaissance (MISR). However, no matter the application, energy limitation keeps being the major drawback when it comes to the performance of extended UD missions. To assure a better trade-off between size, weight, cost and energy autonomy, wirelessly rechargeable Li-Ion batteries have been pointed out as the best available option for UD power source [2-4].

Many solutions have been presented in literature for UD recharging mechanism. Most of them are based on inductive power transmission (IPT) since the energy density of acoustic wireless power transfer (WPT) is too low and resonant magnetic coupling (RMC) has been proved to present considerably lower losses than radiofrequency (RF) wave propagation in salt water [5]. The most traditional architectures adopt a docking concept [6-7], having the disadvantage of being quite dependent of the alignment between the UD and its source, which is hard to be achieved due to the water motion. Besides that, docking stations have a high-cost maintainability, being susceptible to biofouling, contaminants and any

other sort of dirt collected by it over time [8]. In [9], coil shielding strategies are presented to minimize the induced eddy currents, which are the major source of loss at the transmitter. In [10], multi-coil based receivers are proposed to minimize the parallel and angular alignment dependency of the magnetic coupling. In [11], a coil structure with two transmitter coils and one receiver is proposed to reduce the eddy-current losses and increase the power transfer efficiency (PTE) of the system in 10%. In [12], a transmitter coil composed of three mutually orthogonal loops, with different feeding phases, is presented.

However, since the UD is filled with instruments and equipment, multi-coil-based solutions in the transmitter are too bulky to be practical. Consequently, researchers started to investigate innovative designs that replace coil diversity by geometric optimization of their core and/or winding. In [7], the maximization of the PTE of such systems are shown to depend on the transversal section of the transmitter and receiver coils, which should be adapted to the curvature of the UD hull. In [13], a magnetic core design optimization is proposed in order to reduce the misalignment sensitivity of the coupler. In [14-15], axial-rotation misalignment problems are also addressed. In [16], a wide power supply area strategy based on multi-coil repeaters has been proposed aiming at enabling transmissions in depths of more than ten meters, avoiding time-consuming UD travels to recharging stations. In [17], insulation cavities are proposed to minimize the eddy current losses. In [18], multi-coil coupling has been demonstrated to provide a good trade-off between bandwidth and efficiency enhancement. Finally, it was also shown that electric-coupling based WPT could be employed in underwater applications due to the high-permittivity of the water [19]. Nevertheless, this option relies on expensive and complex high-voltage and fast-switching circuits.

One of the most important applications of UDs, which is the main concern of this thesis, is the utilization of these seacrafts as data-collecting intermediary-transceiver for underwater communication (UWC) [20]. That is, the using of UDs as data and power movable relay nodes for future Internet of Underwater Things (IoUT), as shown in Figure 1.1. Underwater wireless sensor networks (UWSN), which are the building blocks of UWC/IoUT, are composed of sensor nodes (SNs) deployed in an underwater location to collect data and/or to perform tasks, such as oceanographic or underwater pollution monitoring [20-21]. The computational power demanded by these systems are rapidly increasing, since nowadays the majority of their SNs are active devices that can perform power-consuming tasks such as communicate with neighboring nodes, detect and respond to surrounding changes and be remotely operated.

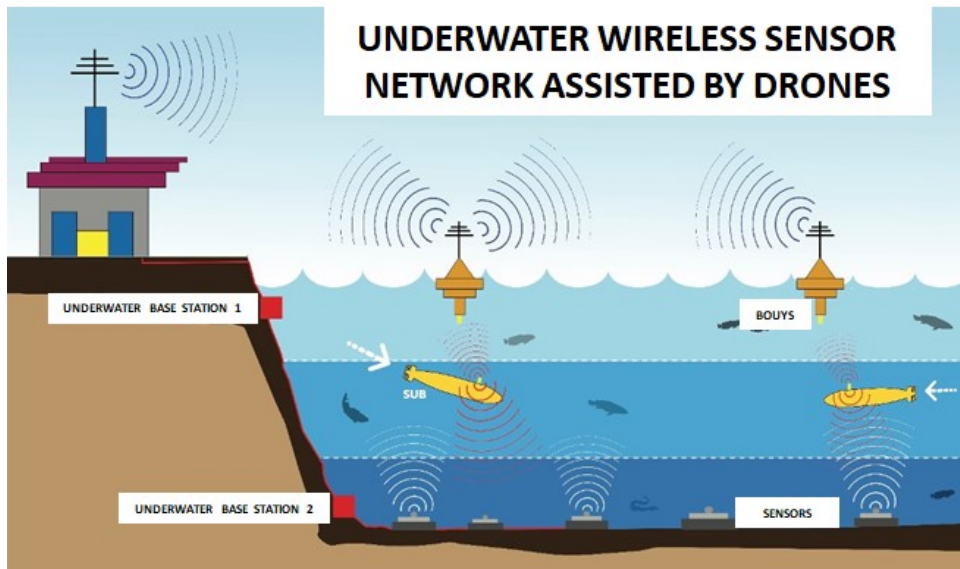


Figure 1.1: UD-assisted UWSN

Most actual UWSNs still employ acoustic power and data transmission (APDT) systems because of the salinity of most underwater environments [20, 22]. Nonetheless, it imposes severe limitations to the system due to the narrowband nature of the acoustic transmissions. Besides, APDT is stochastic in nature due to water and sediment motions in lakes, rivers and oceans, due to maritime currents, tides and wind-induced waves. Acoustic multiple-input multiple-output (MIMO) techniques as well as metamaterials (MTMs), have been proposed to enhance the robustness of those systems and reduce destructive interference due to the water motion [20, 23]. However, similarly to what happened to the UD systems, the low-power nature of acoustic wireless power transfer (AWPT) is prohibitive to the effective recharging of active SNs.

At last, underwater wireless optical communication (UWOC) has also been considered because of its extremely high data transmission rates [24]. The underwater optical channel, however, keeps being incredibly challenging for the actual UWSNs, due to turbulence, temperature fluctuations and salinity, not being reliable enough for WPT. In Figure 1.2, the main issues of UWC, other than IPT, are summarized.

Considering that RMC is already being proved reliable for UD recharging systems and that UDs can navigate to the very vicinity of the sensor field, some recent works have proposed to use IPT systems for both UWSN recharging and communication [25-26]. This solution has the obvious advantage of solving the water/sediment motion problem (since the magnetic field distribution is not affected by them). Furthermore, it also improves both the data rate and the recharging delay

of the system. Consequently, considering the data transmission, magnetoinductive (MI) based communications sounds like the obvious choice, since they occur naturally in RMC-based systems and are robust to attenuation in complex media (especially, conductive ones).

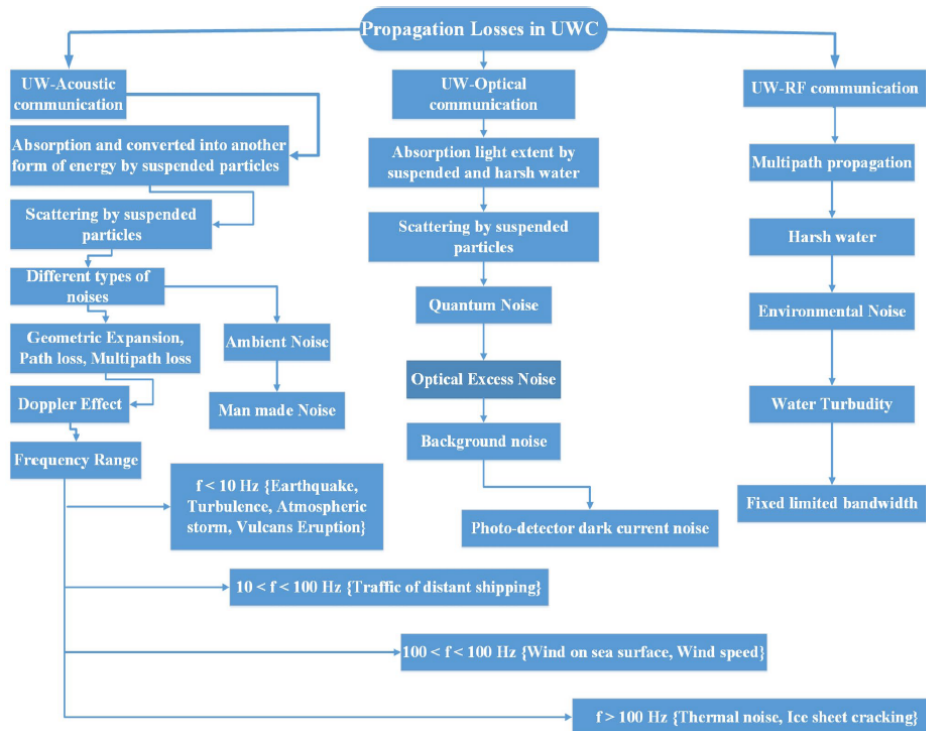


Figure 1.2: Propagation losses in different UWC/loUT other than IPT [20]

## 1.2

### Thesis motivation

The main reasons that motivate the studies conducted on the Ph.D thesis to this particular research topic are:

- The Brazilian coast measures around 7,500 km, being the longest inter and subtropical coastline of the world, as well as the longest coastline in the South Atlantic region. Since more than 80% of the Brazilian population lives close to the coastline, the permanent monitoring of the Brazilian sea is vital for the security of most Brazilians, especially to the safety of the inhabitants of the City of Rio de Janeiro, the biggest Brazilian coast city and second economic region of Brazil;

- South Atlantic biodiversity is one of the greatest of the world, comparable and maybe even larger than the biodiversity in Amazon and Pantanal Regions, making it an important resource and asset to be protected and exploited for the benefit of the Brazilian biotechnology and pharmaceutical companies. Future underwater explorations and associated industries in Brazil and in Rio de Janeiro will certainly benefit of UWSN;
- Brazil possesses an incredible waterway network of 63,000 *km* that connects most of the Brazilian territory, including the Amazon River, in the North Region, the second largest river of the world. Nowadays, only 30% of these waterways (about 19,000 *km*) is used for some form of inland navigation, transporting no more than 5% of the country's total cargo. However, the future growth of the Brazilian river terminals, that could reduce up to 20 times the transportation costs in Brazil, would also demand the development of underwater monitoring systems in most of the inner side of Brazil. It is of particular interest the monitoring of Paraíba do Sul river, the larger river in the State of Rio de Janeiro, which connects the two major metropolitan regions of Brazil (São Paulo and Rio de Janeiro), and many important intermediary regions in the Vale do Paraíba, Região Serrana Fluminense (including Juiz de Fora-MG) and Campo dos Goytacazes-RJ (including Porto do Açú in São João da Barra-RJ);
- Brazil, particularly the State of Rio de Janeiro, has a long tradition in the development of underwater technologies and could be one of the main leaders of the world in this segment. Due to its strategic and central position in the South Atlantic, the "Old Province" (the State of Rio de Janeiro) was chosen to host a branch of the Society for Underwater Technologies (SUT), created by the British government in 1968. The Brazilian SUT, established at the UK Brazil Centre of Ocean Engineering, UFRJ, Rio de Janeiro City, was created in 1999. It was the first branch of the SUT created out of the UK and its commonwealth, and the only one in Latin America. At PUC-Rio, many Master and PhD thesis on underwater technologies, including ROVs and AUVs, have been written in the last decades, but there is still room for many researchers on UWSN and IoUT.
- In 2020, the State of Rio de Janeiro was responsible for more than 80% of all Brazilian oil's production and 70% of its refining. Most new Brazilian oil fields are in an area enclosed by a circle of 500 km radius from Cabo Frio-RJ. Hence, underwater technologies will keep being a major axis of development of the Fluminense industry and society.

### 1.3

#### Objectives

Since previous works on UD-assisted UWSN are primarily concentrated in the design of just one part of the link (from the dock to the UDs *or* from the UD to the SNs), this thesis proposes:

- 1) To fulfill that gap by developing an all-integrated inductive coupling-based solution for the UD transceiver. This transceiver is expected to simultaneously exchange energy and information with both the base station (BS) and the UWSN;
- 2) To conceive near-field MTM-based lenses and/or reflectors (adapted to the underwater environment) in order to maximize the overall system PTE and throughput, as well as minimizing the induced eddy currents in the surroundings; and
- 3) To develop a theoretical model of the underwater magnetic channel based on the virtual magnetic transmission line (VMGTL) theory. This new model of the channel intends to facilitate the systematization of underwater monitoring systems since VMGTL theory is much more practical and straightforward when dealing with the incorporation to the link budget of complex media losses and MTM gains.

### 1.4

#### Methodology

- Initially, this research focused on the development of both air and subsea MTM-based lenses, including the investigation of how the high permittivity of water (and its conductivity in the ocean) affects the MTM interaction with the near field and its achievable gain. Besides, it was of particular interest to understand and describe the behavior of the MI waves in the presence of MTM in a more physically insightful way, especially on the MTM role on the generation or suppression of eddy currents. To comprehend these phenomena, an analytical model called theory of virtual magnetic transmission lines was proposed and applied along this thesis.
- Different MTM unit-cells were investigated, as well the fine-tuning control of its equivalent material properties by means of geometric optimization and constituent material selection. One major finding of these investigations was that unit cells other than the so-called  $\mu$ -negative ones, such as split-ring resonators (SRRs) or spiral resonators (SRs), were capable to provide high gain to IPT systems. More specifically, it was the case of resonators employing

currents on transmission-line (TL) mode (differential mode). The TL-mode based unit cells, presented for the first time in this thesis, was found to present a nearly zero-loss paramagnetic response that can be used to build artificial magnetic reflectors to confine the magnetic flux between the drivers of the system, greatly increasing its efficiency. Also, hybrid MTM lenses were evaluated aiming to maximize the MTM gain.

- After that, a system-level study was conducted in order to compare the performance of the proposed simultaneous inductive power and data transmission (SIPDT), using different combinations of MTM lenses and reflectors. Besides, different modulation formats were also evaluated, such as phase-shift keying (PSK) and frequency-shift keying (FSK), since they are more suitable for high-efficient power amplifiers (PAs) topologies. The optimum operating frequency were discussed considering seawater losses, penetration depth and the magneto-inductive factor of the IPT systems.
- Based on the achieved results, different strategies for achieving multi-band MTM-assisted SIPDT systems were proposed to improve both power and data transmission. Due to time and resource limitations, and especially the outbreak of COVID-19 pandemic, experimental implementations and verification of the proposed lenses, reflectors and system could not be conducted.

## 1.5

### Research impacts and milestones

- *Physically meaningful analytical models of the magnetic link in complex media*  
The attenuation of MI waves in lossy matter (saltwater or underground) is smaller than RF transmissions, but the abstraction of the actual models cannot properly explain the interaction of the MI waves with these media or establish its fundamental limits. A model describing the Poynting vector along the transmission clarifies these points.
- *Lossy-media robust broadband MTM lenses*  
MTM lenses with increased bandwidth can introduce a net PTE gain to the system without degrading its throughput. Besides, a better theoretical and practical understanding of the near-field focusing mechanism in seawater will contribute to the design of MTM lenses in any sort of lossy media.

- *Integrated solution for UD-based data platforms*

A transceiver architecture that can handle power and data transfer in both ways (from the BS to the UD and from the UD to the BS) will accelerate the implementation of the UDs as data platforms.

- *Systematize the design and the scaling of UD-assisted UWSN*

Considering the major aim of the actual development of the so-called Internet of Things (IoT) is to turn these systems pervasive and ubiquitous, the generalization of UWSN will facilitate its integration with other similar networks in aerial and terrestrial environment.

The main milestones of this research project can be summarized as follows:

- **M1. Development of physically insightful analytical models of the magnetic channel that can easily incorporate different SIPDT compensation topologies and the interaction with complex media (such as MTMs and/or saltwater)**
- **M2. Design and implementation of MTM lenses and reflectors with high gain and low seawater, eddy-current related losses**
- **M3. Proposal of cost-effective UD transceiver architecture for UWSN applications**

## 1.6

### Thesis structure

This thesis is organized as follows:

In **Chapter 1 – Introduction**, it is presented the general context of UWSN and IoUT assisted by UDs, the motivation and the objectives of this research, highlighting the relevance of the proposed study, its expected benefits to the field and the employed methodology.

In **Chapter 2 – Literature review**, a concise literature review on the main subjects related to this thesis is presented, including the fundamentals of the theory of metamaterials.

In **Chapter 3 – Inductive channel modelling based on VMGTL**, the theory of virtual magnetic transmission lines (VMGTL) is reviewed and extended for multiple MTM lenses and large-scale systems. The main results of this chapter were published in [27-28].

In **Chapter 4 – MTM design for underwater SIDPT applications**, it is presented the design strategies of MTM lenses and reflectors considering the deterioration of the MTM gain due to the high salinity of the seawater.

In **Chapter 5 – Modulation scheme for efficient MTM-assisted SIDPT**, phase and frequency modulation scheme are evaluated for efficient MTM-assisted SIDPT applications.

In **Chapter 6 – Final comments and conclusion**, it is summarized the proposed strategies for efficient and cost-effective SIDPT with MTMs for UD-assisted UWSN. Furthermore, it is presented the list of main contributions of the thesis to the research topic and envisioned future works.

In **Annex A – Published and accepted works**, it is summarized the works that were published during the realization of this thesis.

In **Annex B – Student design competition award**, it is presented the IPT prototype, conceived at PUC-Rio, that received the First Place Award in Student Design Competition for Wireless Power Transmission Consumer Electronics Application, from IEEE Microwave Theory and Technique Society (MTT) at the 2017 International Microwave Symposium (IMS 2017).

In **Annex C – MATLAB code**, it is presented the MATLAB code that was used to obtain the results presented in section 3.3.

## 2

### Literature review

#### 2.1

##### Fundamentals of the theory of metamaterials

MTMs are structures designed to synthesize some macroscopic properties of materials. Since these properties are created artificially, it permits a robust wave control without requiring shaping conventional materials in complicated ways. Besides, it permits the synthesis of some rare or even inexistent material properties, such as negative mass, negative magnetic permeability or negative thermal expansion coefficient [29-31].

Even though nowadays MTMs have found applications in almost all engineering domains, they were firstly proposed in electromagnetism. From the point of view of electromagnetics, MTMs consist of a set of electromagnetic (EM) circuits called unit cells, depicted in Figure 2.1. The MTM unit cells can be composed of both passive and active elements, since they are much smaller than the working wavelength (at least 10 times). If so, the incoming EM field will interact with the MTM analogously to a homogeneous medium. Thus, the effects of the MTM on the EM fields (such as wave dispersion, diffraction and/or scattering) can be fully described in terms of effective parameters.

As shown in Figure 2.2, the EM materials can be classified into four categories, according to their effective parameters:

- Electric Negative (ENG):  $\epsilon < 0$  and  $\mu > 0$  (electric plasma);
- Magnetic Negative (MNG):  $\epsilon > 0$  and  $\mu < 0$  (magnetic plasma);
- Double-Positive (DPS):  $\epsilon > 0$  and  $\mu > 0$  (conventional materials);
- Double Negative (DNG):  $\epsilon < 0$  and  $\mu < 0$  (left-handed materials).

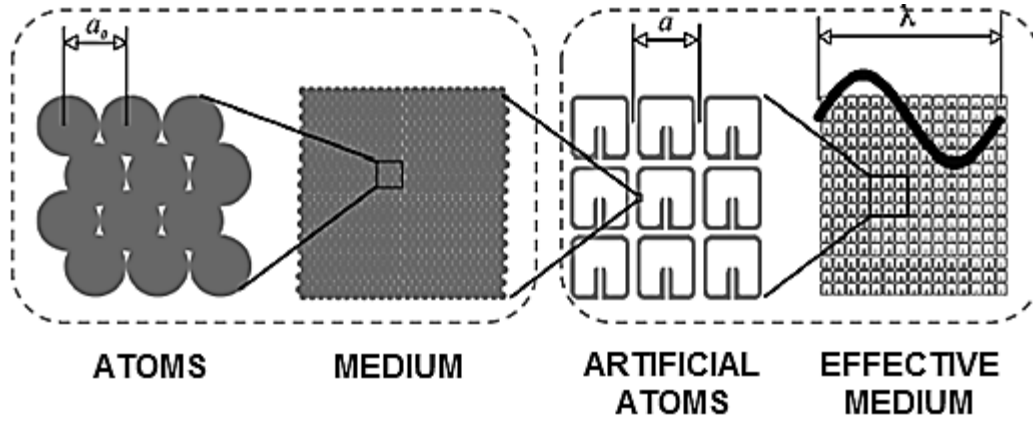


Figure 2.1: MTMs are described by effective parameters like natural materials

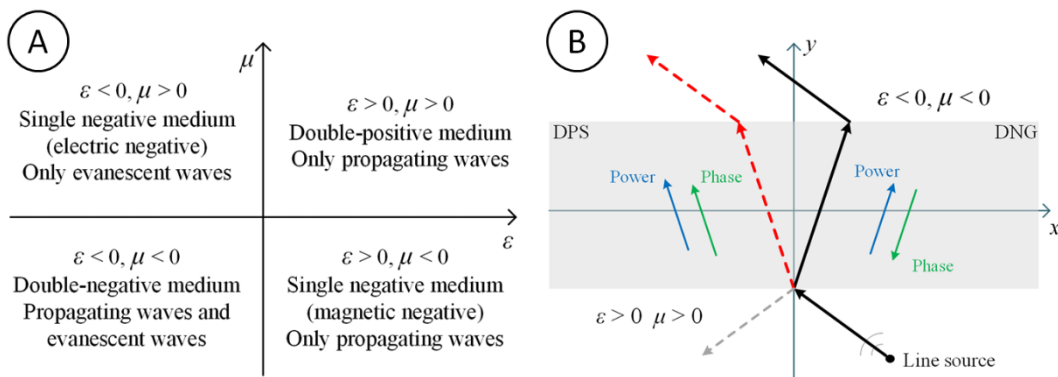


Figure 2.2: (a) Classification of the EM materials and (b) refraction on both DPS and DNG media. Notice that in DNG power flux and phase velocity are inverted

Notice that the classification presented in Figure 2.2 does not include the metamorphic state of MTMs as EM absorbers, which are characterized by  $Re\{\epsilon\} \approx Re\{\mu\} \approx 0$  and  $Im\{\epsilon\} \neq 0$  and  $Im\{\mu\} \neq 0$ , and behave as dissipative sheets [29-30]. A more complete classification should also take into consideration the chiral properties of the materials.

As it has been shown by Veselago [32], DNG and DPS media can support propagation modes, while single-negative ones (ENG and MNG) only permit evanescent solutions. This result comes directly from the fact that the refraction index  $n$  is a real number for the first cases and imaginary for the latter ones.

Based on the theory of electromagnetism, the generic coordinate  $\xi$  of the wave vector  $\mathbf{k}$  is related to the component  $n_{\xi\xi}$  of the generic complex tensor  $\mathbf{n}$ , as follows:

$$k_{\xi} = \frac{2\pi}{\lambda_m} = n_{\xi\xi} \cdot \frac{2\pi}{\lambda_0} \quad (1)$$

$$n_{\xi\xi} = \sqrt{\epsilon_{\xi\xi} \cdot \mu_{\xi\xi}} \quad (2)$$

where  $\lambda_m$  is the wavelength in the medium,  $\lambda_0$  is the wavelength in free space,  $k_\xi$  is the  $\xi$ -coordinate of  $\mathbf{k}$ ,  $\varepsilon_{\xi\xi r}$  is the  $\xi$ -direction component of the generic relative permittivity tensor  $\boldsymbol{\varepsilon}_r$  and  $\mu_{\xi\xi r}$  is the  $\xi$ -direction component of the generic relative permeability tensor  $\boldsymbol{\mu}_r$ .

By their turn, the  $\xi$ -coordinate of the EM fields are related to  $\mathbf{k}$  as follows:

$$E_\xi = E_{\xi 0} e^{-jk_\xi \xi} = E_{\xi 0} e^{-jn_{\xi\xi} \frac{2\pi}{\lambda_0} \xi} \quad (3)$$

$$H_\xi = H_{\xi 0} e^{-jk_\xi \xi} = H_{\xi 0} e^{-jn_{\xi\xi} \frac{2\pi}{\lambda_0} \xi} \quad (4)$$

where  $E_\xi$  and  $H_\xi$  are respectively the  $\xi$ -direction components of the electric-field vector  $\mathbf{E}$  and the magnetic-field vector  $\mathbf{H}$ , and  $E_{\xi 0}$  and  $H_{\xi 0}$  are their amplitudes.

From Eqs. (3) and (4), it is evident that only a real  $n_{\xi\xi}$  supports propagation, otherwise the fields will exponentially decay. Also, it can be seen that the negative sign of  $n_{\xi\xi}$  will change the phase-rotation of the fields. To understand this phenomenon, let us suppose the interface of two media ( $n = 1$  and  $n = -1$ ). Since the magnitudes of their  $n$  are the same, there will be no reflection at the interface, so that the incident EM wave must maintain its propagation direction, when passing from the DPS to the DNG. Nonetheless, its spatial phase rotation  $\frac{\partial \varphi_\xi}{\partial \xi}$  will change direction.

The spreading of the EM field due to spatial phase gain is a necessary condition for propagation, but it can be reversed by the negative material since it is going to gain phase backwardly. In other words, phase velocity  $v_p$  will invert its direction in relation to the group velocity  $v_g$  (in normal dispersion) or the signal velocity  $v_s$  (in anomalous one).

$$v_{p\xi} = \frac{\omega}{k_\xi} \quad (5)$$

$$v_{g\xi} = \frac{d\omega}{dk_\xi} \quad (6)$$

$$v_{s\xi} = \frac{\mathbf{S}}{\mathbf{u}} \quad (7)$$

where  $\omega$  is the angular frequency,  $\mathbf{S}$  is Poynting vector and  $\mathbf{u}$  is the total energy density of the EM fields.

This is why DNG materials can be used as a sort of lens and are commonly referred as left-handed media, since the relationship between vectors  $\mathbf{E}$ ,  $\mathbf{H}$  and  $\mathbf{k}$  is given by

$$\text{dir}(\mathbf{E} \times \mathbf{H}) = \text{dir}(-\mathbf{k}) \quad (8)$$

Notice that Eq. (8) shows that the right-hand rule is no longer applicable.

The equivalent material properties of MTMs depend on the response of each unit cell to an incident EM field as well as on the mutual coupling between the neighboring cells, which is a function of their spatial organization since it directly affects the behavior of the scattered fields [33]. Spatially, the unit cells can be disposed in four ways: 1) periodically (artificial crystal lattice), 2) orderly but not periodically (artificial quasicrystal), 3) hyperuniform disorderly [34] and 4) randomly (artificial amorphous solid). In the case of periodical MTMs, assuming that the unit cells are close (lattice constant  $\Lambda$  much smaller than  $\lambda_0$ ), the entire structure can be characterized based exclusively on their unit cells equivalent parameters [31]. Various homogenization techniques have been developed for the extraction of the MTM properties, like electric permittivity  $\epsilon$  and magnetic permeability  $\mu$ . In [35], S-parameters are used to determine the equivalent of the unit cells. However, S-parameters based techniques find their limit when nonreciprocal cells ( $S_{21} \neq S_{12}$ ) are considered. In [36], alternative techniques that can deal with these cases are presented.

Based on MTM theory, higher-order unit cells can be created out of lower-order ones. A second-order MTM unit cell for subwavelength antenna insulation at PEC boundaries is presented in [37], considering the perfect electric conductor (PEC) boundary conditions. Besides, a new sort of MTM, usually called metadvice, is presented in [38], adding active elements to the unit-cell design, aiming to make MTMs reconfigurable and functional.

## 2.2

### Fundamentals of inductive power transfer

#### 2.2.1

##### Magnetic coupling

Wireless power transfer (WPT) systems are composed of a transmitting unit that converts its electrical energy into EM fields, with the purpose to serve as the primary power source of one or more receivers. WPT can be divided in two major groups: far-field and near-field based systems, as highlighted in Figure 2.3. In far-field WPT, power is transferred by means of propagating EM waves. On the other hand, in near-field WPT, the transmitter and its receivers are deliberately conceived to be electrically small antennas (ESAs) generating a quasistatic field in

the intervening space, that transfers power by means of inductive or capacitive coupling between the drivers [39].

In particular, an IPT system is a type of WPT, based on magnetic coupling  $\kappa_m$ , that operates in the reactive near field (see Figure 2.4) [40]. Basically, it consists of electrical loops that convert electromotive force (EMF) into magnetic flux and vice-versa, as described by Maxwell's third equation (Maxwell-Faraday-Lenz's Law) [41]:

$$EMF = \oint E \cdot dl = - \iint J_m ds \quad (9)$$

where  $E$  and  $J_m$  are, respectively, the electric field and the magnetic current density in their complex spatial form.

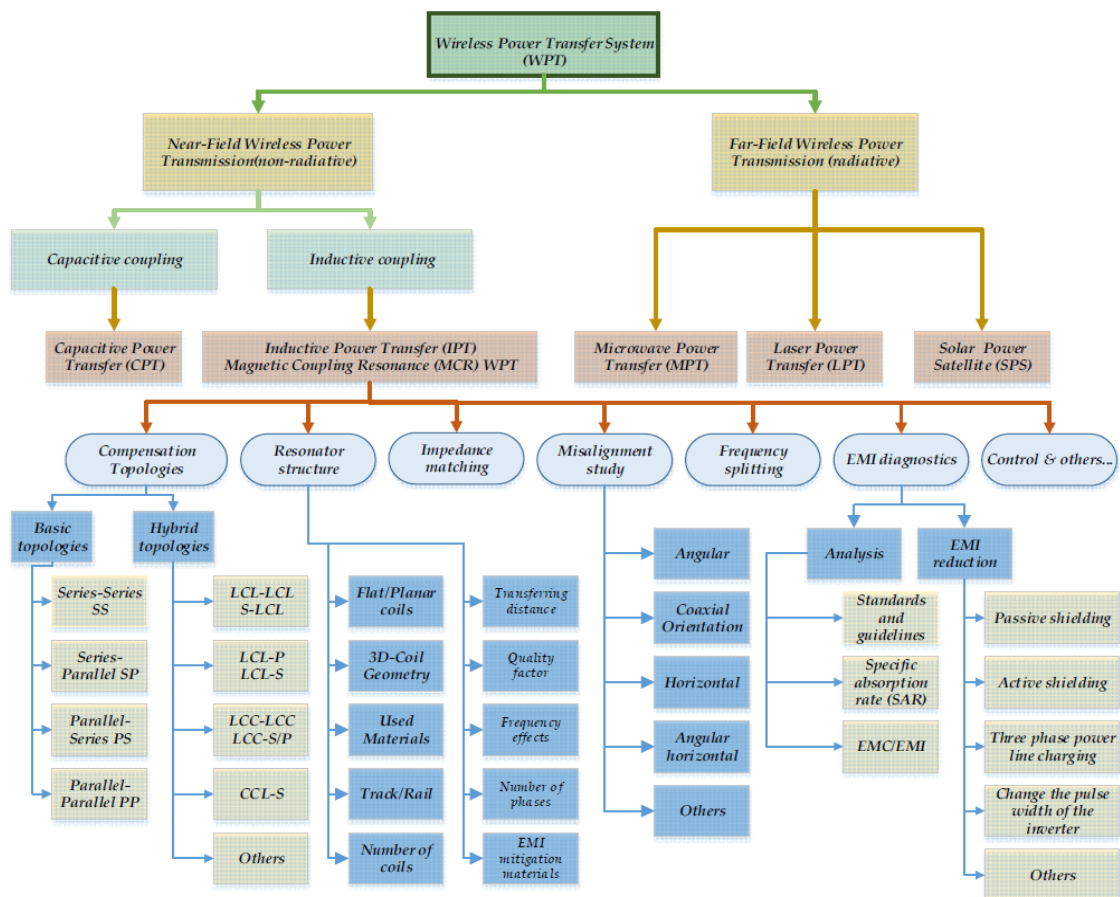


Figure 2.3: WPT main technologies and research areas [42]

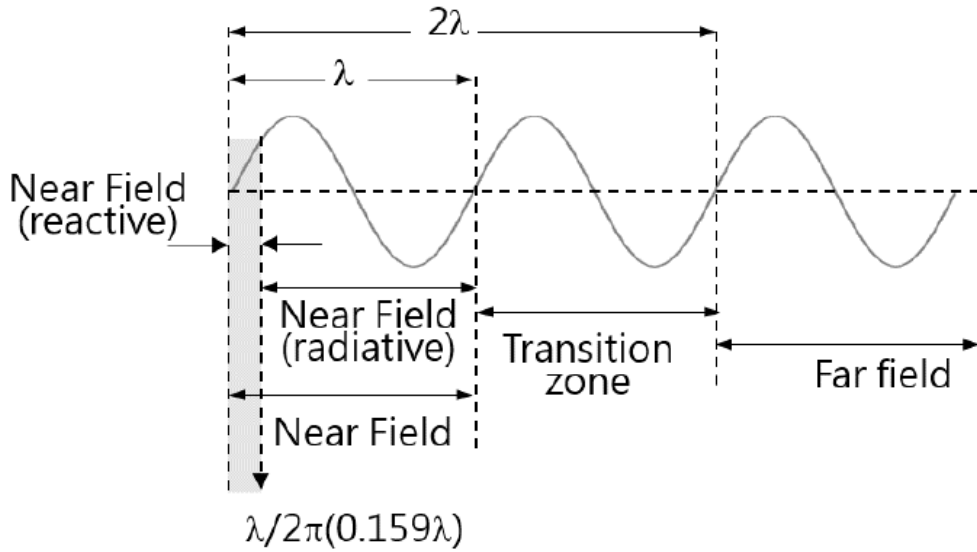


Figure 2.4: Antenna field regions

This sort of system has been used as electric transformer in power distribution system since Tesla [39]. However, it can only be used in a short range for two reasons. First, the radius of the reactive near-field region  $r_{NF}$  is limited by the wavelength  $\lambda$ :

$$r_{NF} < \frac{\lambda}{2\pi} \quad (10)$$

and secondly, the EM near field is dominated by evanescent modes, transferring power by means of mode coupling. Since  $\kappa_m$  between the drivers decays exponentially with the separation distance  $D$  between them, in RF frequency, operating distance is typically limited by  $\kappa_m$  since any practical value  $\kappa_m$  with non-negligible PTE implies  $D \ll r_{NF}$ . Figure 2.5 shows the theoretical  $r_{NF}$  as a function of the frequency. Notice that only after tens of *MHz* the near-field region starts to become small enough to be a concern for designers.

Using the conventional circuit theory (transformer approximation) [43], the PTE of IPT systems is given by the ration between the power delivered to the load (PDL) and the input power ( $P_{IN}$ ):

$$PTE = \frac{PDL}{P_{IN}} = \frac{R_L(\omega M_{RX-TX})^2}{Z_{RX}(Z_{TX}Z_{RX} + (\omega M_{RX-TX})^2)} \quad (11)$$

$$M_{RX-TX} = \kappa_m \sqrt{L_{TX}L_{RX}} \quad (12)$$

where  $R_L$  is the load resistance,  $Z_{TX}$  and  $Z_{RX}$  are the impedances of the primary and secondary coils,  $L_{TX}$  and  $L_{RX}$  are the inductances of these same coils and  $M_{RX-TX}$  is the mutual inductance of the drivers.

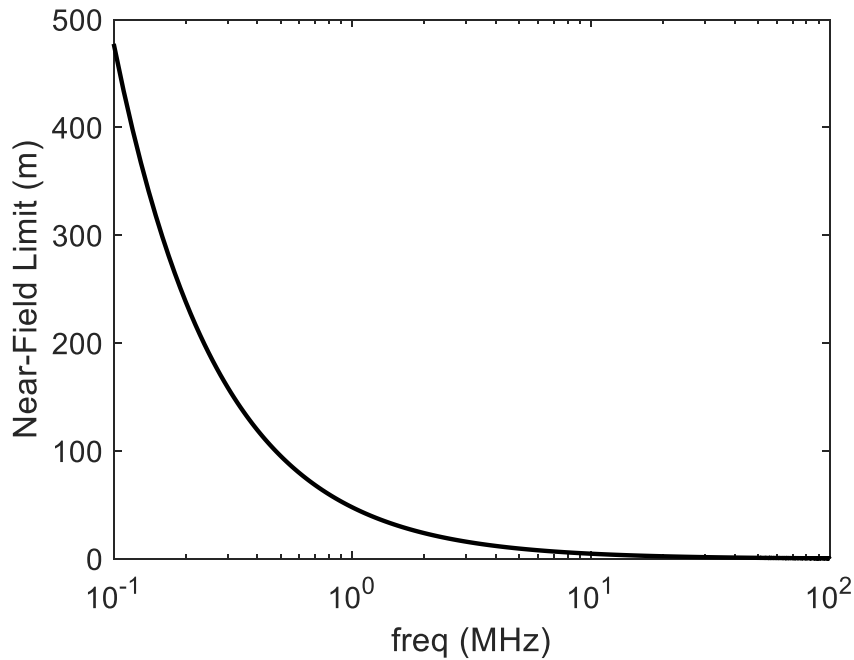


Figure 2.5: Near-field limit  $r_{NF}$  as a function of the frequency

Equation (11) establishes that PTE is directly proportional to the square of  $\kappa_m$  for magnetically coupled circuits. Consequently, it reaches high values only for  $\kappa_m$  quite close to the unity. Besides that, since the coupling depends basically on the amount of ongoing and outgoing magnetic flux through the area of the coils, IPT is very sensible to misalignments. Furthermore, the coupling also tends to decrease when the primary and secondary coils do not have the same geometry.

### 2.2.2

#### Resonant magnetic coupling

In the last decade, IPT became popular on WPT research for consumer electronics applications, because efficient mid-range IPT has been proved to be possible by using RMC. In [44], an IPT system at 9.9 MHz powered a 60 W lamp up to a distance of 2 meters, with 40% of PTE. RMC-based IPT, also called strong coupling magnetic resonance (SCMR), uses a four-coil topology with two intermediary coils in resonance in order to compensate the losses of loosely coupled coils [42]. Both conventional and resonant IPT have the same basic configuration, shown in Figure 2.6.

Using the coupled mode theory (CMT) and assuming a series-series compensation topology [44], it can be shown that the PTE of such systems is given by:

$$PTE = \frac{PDL}{P_{IN}} = \frac{4\kappa_m^2 Q_{TX} Q_{RX}}{\left( \left(1 + \frac{R_i}{R_{TX}}\right) \left(1 + \frac{R_L}{R_{RX}}\right) + \kappa_m^2 Q_{TX} Q_{RX} \right)^2} \cdot \frac{R_i}{R_{TX}} \frac{R_L}{R_{RX}} \quad (13)$$

where  $Q_{TX}$  and  $Q_{RX}$  are the quality factors of the coils, and equal to  $Q_S = \frac{1}{R} \sqrt{\frac{L}{C}}$  and  $Q_P = R \sqrt{\frac{C}{L}}$  for RLC series and RLC parallel circuits, respectively.

In brief, strong-coupled regime compensates the decreasing of  $\kappa_m$  by increasing the Q-factor of the coils. RMC has the virtue of being quite robust to misalignment between the coils [45]. However, this approach also has limitations. As discussed in [46], high-Q coils imply more complex and expensive systems, since the high-efficient bandwidth is exceedingly small, demanding powerful frequency-tracking mechanisms. Moreover, since RMC is phase-dependent, maximum PTE and PDL cannot be achieved simultaneously in such systems, leading to frequency splitting [47].

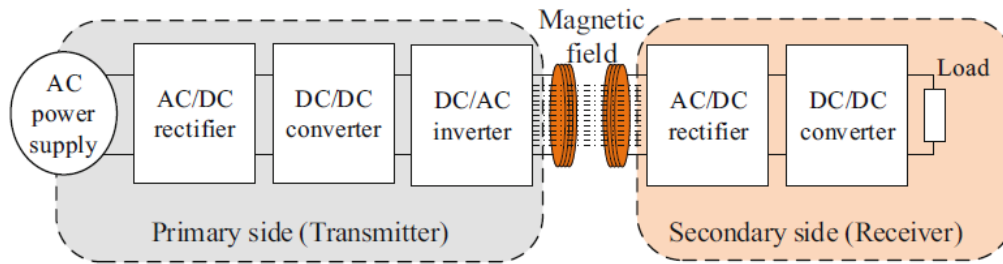


Figure 2.6: Block diagram of a typical IPT system configuration [26]

### 2.2.3

#### IPT systems in seawater

In [48], it is shown that IPT efficiencies in air and freshwater are basically identical but results also indicate that in seawater the system performance will be degraded in higher frequencies (above hundreds of kHz) due to induced eddy currents. The PTE variation with the salinity in underwater IPT is better investigated in [49], where authors shown that the optimum operating range decreases as salinity increasing due to the equivalent high conductivity  $\sigma$  of the water, which affects the unload Q-factor of the coils. For environments with high salinity like the ocean, they point out that the operating frequency range must not exceed 200 kHz. In [50], authors come to a similar conclusion.

## 2.2.4

### Compensation topologies

Figure 2.7 presents the many topologies employed in IPT systems. Besides, Figure 2.8 shows the four basic types of compensation topologies used by IPT systems: series-series (SS), parallel-parallel (PP), series-parallel (SP) and parallel-series (PS) [26].

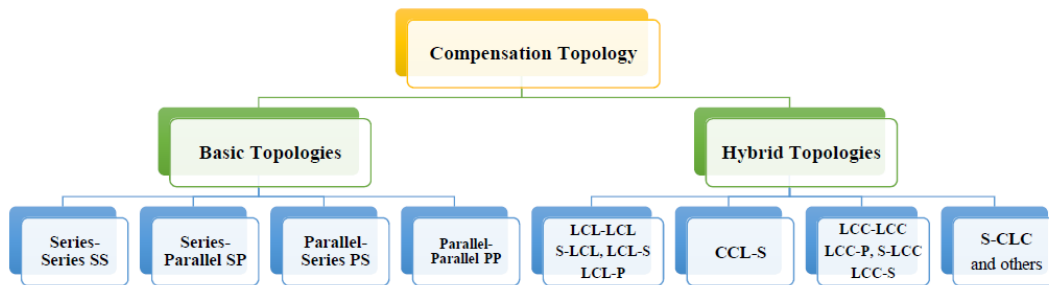


Figure 2.7: Classification of the compensation topologies [42]

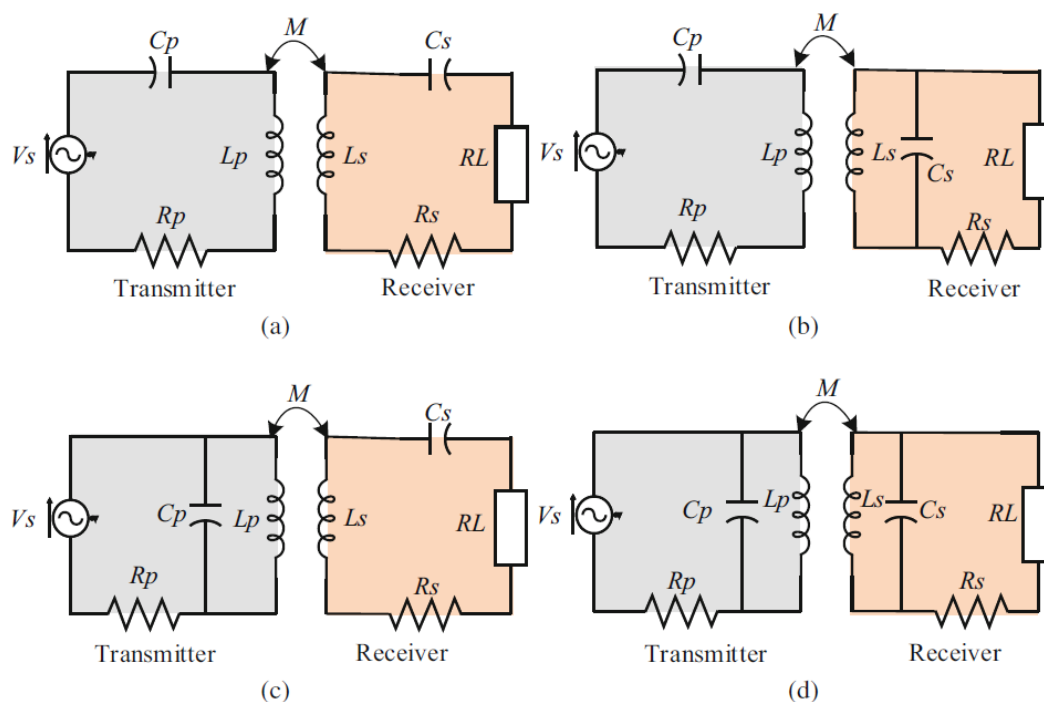


Figure 2.8: The four basic compensation topologies of IPT systems: (a) SS, (b) SP, (c) PS and (d) PP [26]

In SS, the primary and secondary capacitors can be designed to resonate with the equivalent leakage inductance of the system to increase the active-reactive power ratio (improved power factor). The drawback of this configuration is its weak misalignment tolerance. In PP, the misalignment tolerance is stronger

than in other topologies, but with the drawback of presenting the lower power output capacity (POC) due to higher reflected reactances. In SP, the high reflected impedance of the parallel-compensated secondary circuit can be minimized by adjusting the capacitor inserted in the primary one. This configuration is, hence, advantageous to deal with large loads. Nonetheless, it is more sensitive to frequency variations and to the decreasing of the coupling coefficient. In PS, as well as in PP, the reflected impedance depends on both the mutual inductance and the load.

Besides the basic compensation topologies, novel compensation topologies have been proposed, based on combinations of the basic ones such as SP/S, S/SP or S/PS, or T-type and  $\pi$ -type networks, such as inductor/capacitor/capacitor (LCC) or inductor/capacitor/inductor (LCL), shown in Figure 2.9 [42]. These hybrid topologies can achieve a better trade-off between POC, PTE and misalignment tolerance. Particularly, in the last decade most designers concentrated their efforts on the investigation of the double-sided LCC. This topology has high-misalignment tolerance and can easily achieve zero-voltage switching (ZVS) and zero phased angle (ZPA) conditions. ZVS sets the PA block losses to a minimum, while ZPA assures no resistance bifurcation avoiding the frequency splitting phenomenon.

The main drawback of LCC-LCC compensation is the high number of components required, increasing the size and cost of the system. In this way, aiming to minimize the complexity of LCC-LCC, a novel LC/S compensation topology, presented in Figure 2.10, has proved to be simpler and to have a similar performance [51].

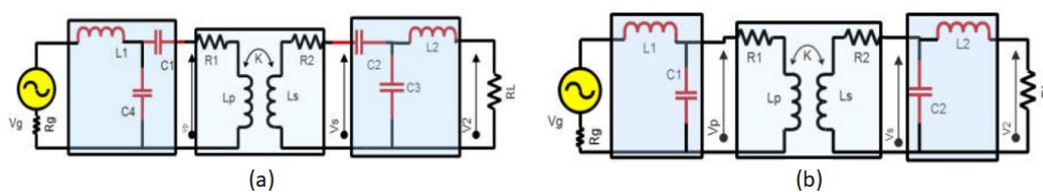


Figure 2.9: (a) Double-sided LCC and (b) double-sided LCL topologies [42]

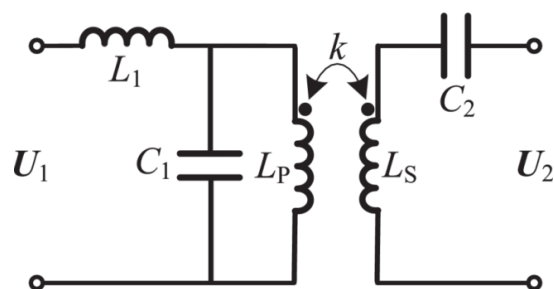


Figure 2.10: LC/S compensation topology

Nevertheless, considering applications where not only power but also data must be transferred, other problems than the cost/size of the system must be taken into consideration. Particularly, it should be considered the transient delay  $t_d$  imposed by the chosen compensation topology. To avoid that the transient process interferes with data, the symbol period  $T_s$  must be always much longer than  $t_d$ , as exemplified in Figure 2.11. As pointed out in [52], transient distortion will be negligible if:

$$T_s \geq 2t_d \quad [s] \quad (14)$$

Consequently, the maximum achievable symbol rate  $R_s$  and bit rate  $R_b$  are:

$$R_s = \frac{1}{T_s} = \frac{1}{2t_d} \quad [symbols/s] \quad (15)$$

$$R_b = R_s \log_2 M \quad [bits/s] \quad (16)$$

where  $M$  is the number of symbols of the chosen modulation scheme.

Based on the transient criterium, PP typically presents the better performance (shorter  $t_d$ ) among all compensation topologies (including the hybrids) while SS presents the worst. This fact becomes obvious by remembering that the transient response of parallel RLC circuits is  $t_{d_p} \approx 8RC$ , while the series RLC one is  $t_{d_s} \approx 8\frac{L}{R}$  [52]. Therefore, since IPT systems are characterized by  $L \gg C$  and low  $R$ ,  $t_{d_s} \gg t_{d_p}$ .

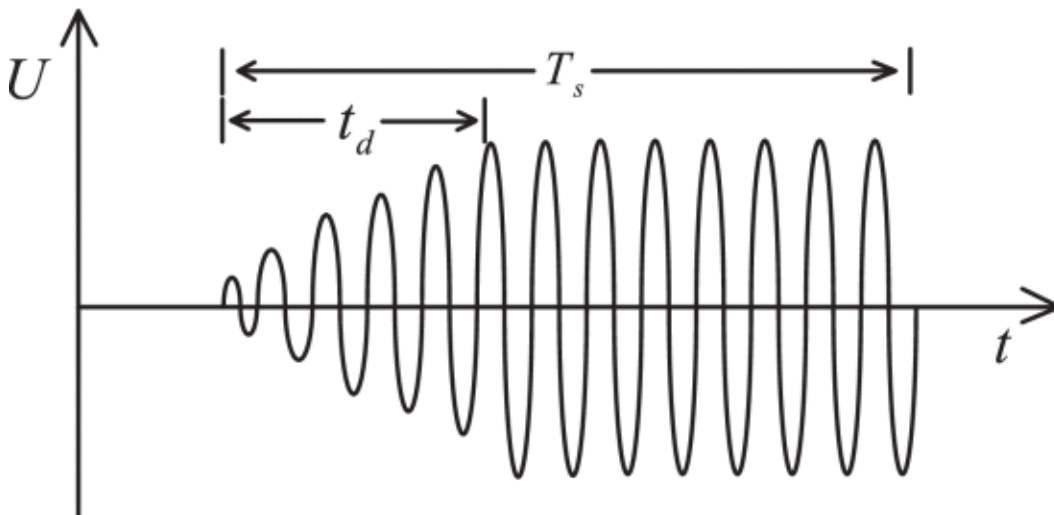


Figure 2.11: Symbol period  $T_s$  must be long enough to ensure that transient effects of the system are negligible

## 2.2.5

### Metamaterial-enhanced inductive power transfer

Alternatively to RMC, MNG MTM-based lenses have been proposed as a mean to enhance the PTE of IPT systems [46, 53-56]. Many of these publications explain the MTM-enhanced coupling by using the perfect lensing concept introduced by Pendry [31], depicted in Figure 2.12. Perfect lensing interpretation is based on transformational electromagnetics (TE) [57]. According to TE, the EM-wave medium changing is equivalent to spatial transformation in free space for EM fields, because of the well-known invariance of the Maxwell's equations under relativistic transformations. In this approach, MNG MTMs act as a space where the EM field spatial phase decreases instead of increasing.

In [27], VMGTL theory was employed to clarify the functioning of the MTM-enhanced coupling. In VMGTL approach, the apparent enhancement of the magnetic coupling is due to the improvement in the impedance matching between the primary and secondary drivers. The MNG MTM acts as band-limited non-foster virtual impedance, reducing the reactance of the magnetic channel. By filtering the higher-order modes of the magnetic flux, the magnetic potential of the VMGTL is increased as well as the real part of the Poynting vector, leading to higher PTE.

In [58], MTMs have also been proposed to synthesize magnetic shields or reflectors (see Figure 2.13). Zero-index reflectors can be used to spatially confine the magnetic flux between IPT transceivers, increasing the PTE and reducing the specific absorption rate (SAR) of the system.

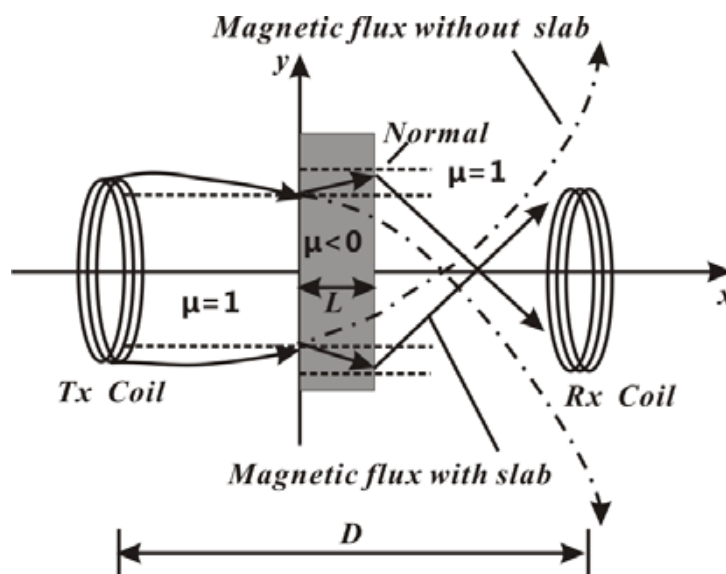


Figure 2.12: MTM-based focalization of the magnetic-field evanescent modes

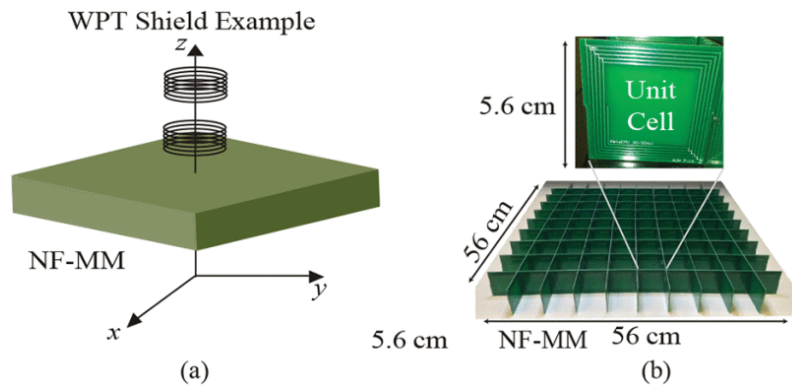


Figure 2.13: MTM-based magnetic shielding or reflector: (a) relative position on the inductive link and (b) prototype using SR cells [58]

## 2.3

### Magneto-inductive waves and MTM-enhanced coupling

The discovery of MI waves was a by-product of metamaterial research. The artificial crystal used to synthesize the first MTM-based lens was composed of SRR cells, that are capacitively loaded loops that support the propagation of a surface wave (MI waves), by means of magnetic coupling with neighbor cells. These MI waves, a sort of slow wave, received a lot of attention since they were first proposed, including the investigation of their dispersion characteristics and modulation properties [59].

The real and imaginary components of the dispersion relation of MI waves in axial and planar orientations (see Figure 2.14) are respectively given by [59]:

$$1 - \frac{\omega_0^2}{\omega^2} + \kappa_m \cos(\beta a) \cosh(\alpha a) = 0 \quad (17)$$

$$\frac{1}{Q} - \kappa_m \sin(\beta a) \sinh(\alpha a) = 0 \quad (18)$$

where  $a$  is the array periodicity, and  $\alpha$  and  $\beta$  are the attenuation and propagation (phase) constants, respectively.

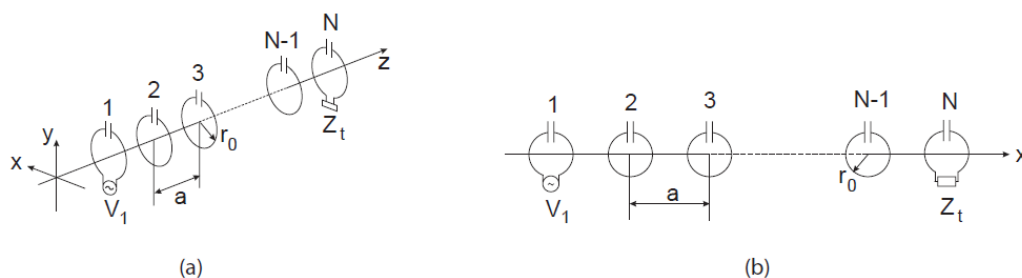


Figure 2.14: (a) Axial and (b) planar orientations [59]

Figure 2.15 shows the dispersion for 1-D axial array, with  $\kappa_m = 0.1$ , and Figure 2.16 shows the dispersion for 1-D planar array, with  $\kappa_m = -0.1$ . Notice that the behavior of the curves presented in the left graphs of Figure 2.15 and Figure 2.16 are inverted in relation to each other, but the same thing does not happen in the right graphs. This is because  $\beta$  is related to the real component of the dispersion relationship, given by Eq. (17), while  $\alpha$  is related to the imaginary one, given by Eq. (18). In Eq. (17), we see that  $\kappa_m$  multiplies an even function, so the derivative of  $\beta$  will rely on the sign of  $\kappa_m$ . In Eq. (18), we see that  $\kappa_m$  multiplies an odd function, whose sign depends on  $\kappa_m$ , making  $\alpha$  insensitive to the sign of  $\kappa_m$ .

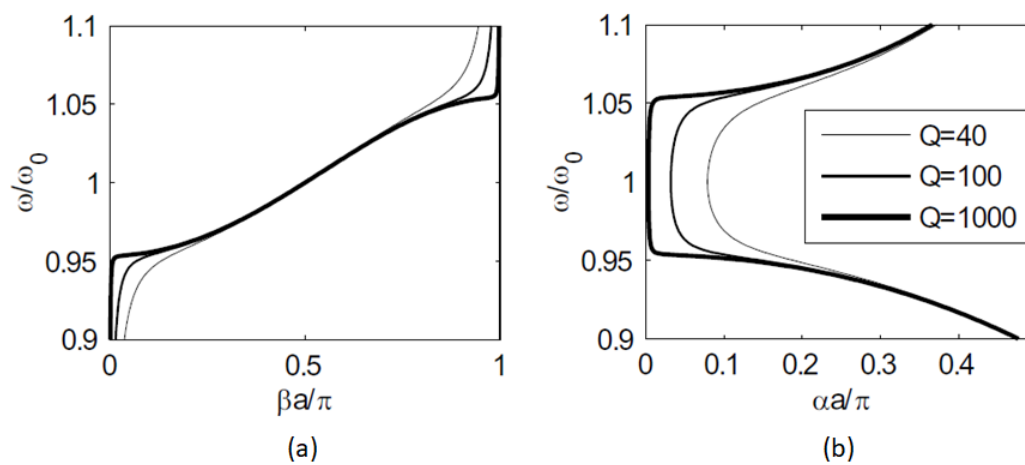


Figure 2.15: Dispersion for 1-D axial array with  $\kappa_m = 0.1$ : normalized (a)  $\beta$  and (b)  $\alpha$  [59]

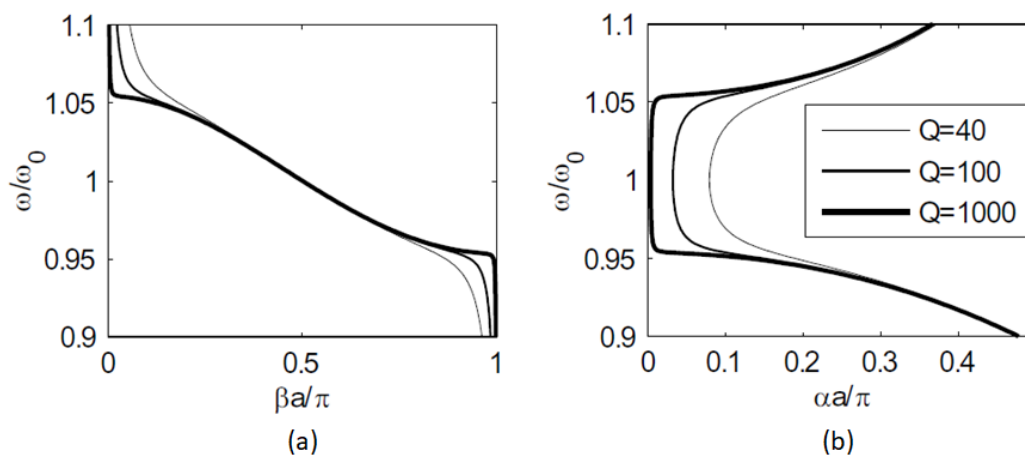


Figure 2.16: Dispersion for 1-D planar array with  $\kappa_m = -0.1$ : normalized (a)  $\beta$  and (b)  $\alpha$  [59]

Similarly, MI-wave solution can be found for two-dimensional (2D) arrays of loaded loops. In that case, their dispersion relation is given by [60]:

$$\frac{\omega_0}{\omega} = \left(1 + \kappa_{mx} \cos(\gamma_x a) + \kappa_{my} \cos(\gamma_y a)\right)^{-\frac{1}{2}} \quad (19)$$

where  $\kappa_{mx}$  and  $\kappa_{my}$  are respectively the coupling coefficients of the cells in the horizontal and vertical direction, and the terms  $\gamma_x$  and  $\gamma_y$  are components of the complex propagation constant of the 2D-MI wave.

The following condition should be attended for the generation of propagating waves:

$$|\gamma_x a| \ll 1 \text{ and } |\gamma_y a| \ll 1 \quad (20)$$

As it was demonstrated in [61], using the prototype built during the initial stages of this thesis, shown in Figure 2.17, MTM-enhanced coupling phenomenon arises directly from the interactions of MI waves supported by the MNG MTM. These are essentially a type of surface waves supported by the 2D-array of loaded loops, illustrated in Figure 2.18. The incident magnetic field excites MI waves on the MTM surface, which is analogous to magnetic currents and supports source-free fields (that is, fields that exist independently of the source). The other evanescent modes still coming from the driver coil strongly couple to those free fields at the MTM interface, taking energy from them and, consequently, generating an amplification process, equivalent to a band-limited non-foster impedance matching [27]. Since MI wave propagation is a collective behavior, it is much more tolerant to fabrication defects or misalignments. Besides that, as mention in chapter 1, MI-based data transmission has been shown to be quite efficient in highly lossy environments due to its surface-wave nature [62-63].



Figure 2.17: Developed MTM-integrated driver using a unit-cell with spacing varying according to a Fibonacci sequence

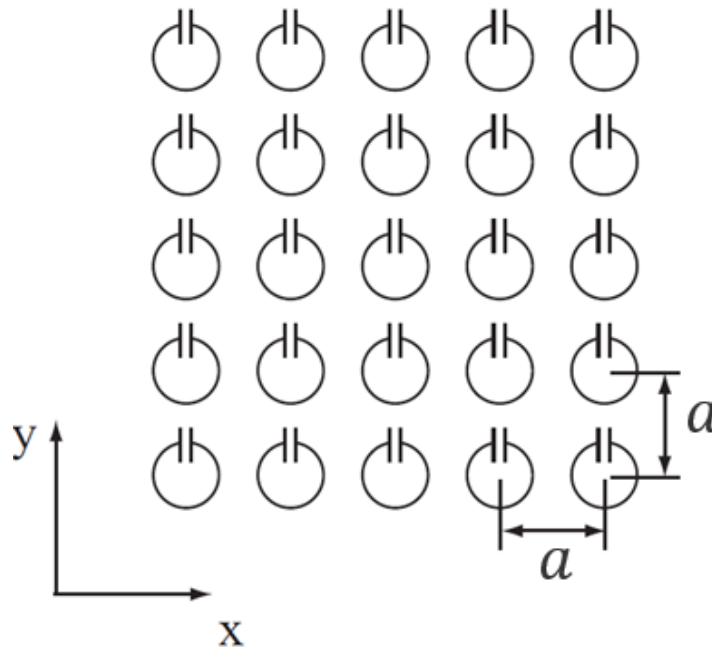


Figure 2.18: Schematic representation of a MNG MTM as 2D-array of loaded loops

## 2.4

### Final considerations

In this chapter, the main subjects related to this thesis were introduced. Considering IPT systems, the two most usual mechanisms employed for PTE enhancement, the strong coupling regime of the RMC and MTM slabs, are shown to rely both on high-Q circuits to compensate the decaying of  $\kappa_m$ . Nonetheless, due to their crystal-like structure, which supports the propagation of surface waves known as MI waves, MTMs also present a sort of lattice gain mechanism. Besides that, based on the literature of MTMs, both artificial magnetic lenses and reflectors based on MTMs have proven to be effective PTE enhancement mechanisms for IPT systems. Finally, for simultaneous power and data transmission, the compensation topologies employed in most IPT systems were shown to be limited not only by PTE, maximum PDL and misalignment issues but also by their transient delay, meaning that complex topologies, such as LCC-LCC or LC/S, could be disadvantageous despite their robustness and overall good performance.

### 3

## Inductive channel modeling based on VMGTL

### 3.1

#### Motivation

Most IPT systems are still modeled using circuit theory (transformer approximation) due to its simplicity. Nonetheless, the obtained results with this approach have huge limitations and drawbacks, especially considering the description of magnetic links. This fact has been stressed out by many works in literature, like those using more robust modeling techniques such as coupled-mode theory and bandpass filter design theory [64-65]. In [66], the small-signal phasor modeling was introduced with the advantage of avoiding complicated mathematics for obtaining the channel transfer function, especially when the compensation network includes nonlinear components such as diodes. Moreover, some researchers have also tried to bypass the use of circuit theory by characterizing the inductive channel directly through experimental measurements [67]. Yet this strategy is also quite complicated to be implemented, especially considering operating scenarios like massive MIMO-SIPDT.

Considering these issues, this thesis proposes the use of a more systematic inductive channel modeling technique based on virtual magnetic transmission line (VMGTL), which has been proposed by the thesis author as an extension of the theory of magnetic TLs for unconfined magnetic flux [68]. Like the Gyrator-Capacitor Lumped Element Model [69], VMGTL is a distributed model that also preserves the representation of the energy flow along the inductive channel. This new approach can easily integrate complex media (natural or artificial) interferences to the channel and be easily scalable to multi-coil applications (multi-channel scenario). Differently from other techniques, that derives the behavior of the channel from the behaviors of the coils' circuitry, VMGTL models the channel independently as a virtual transmission line (TL).

## 3.2

### Theoretical aspects

#### 3.2.1

##### Basic equations

The main design principle of the VMGTL model is the observation that electric/magnetic fluxes and charges have the same dimension. Hence, any time-varying flux behaves as a “virtual current”, which are better known as displacement magnetic/electric currents:

$$j\omega\phi_m = j\omega \iint \mathbf{B} \cdot d\mathbf{s} = \iint j\omega\mathbf{B} \cdot d\mathbf{s} = \iint \mathbf{J}_{m,d} \cdot d\mathbf{s} = I_{m,d} \quad [V] \quad (21)$$

$$j\omega\phi_e = j\omega \iint \mathbf{D} \cdot d\mathbf{s} = \iint j\omega\mathbf{D} \cdot d\mathbf{s} = \iint \mathbf{J}_{e,d} \cdot d\mathbf{s} = I_{e,d} \quad [A] \quad (22)$$

where  $\phi_m$  is the magnetic flux,  $\phi_e$  is the electric flux,  $\mathbf{B}$  is the density of magnetic flux,  $\mathbf{D}$  is the density of electric flux,  $\mathbf{J}_{m,d}$  is the density of magnetic displacement current,  $\mathbf{J}_{e,d}$  is the density of electric displacement current,  $I_{m,d}$  is the magnetic displacement current and  $I_{e,d}$  is the electric displacement current.

Like real currents, displacement currents can also guide EM fields, as illustrated in Figure 3.1.

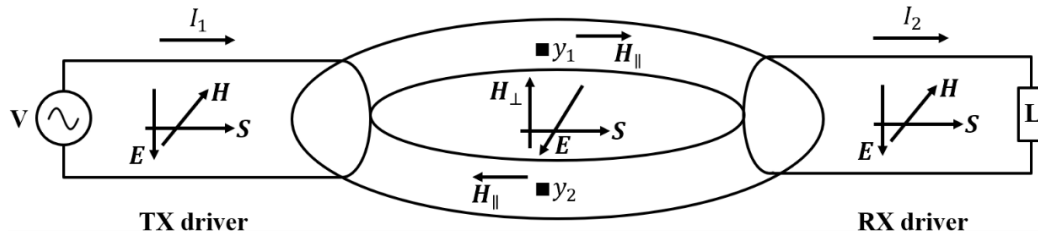


Figure 3.1: The displacement magnetic current  $I_{m,d}$ , between the TX and RX coils, forms a virtual circuit similar to a conventional TL. According to Poynting theorem, power flow in the inductive channel depends on the perpendicular component of the magnetic near field created by the magnetic potential difference between the flux in positions  $y_1$  and  $y_2$

For all purposes, a VMGTL consists of two identical insulated transmitting (TX) and receiving (RX) drivers with no physical charge flowing between them and interacting only by means of the magnetic flux. The driving force of a VMGTL is the magnetic potential  $V_m$ , given by:

$$V_m = \int_{y_1}^{y_2} \mathbf{H}_\perp(\omega) \cdot d\mathbf{l} [A] \quad (23)$$

where  $\mathbf{H}_\perp$  is the component of the magnetic field perpendicular to the magnetic flux.

The magnetic potential  $V_m$  and the magnetic displacement current  $I_{m,d}$  of the VMGTL follow propagation equations analogous to the ones of conventional TLs:

$$\frac{d}{dz} V_m(z) = \left( \frac{\mathcal{R}'_m}{j\omega} + G'_e \kappa_m^2 + j\omega C' \kappa_m^2 \right) I_{m,d}(z) = Z_m I_{m,d}(z) \quad \left[ \frac{A}{m} \right] \quad (24)$$

$$\frac{d}{dz} I_{m,d}(z) = (G'_m \kappa_m^2 + j\omega L' \kappa_m^2) V_m(z) = Y_m V_m(z) \quad \left[ \frac{V}{m} \right] \quad (25)$$

where  $Z_m$ ,  $Y_m$ ,  $\mathcal{R}'_m$ ,  $\kappa_m$ ,  $G'_e$ ,  $G'_m$ ,  $L'$  and  $C'$  denote the series magnetic impedance, the shunt magnetic admittance, the magnetic reluctance, the magnetic coupling coefficient, the electrical conductance, the magnetic conductance, the inductance and the capacitance per unit length, respectively.

Notice in Eqs. (24) and (25) that the equivalent parameters  $G'_e$ ,  $G'_m$ ,  $L'$  and  $C'$  are weighted by  $\kappa_m$ . This approximation is necessary considering that the magnetic flux and consequently  $I_{m,d}$  is unconfined. It can be seen that when  $\kappa_m \rightarrow 1$  the TL analogy becomes identical to the magnetic TLs proposed by [70] for confined-flux magnetic circuits. One important observation is that VMGTL loses its validity when  $\kappa_m$  is too low and the system gets close to the limiting case  $Y_m \rightarrow 0$ .

The equivalent circuit of the system using the VGMTL approach is presented in Figure 3.2. The characteristic electrical impedance  $Z_0$  of the VMGTL, its complex propagation parameter  $\gamma$  and its load reflection coefficient  $\Gamma$  are defined as:

$$Z_0 = \frac{I_{m,d}(z)}{V_m(z)} = \sqrt{\frac{Y_m}{Z_m}} = \sqrt{\frac{G'_m \kappa_m^2 + j\omega L' \kappa_m^2}{\frac{\mathcal{R}'_m}{j\omega} + G'_e \kappa_m^2 + j\omega C' \kappa_m^2}} \quad [\Omega] \quad (26)$$

$$\gamma = \sqrt{Z_m Y_m} = \sqrt{\left( \frac{G'_m \kappa_m^2}{j\omega} + L' \kappa_m^2 \right) \left( -\frac{\mathcal{R}'_m}{\omega^2} + \frac{G'_e \kappa_m^2}{j\omega} + C' \kappa_m^2 \right)} \quad \left[ \frac{rad}{m} \right] \quad (27)$$

$$\Gamma = \frac{Z_{RX} - Z_0}{Z_{RX} + Z_0} \quad (28)$$

where  $Z_{RX}$  is the load at the receiver.

Considering the definitions presented in Eqs. (26) to (28), the general solution of the one-dimensional Helmholtz problem defined by Eqs. (24) and (25) can be expressed as [41]:

$$I_m(z) = I_m(0) e^{-\gamma z} (1 + \Gamma e^{2\gamma z}) \quad [V] \quad (29)$$

$$V_m(z) = \frac{I_m(0)}{Z_0} e^{-\gamma z} (1 - \Gamma e^{2\gamma z}) \quad [A] \quad (30)$$

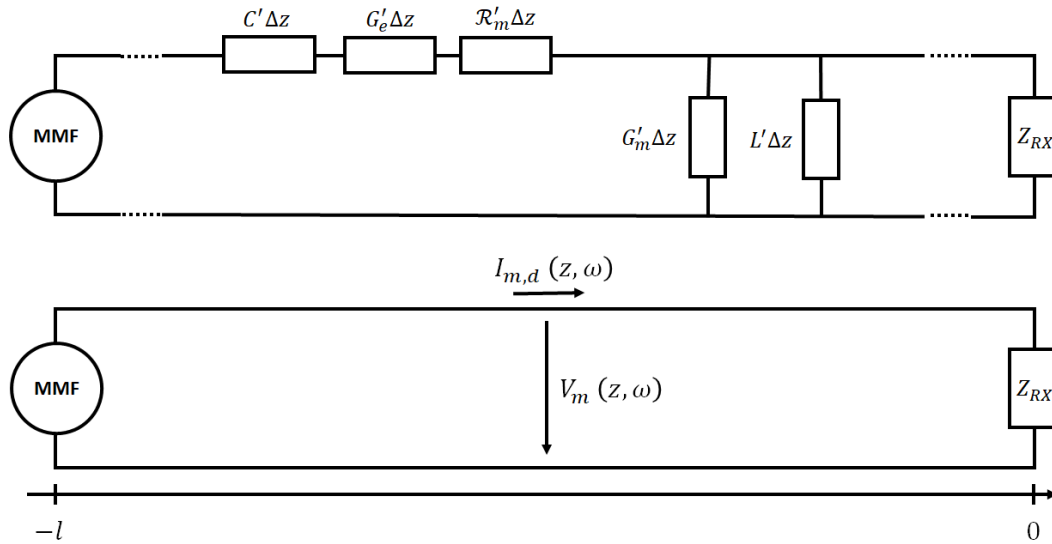


Figure 3.2: VGMTL equivalent circuit of two magnetically coupled coils

Notice that at  $V_m(-l) = I_{IN} = MMF$ , where  $I_{IN}$  is the input current, which is equivalent to the magnetomotive force  $MMF$  provided by the TX (see Figure 3.2).

Using the system's solution presented in Eqs. (29) and (30), the power flow  $P_f(\omega)$ , at any point of the inductive channel, is computed as:

$$P_f(\omega) = V_m I_{m,d}^* \quad [W] \quad (31)$$

By definition, the frequency-domain channel transfer function, which is equal to the transmission gain  $S_{21}$ , of the system is given by:

$$S_{21}(\omega) = \frac{V_m(0)}{V_m(-l)} = \frac{e^{-\gamma D}(1 - \Gamma)}{(1 - \Gamma e^{-2\gamma D})} = \quad (32)$$

where  $V_m(0)$  is the magnetic potential at the load and  $V_m(-l)$  is the magnetic potential at the source. Notice that  $D$  must be greater than the diameter of the wires of the TX and TX coils.

### 3.2.2

#### Estimation of the model parameters

To determine the five parameters presented in Eqs. (24) and (25), some simplifying hypotheses must be made. The first hypothesis assumes that the distributed elements  $G_e'$ ,  $G_m'$ ,  $L'$  and  $C'$  are uniform throughout the inductive channel, so that they can be directly estimated as follows:

$$L' = \frac{L_0}{D} \quad \left[ \frac{H}{m} \right] \quad (33)$$

$$C' = \frac{C_0}{D} \quad \left[ \frac{F}{m} \right] \quad (34)$$

$$G'_e = \omega C' \frac{Im\{\epsilon_r\}}{Re\{\epsilon_r\}} \left[ \frac{S}{m} \right] \quad (35)$$

$$G'_m = \omega L' \frac{Im\{\mu_r\}}{Re\{\mu_r\}} \left[ \frac{\Omega}{m} \right] \quad (36)$$

where  $L_0$  and  $C_0$  are the equivalent inductance and capacitance of the TX and RX coils, and  $\epsilon_r$  and  $\mu_r$  are the relative permittivity and permeability of the channel medium.

However, the estimation of distributed  $\mathcal{R}'_m$  is a little more complicated since the original concept of magnetic reluctance  $\mathcal{R}_m$  was conceived for magnetic circuits where most of the magnetic flux is confined into a ferromagnetic core, with a constant transverse section.

First, by definition,  $\mathcal{R}_m$  is given by:

$$\mathcal{R}_m \triangleq \frac{V_m}{\phi_m} \quad [H^{-1}] \quad (37)$$

Secondly, the mutual inductance  $M_{RX-TX}$  is given by:

$$M_{RX-TX} = \frac{\phi_m^{RX-TX}}{V_m^{TX}} \quad [H] \quad (38)$$

Hence, based on Eqs. (37) and (38),  $\mathcal{R}'_m$  can be approximated by:

$$\mathcal{R}'_m \propto \frac{1}{M^{RX-TX} \xi} \quad [H^{-1}] \quad (39)$$

where  $\xi$  is dimensionless geometrical weighting parameter.

Making another simplifying hypothesis, that  $\xi$  is estimated by,

$$\xi \sim r^2, \quad (40)$$

based on the educated guess that  $\xi$  is related to the effective area of the coils, the equivalent VMGTL of the system is now completely characterized.

It is important to notice that the model assumes that  $\mathcal{R}'_m$  is constant and then not a function of the spatial coordinates. Thus, the approximation will become less and less accurate if  $D/r$  increases, particularly concerning the estimation of  $\gamma$ . Another limitation regarding the model validity is that TX and RX coils should be much smaller than their resonance frequency ( $r \ll \lambda/2$ ), since radiation resistance of the drivers is assumed null.

### 3.2.3

#### MTM interaction with the inductive channel

As demonstrated in [27], the effects of the MTM on the inductive channel can be introduced to the VMGTL model by defining the equivalent distributed impedance of the MTM  $Z'_{MTM}$ . In this way, assuming MTM slabs made of a constant lattice of SR cells, the equivalent distributed  $Z'_{MTM}$  is found to be:

$$Z'_{MTM}(\omega) = j\omega\mu_0 \left( 1 + \mathbf{sign}(F) \frac{|F|\omega^2}{\omega_0^2 - \omega^2 - j\omega\omega_0/Q} \right) \left[ \frac{\Omega}{m} \right] \quad (41)$$

where  $\omega_0$ ,  $F$  and  $Q$  are its operating angular frequency, the coupling coefficient between adjacent cells of the lattice and the quality factor of the unit cells, respectively.

Hence, Eq. 25 can be rewritten as

$$\begin{aligned} \frac{d}{dz} I_{m,d}(z) &= (G'_m \kappa_m^2 + j\omega L' \kappa_m^2 + Z'_{MTM}(\omega) \kappa_{m,MTM}^2) V_m(z) \\ &= Y_m V_m(z) \left[ \frac{V}{m} \right] \end{aligned} \quad (42)$$

since the MTM changes the variation of the magnetic flux with the distance. In other words, the MTM alters the magnetic admittance  $Y_m$  of the channel. If there is more than one slab inside the link, assuming they are uncoupled, the equivalent  $Z'_{MTM}$  of all slabs will be the summation of the individual  $Z'_{MTM}$  of each MTM scaled by  $\kappa_{m,MTM}^2$ . This is due to the fact that the MTMs are perceived as impedances connected in parallel with the equivalent circuit shown in Figure 3.2.

Furthermore, the magnetic coupling between the MTM and TX and RX coils depends on the physical size of the MTM. Assuming a semi-infinite MTM plane over the transversal section of the channel, the magnetic coupling can be approximated by:

$$\kappa_{m,MTM} \cong 2\kappa_m \quad (43)$$

This simplifying hypothesis can be assumed if the MTM dimensions are at least four times larger than TX and RX coils radius  $r$ . This estimation is made based on an engineering judgment considering conventional image theory. MNG MTMs are equivalent to perfect magnetic conductors (PMCs), which means that the images of the electric currents of both the TX and RX coils will have in-phase images on the MTM's surface, which can roughly be represented by a magnetic coupling twice greater than  $\kappa_m$ .

### 3.3

#### Model validation

The considered system is composed of two electrically small far-from-resonance coils, separated by a fixed distance  $D = 15 \text{ cm}$ . The coils are made of copper, with diameter  $p = 1 \text{ mm}$ . Their self-inductance is  $L_0 = 620 \text{ nH}$  and their self-capacitance is  $C_0 = 0.28 \text{ pF}$ , which can be obtained using the small circular loop found in literature [71]. Their magnetic coupling coefficient  $\kappa_m$  can be estimated as a function of  $D$  using the thin-wire approximation [72]. The TX coil is supposed to be connected to a TL with  $Z_0 = 50 \Omega$  and TX coil is supposed to be terminated with a load  $Z_{RX} = 50 \Omega$ .

In this chapter, it will be employed a MTM identical to the one used in [27], consisting of a  $7 \times 7$  lattice of SR cells conceived on FR4 and copper ( $\epsilon_r = 4.4$ ,  $\tan \delta = 0.018$ ) with the following characteristics:

- **Outer dimensions:**  $d_{mtm1} = d_{mtm2} = 20 \text{ mm}$
- **Substrate thickness:**  $e = 1 \text{ mm}$
- **Coarse tuning element:**  $C_{SMD} = 100 \text{ pF}$
- **Conductor width:**  $w = 1 \text{ mm}$
- **Gap:**  $g = 1 \text{ mm}$
- **Diameter of the electric via:**  $d_{via} = 0.5 \text{ mm}$

The SR-based MTM prototype is shown in Figure 3.3. Knowing that SR cells are equivalent to RLC series circuits and using the same thin-wire approximation used for the estimation of  $\kappa_m$  [72], the  $Q$  of the cells and the coupling coefficient between cells  $F$  can be determined. For the validation purpose, it was considered a lattice constant  $a = 23 \text{ mm}$ , hence  $F \approx -0.43$  and  $Q \approx 100$ . The equivalent  $Z'_{MTM}$  can be estimated using Eq. 41. Notice that the slab is assumed to be at the central position between the two drivers, perpendicularly to the magnetic flux. Nonetheless, the MTM effects on the inductive link would be basically the same at any other relative position between the drivers, excluding the case where it is separated of the TX coil by a distance smaller than  $a$ .

To demonstrate the model's accuracy, the analytical channel estimation is compared with the results obtained by computational simulations performed on Advanced Design System (ADS) using the RF method of moments. These results are presented in Figures 3.4 and 3.5, that show the magnitude of the transfer

function as a function of frequency, for a VMGTL without MTM (Figure 3.4) and with MTM (Figure 3.5), for different coil radius  $r$ . Some discrepancies between analytical and numerical results exist, as expected, due to the simplifying hypotheses applied to Eqs. (37) to (40).

Besides, Figures 3.6 and 3.7 show the attenuation  $\alpha$  and propagation  $\beta$  constants as a function of frequency, for a VMGTL without and with MTM, respectively, for different coils radius  $r$ .

As shown in Figure 3.6, when there is no MTM in the channel,  $\beta$  is null and  $\alpha$  is almost independent of the frequency. In this situation, the only mechanism of power exchange between the electric interfaces is their mutual coupling. The H-field lines generated by each driver are in contact with its neighbor, inducing current according to Faraday's Law. This case can be completely characterized by means of the mutual inductance matrix and similar circuit analogies. However, if a MTM slab is introduced in the channel, independently of its relative position inside the link, other power transfer mechanism arises. Figure 3.7 shows the enhancement of the transmission gain around the MTM operating frequency  $f_0$ . This behavior is basically due to the appearance of a passband (non-null propagation constant) in the inductive link.

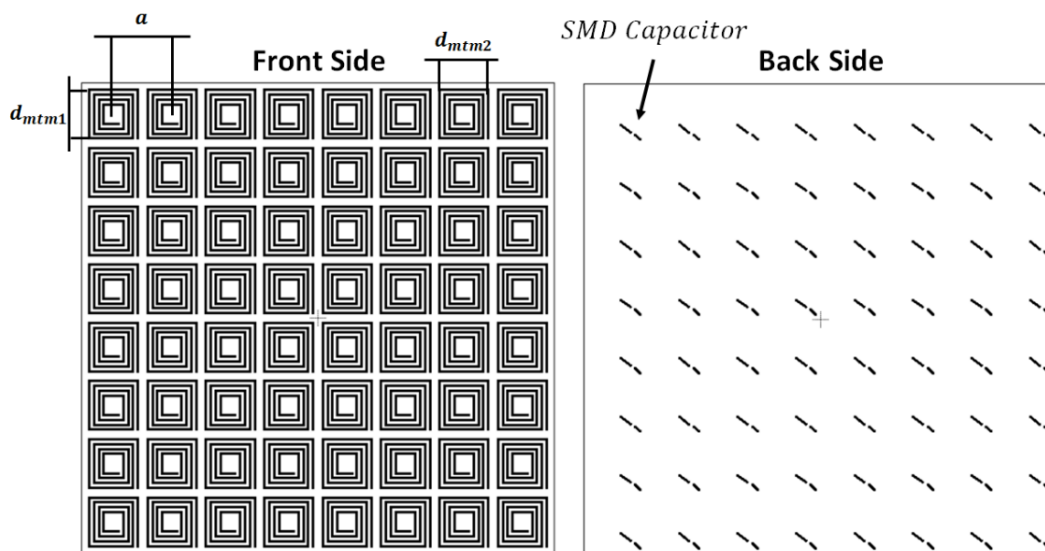


Figure 3.3: SR-based MTM prototype

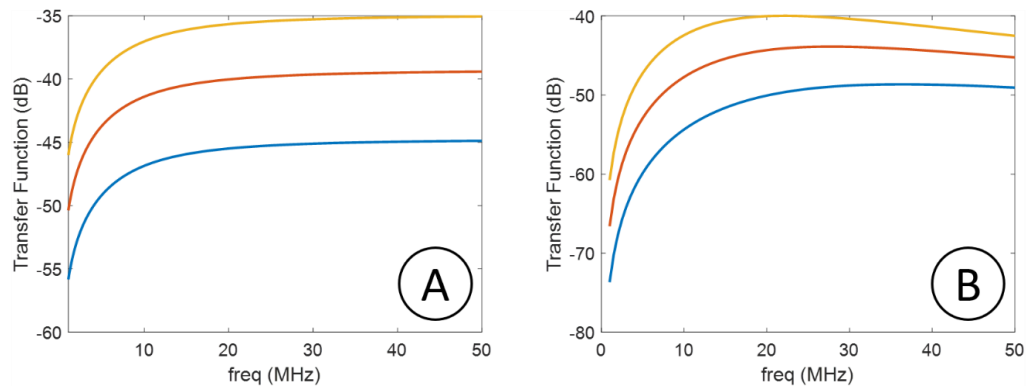


Figure 3.4: Magnitude of the transfer function as a function of frequency for a VMGTL without MTM: (a) analytical model and (b) numerical simulation, for  $r = 4$  cm (blue),  $r = 5$  cm (orange) and  $r = 6$  cm (yellow)

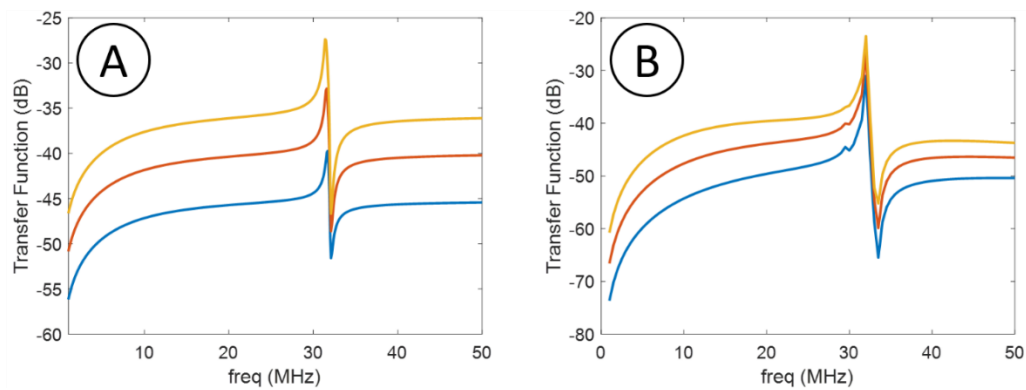


Figure 3.5: Magnitude of the transfer function as a function of frequency for a VMGTL assisted by one MTM slab: (a) analytical model and (b) numerical simulation, for  $r = 4$  cm (blue),  $r = 5$  cm (orange) and  $r = 6$  cm (yellow)

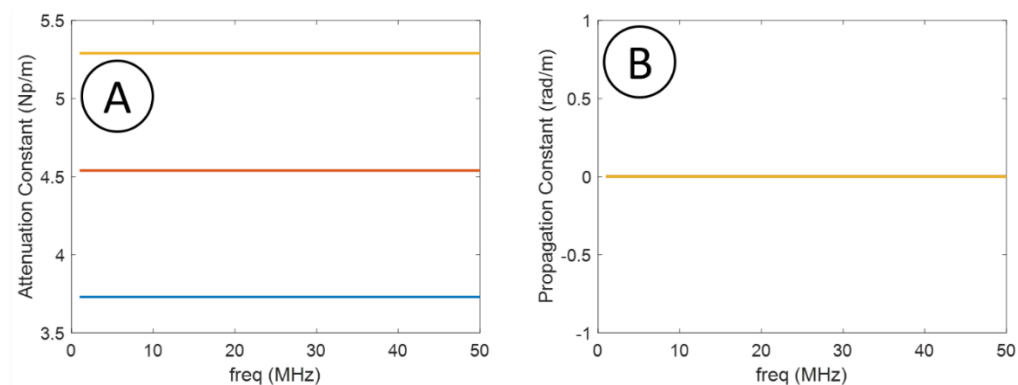


Figure 3.6: (a) Attenuation and (b) propagation constants as a function of frequency for a VMGTL without MTM for  $r = 4$  cm (blue),  $r = 5$  cm (orange) and  $r = 6$  cm (yellow)

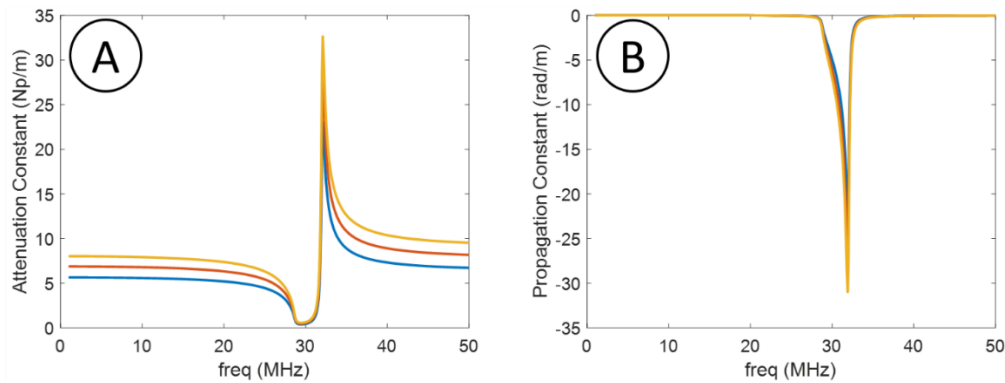


Figure 3.7: (a) Attenuation and (b) propagation constants as a function of frequency for VMGTL assisted by one MTM slab, for  $r = 4$  cm (blue),  $r = 5$  cm (orange) and  $r = 6$  cm (yellow)

So, the additional power transferred between the drivers is not coming from the enhancement of the coupling, but by propagating modes supported by the MTM. Travelling magnetic waves were already identified and employed in literature in different contexts [73], but they were never shown to be the cause of the “enhanced coupling” phenomenon. Nevertheless, this work clearly shows that the additional power being delivered to the receiver in the MTM gain region is not due to any stronger interaction of the evanescent modes but by the emergence of travelling ones.

Evanescent modes are characterized by  $\alpha > 0$  and  $\beta = 0$ . The greater  $\alpha$  becomes, faster the modes attenuate with distance, diminishing the probability that any coupling will occur between the drivers. If the gain mechanism was related with the enhancement of the evanescent modes,  $\alpha$  should be reduced. Still, as shown in Figure 3.7.(a), in the region of minimum  $\alpha$ , the gain is not maximum. On the contrary, it is negligible in comparison to the case where no MTM slab is employed. As shown in Figure 3.7.(b), the maximum gain occurs, in fact, at the frequency where the MTM maximizes both  $\alpha$  and  $\beta$  magnitudes. In this way, it can be said that the coupling is strongly reduced by MTMs (whose losses increases  $\alpha$ ) and that the observed transmission gain occurs primarily due to the appearance of propagating modes ( $\beta \neq 0$ ). Since the propagating modes transfer power more efficiently than the evanescent ones, MTM-added losses are fully compensated by the power of the magnetic waves, increasing the system’s net gain. Notice that, since  $\beta < 0$ , these waves are backwardly oriented.

Another important fact that becomes clear with VMGTL approach, although totally neglected on MTM-enhanced coupling theory, is that MTMs induce not only a region of high gain, but also a passband region with minimum attenuation. This

region lies in the sub-resonant region and has a relative flat response in comparison with the region of strong gain, around  $f_0$ . The flatness of this region imposes low distortion to signals, which could improve data transmission. Nonetheless, since MTM gain increases with  $\beta$ 's magnitude and since  $\beta$  decreases rapidly out of the operating frequency, the average power transfer in this sub-resonant region is significantly smaller than the peak gain. This means that MTMs, in principle, could be either used for maximizing data rate or power transfer, but optimum values for both cannot be simultaneously obtained. Optimum bandwidth-gain trade-off in SIPDT systems lies fundamentally in-between these two cases.

Finally, the MATLAB code used to obtain the results presented in this section were included in Annex C.

### 3.4

#### Parametric study of MTM-assisted VMGTL

##### 3.4.1

##### Channel sensitivity to $F$ and $Q$ parameters

Using the proposed analytical model, the channel sensitivity to the MTM's  $F$  and  $Q$  parameters can be evaluated. The obtained results are shown in Figures 3.8 to 3.10. Figure 3.8 presents the sensitivity of the VMGTL attenuation and propagation constants channel to  $F$ , for  $Q = 100$  and  $F$  varying from 0.2 to 0.8, in steps of 0.15. On the other hand, Figure 3.9 shows the sensitivity of VMGTL attenuation and propagation constants to  $Q$ , for  $F = 0.4$  and  $Q$  varying from 10 to 100, in steps of 22.5. Besides, Figure 3.10 highlights the sensitivity of VMGTL transfer function to  $F$  and  $Q$ .

These results indicate that the sensitivity of the channel to  $F$  is much stronger than to  $Q$ . Hence, while  $F$  can be employed to control the bandwidth of the passband region created by the MTM,  $Q$ -factor can be used to regulate the magnitude of the response.

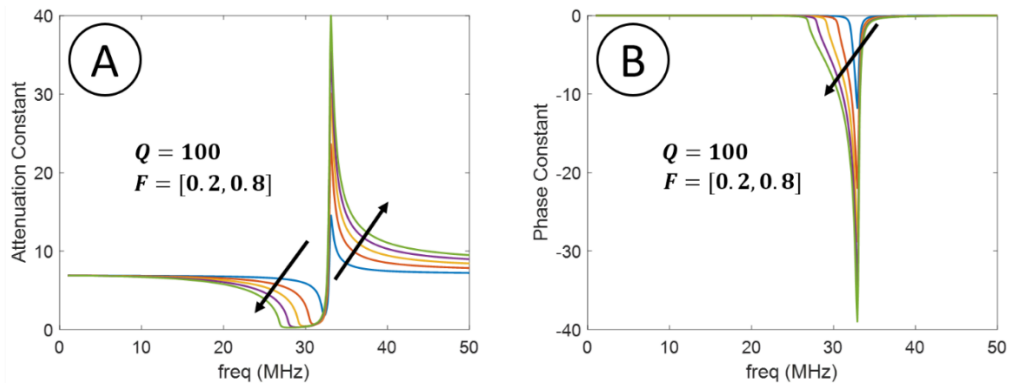


Figure 3.8: Sensitivity of VMGTL (a) attenuation and (b) propagation constants to  $F$

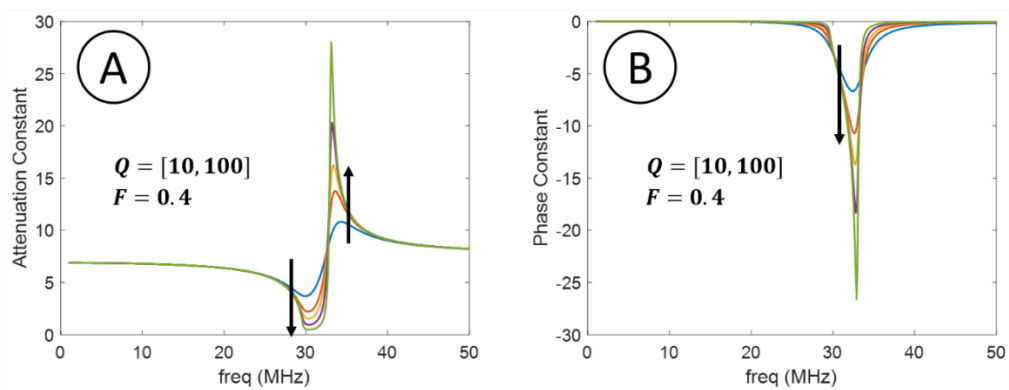


Figure 3.9: Sensitivity of VMGTL (a) attenuation and (b) propagation constants to  $Q$

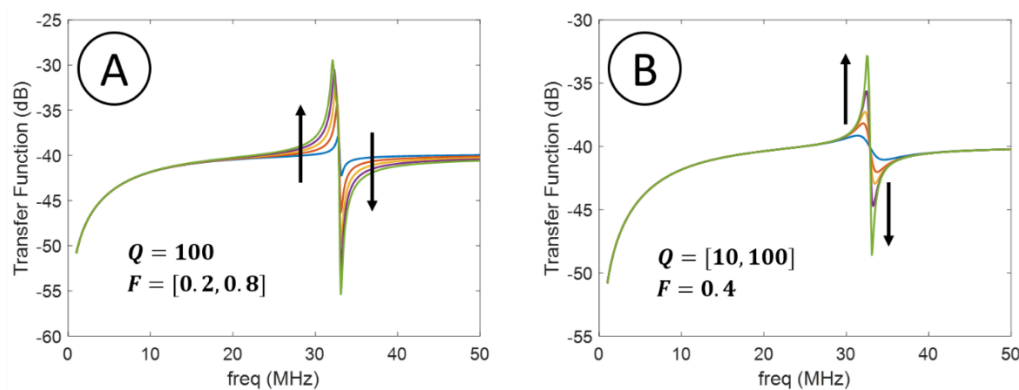


Figure 3.10: Sensitivity of VMGTL transfer function to (a)  $F$  and (b)  $Q$ . While  $F$  governs the bandwidth of the passband,  $Q$  regulates only the magnitude of the response

### 3.4.2

#### Number $N$ of MTM slabs

Concerning the number  $N$  of slabs, analytical calculations were performed varying the number of MTMs in the channel, from 1 to 10 slabs, assuming that  $D$  was constant and that the slabs were equally distant from each other by a factor  $D_2 = D/(1 + N)$ . Figure 3.11 shows how the channel bandwidth and gain vary with the number of slabs, when operating at two different regions: (a) minimum distortion and (b) high gain. On the other hand, Figure 3.12 shows how the VMGTL transfer function varies with the number of MTMs.

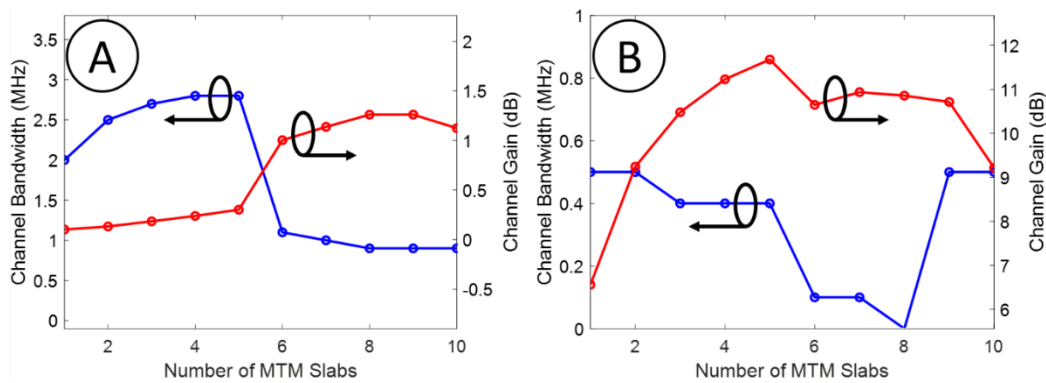


Figure 3.11: The bandwidth-gain trade-off when operating at the region of (a) minimum distortion and (b) high gain

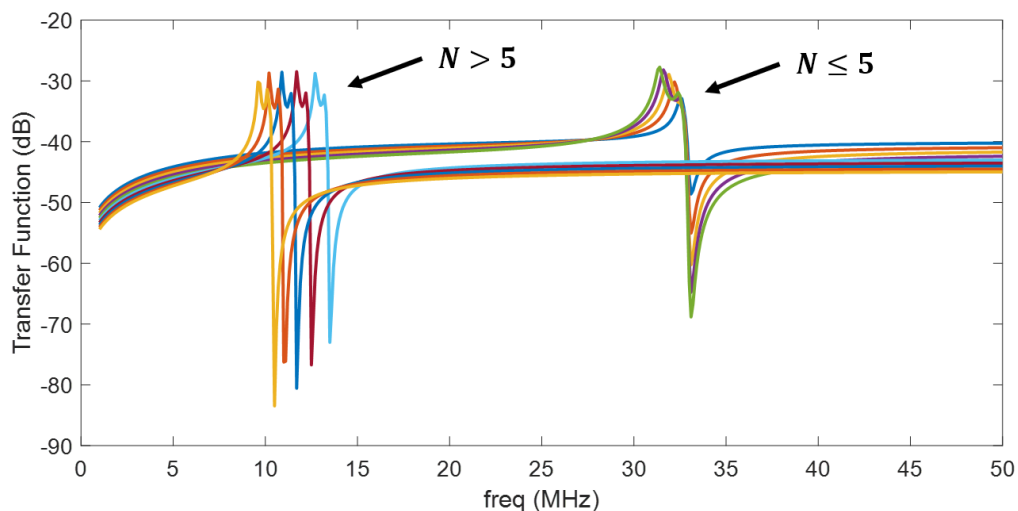


Figure 3.12: VMGTL transfer function with an increasing number  $N$  of MTM slabs

Figure 3.11 shows that the peak gain of the high-gain region (strong  $\beta$  response) and the minimum-distortion band (flat  $\alpha$  response) start to saturate as the number of MTM slabs increases. Besides, note that when  $D_2$  becomes small (equal or smaller than the lattice periodicity  $a$ ), due to the increasing number of MTMs inside of the inductive link, the mutual coupling between the slabs forces them to operate as one single structure, at a much lower  $f_0$ , as shown in Figure 3.12. When the MTMs get coupled with each other,  $f_0$  is decreased by a factor of  $\sqrt{N}$ .

As shown in Figure 3.11, the achievable bandwidth in the minimum-distortion region is much higher (almost one order of magnitude) than the one obtained in the high-gain region. However, the channel gain in the minimum-distortion region is almost negligible (less than 1.5 dB). Conversely, the high-gain region reaches power gains up to 12 dB, permitting to deliver much more power to the receiver, but at the cost of a very narrow bandwidth (less than 0.5 MHz). Notice that bandwidth is dramatically reduced in both scenarios when the mutual coupling between the MTMs force  $f_0$  to decrease, with one exception for  $N = [9,10]$  in Figure 3.11(b). In the high-gain region, when  $N$  is high, not only the MTM slabs get coupled but they also interact strongly via their mutual coupling. This strong interaction increases losses and power dissipation, degrading the Q-factor of the unit cells. That is why we see a reduction in gain and an increase in bandwidth for  $N = [9,10]$  in Figure 3.11(b).

### 3.4.3

#### Multiple MTMs set to different operating frequencies

Based on the results presented in the previous subsection, a new strategy to increase the capacity of the inductive channel keeping a net gain was proposed. It consists in using multiple MTM slabs set to different values of  $f_0$ . Figures 3.13 and 3.14 show the behavior of the attenuation and propagation constants as a function of the frequency, using three MTM slabs in the channel. For case 1, the resonance frequencies of the MTMs used to generate the response presented in Figure 3.13 were set to:  $f_{01} = 10 \text{ MHz}$ ,  $f_{02} = 32 \text{ MHz}$  and  $f_{03} = 40 \text{ MHz}$ . On the other hand, for the case 2, shown in Figure 3.14, the resonance frequencies were set to:  $f_{01} = 10 \text{ MHz}$ ,  $f_{02} = 31 \text{ MHz}$  and  $f_{03} = 32 \text{ MHz}$ . Besides, Figure 3.15 shows the response of the VMGTL transfer function with 3 MTM slabs, for case 1 (Figure 3.15.(a)) and case 2 (Figure 3.15.(b)).

As shown in Figures 3.13 and 3.15.(a), this new approach permits to create a population of narrow passband regions inside the inductive channel. However, it meets its limitation if the MTMs are resonating in immediately adjacent bands since the high gain region of the slabs (around maximum  $|\beta|$ ) is always followed by an extremely low one, due to the anti-resonance phenomenon. In such cases, as exemplified in Figures 3.14 and 3.15.(b), the peak of the MTMs may “fall” into a valley produced by its neighbor, compromising the efficacy of this methodology.

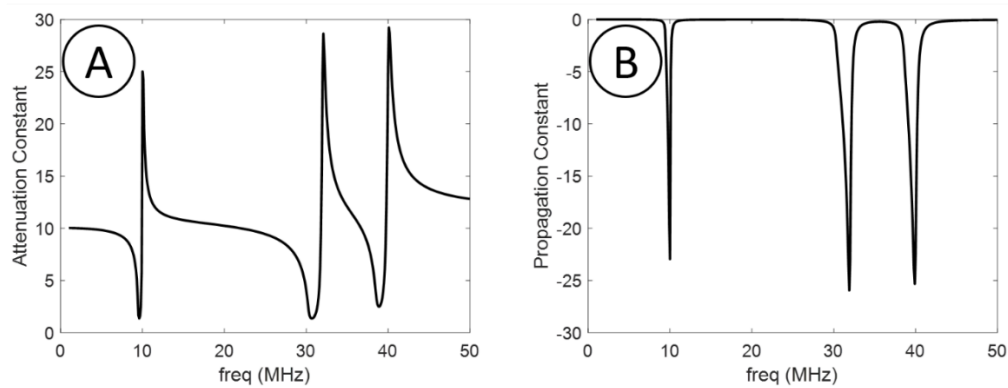


Figure 3.13: (a) Attenuation and (b) propagation constants with three MTM slabs, for case 1:  $f_{01} = 10 \text{ MHz}$ ,  $f_{02} = 32 \text{ MHz}$  and  $f_{03} = 40 \text{ MHz}$

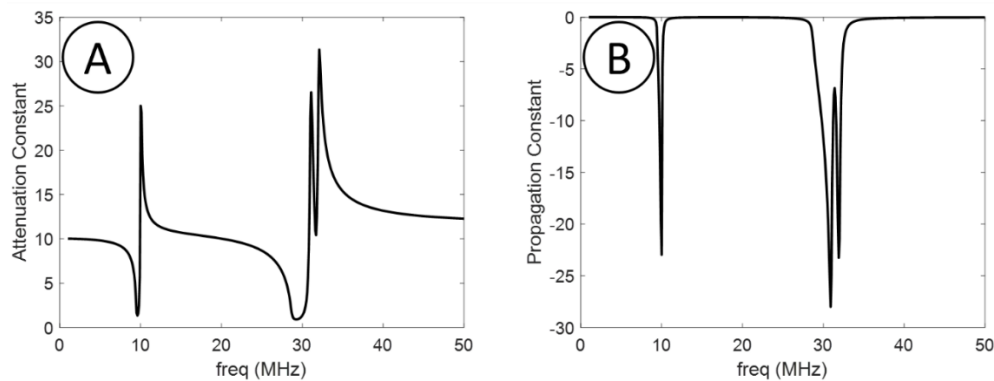


Figure 3.14: (a) Attenuation and (b) propagation constants with three MTM slabs, for case 2:  $f_{01} = 10 \text{ MHz}$ ,  $f_{02} = 31 \text{ MHz}$  and  $f_{03} = 32 \text{ MHz}$

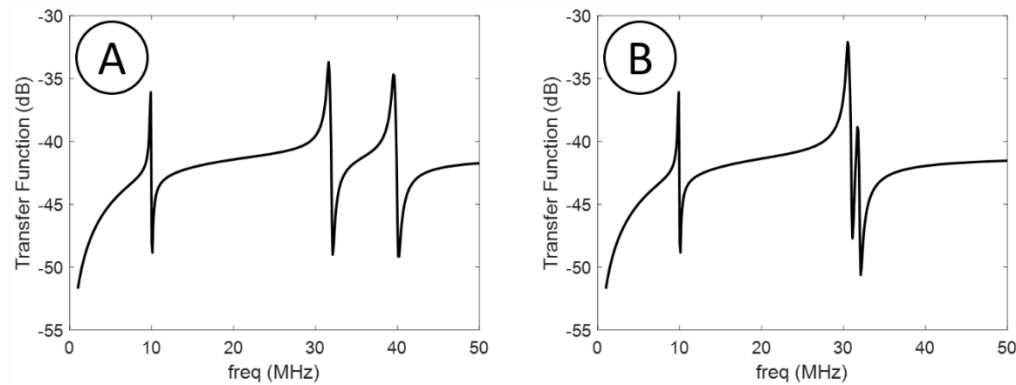


Figure 3.15: Results for the VMGTL transfer function with 3 MTM slabs for (a) case 1 and (b) case 2

### 3.5

#### VMGTL in lossy media

##### 3.5.1

##### Effects of lossy dielectric media

In the previous sections of this chapter, TX and RX coils were assumed to be perfect inductors, with no parasitic capacitance. Consequently, after a certain saturation frequency  $f_{sat}$ , the channel transfer function  $S_{21}$  keeps constant and does not vary with frequency. Evidently, it is not the case for real inductors, even if assuming the hypothesis of being far from the self-resonance of the coils, since just after saturation  $S_{21}$  will decrease monotonically with frequency, due to the increasing of the capacitive interaction between the drivers. Figure 3.16 highlights these regions in the transfer function of the inductive link studied in section 3.3, obtained from ADS simulations, for different coil radius.

To incorporate this magneto-capacitive coupling effect to the model, aiming to improve the correspondence between the analytical model and the numerical simulations (or experimental measurements) in the VMGTL approach, one just needs to set an appropriate value for  $G'_e$ , as shown in Figure 3.17. This means that, from the point of view of the VMGTL approach, the parasitic capacitances of the drivers are analogous to dielectric losses.

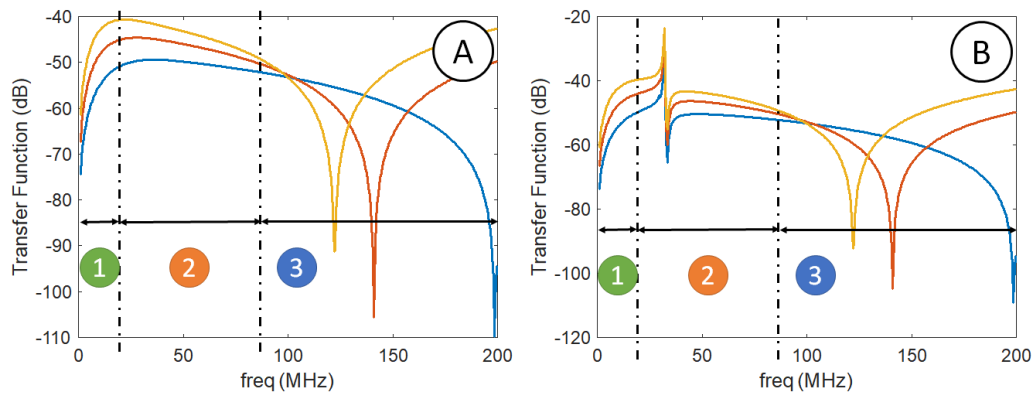


Figure 3.16: ADS-simulated IPT transfer function (a) without and (b) with a MTM is characterized by three major regions: 1) purely inductive 2) magneto-capacitive and 3) self-resonant, for  $r = 4 \text{ cm}$  (blue),  $r = 5 \text{ cm}$  (orange) and  $r = 6 \text{ cm}$  (yellow)

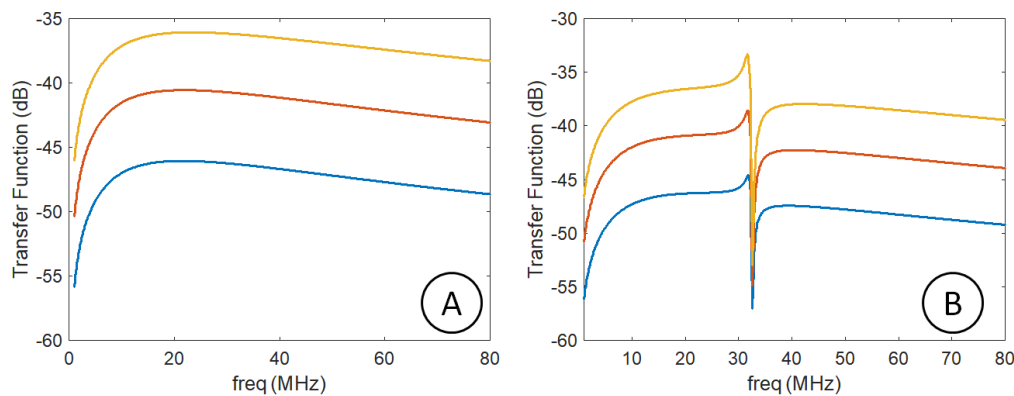


Figure 3.17: Estimation of the transfer function using VMGTL with  $G'_e = 4 \cdot 10^5$  (a) without and (b) with one MTM slab, for  $r = 4 \text{ cm}$  (blue),  $r = 5 \text{ cm}$  (orange) and  $r = 6 \text{ cm}$  (yellow)

In particular, adding  $G'_e = 4 \cdot 10^5 \text{ S/m}$  to the inductive link studied in section 3.3, the analytical behavior of the inductive link for frequencies above  $f_{sat}$  become much closer to the one obtained on ADS, as can be observed by comparing the simulated and analytical results of the IPT transfer function, shown in Figure 3.16 and 3.17, respectively. This is an interesting result, especially because it helps to elucidate one well-known phenomenon on MTM-based lenses: the degradation of the MTM gain, when operating out of the purely inductive region.

Figure 3.18 shows the analytical estimation of the attenuation constant of the VMGTL, with  $G'_e = 4 \cdot 10^5 \text{ S/m}$ , without (Figure 3.18.(a)) and with (Figure 3.18.(b)) one MTM slab, as a function of frequency, for different coil radius. On the other hand, Figure 3.19 shows the analytical estimation of the propagation constant of

the VMGTL, for  $G'_e = 4 \cdot 10^5 S/m$ , without (Figure 3.19.(a)) and with (Figure 3.19.(b)) one MTM slab, as a function of frequency, for different coil radius.

As shown in Figure 3.18 and 3.19, if  $G'_e > 0$ , the attenuation constant  $\alpha$  becomes a function of the frequency and the propagation constant  $\beta$  acquires a non-null, positive value. In the presence of a MTM,  $\beta$  still becomes negative, but since it starts from an initial value above zero, the resultant negative response is smaller in magnitude, as shown in Figure 3.19.(b). This reduction in the maximum attainable magnitude of  $\beta < 0$  limits the maximum attainable MTM gain, explaining why the gain of the MTM is always smaller in the magneto-capacitive region in comparison with the inductive region.

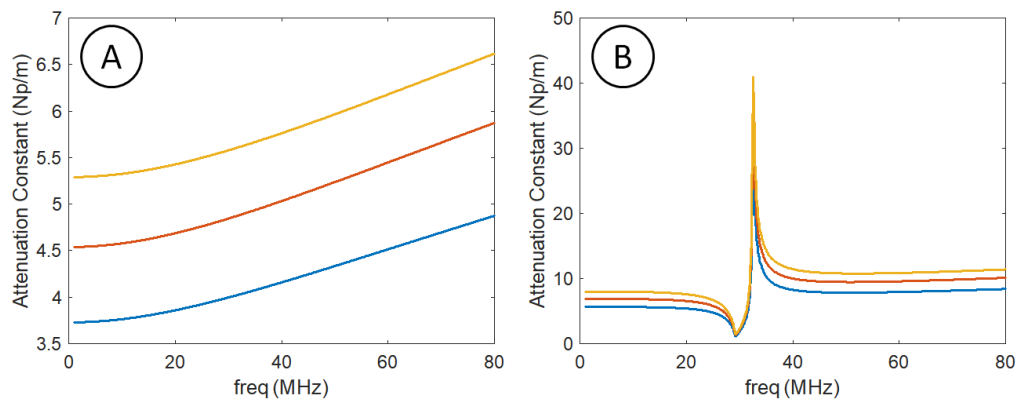


Figure 3.18: Attenuation constant for the VMGTL with  $G'_e = 4 \cdot 10^5$  (a) without and (b) with one MTM slab as a function of frequency, for  $r = 4$  cm (blue),  $r = 5$  cm (orange) and  $r = 6$  cm (yellow)

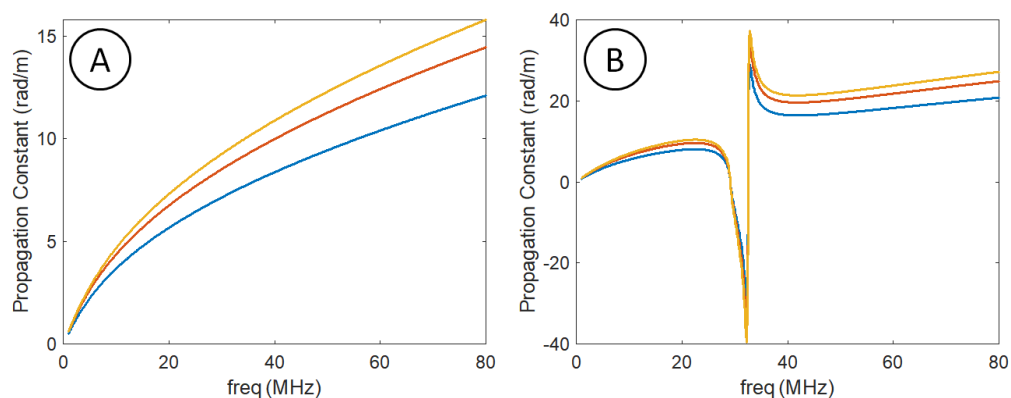


Figure 3.19: Propagation constant for the VMGTL with  $G'_e = 4 \cdot 10^5$  (a) without and (b) with one MTM slab as a function of frequency, for  $r = 4$  cm (blue),  $r = 5$  cm (orange) and  $r = 6$  cm (yellow)

Besides the gain compression, another consequence of  $G'_e > 0$  is the huge reduction of the minimum-distortion band, as shown in Figure 3.18.(b). It implicates that, for any practical purpose, only low-loss coils with exceptionally low parasitics could be used to implement it.

Figure 3.20 shows the MTM gain curve as a function of  $G'_e$ , derived from the VMGTL equations, assuming an inductive system with  $r = 5 \text{ cm}$  assisted by one MTM slab, with a maximum gain of  $6.7 \text{ dB}$ . Note that for  $G'_e \geq 10^7 \text{ S/m}$  the MTM gain become negligible.

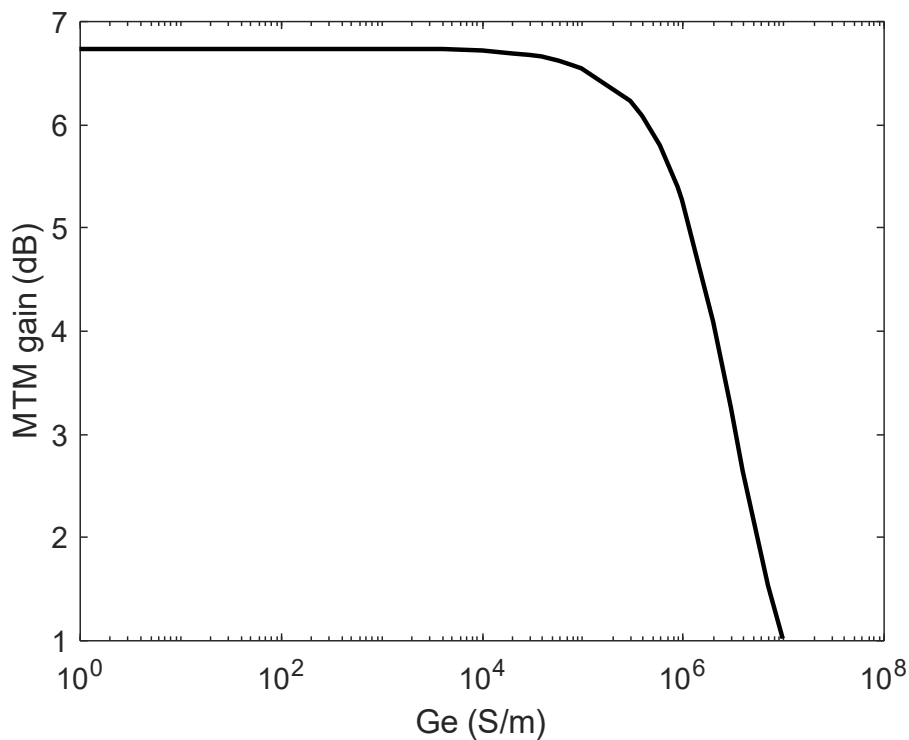


Figure 3.20: MTM gain as a function of  $G'_e$

### 3.5.2

#### Effects of lossy magnetic media

Most materials do not have a magnetic response, therefore the distributed magnetic conductance  $G'_m = 0$  in most cases. One exception would be a VMGTL surrounded by a lossy ferromagnetic material. Since VMGTL are magnetic-driven, the MTM gain decreases with  $G'_m$  faster than with  $G'_e$ , as shown in Figure 3.21.

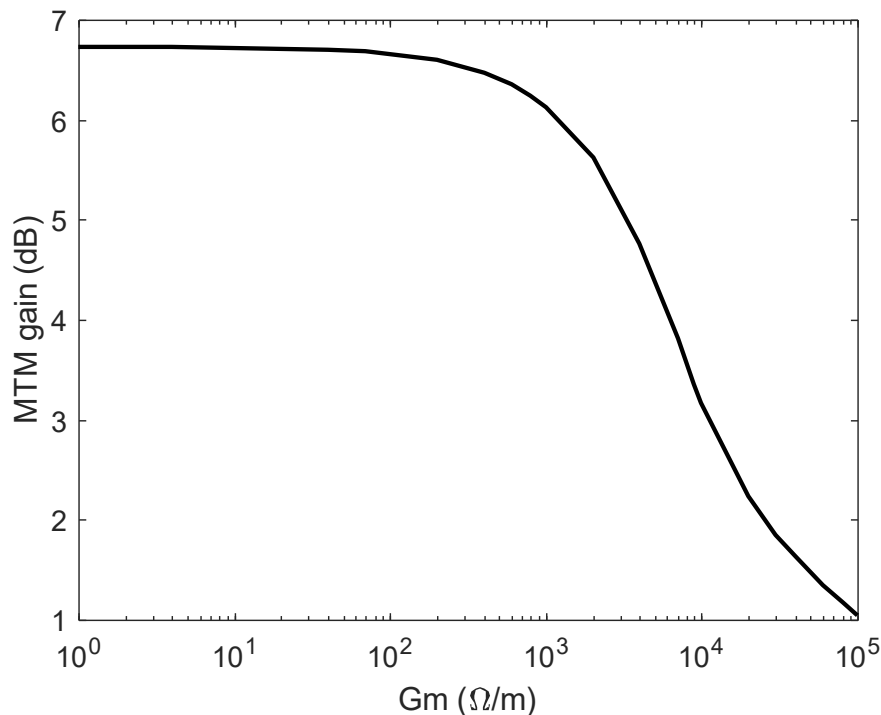


Figure 3.21: MTM gain as a function of  $G'_m$

### 3.5.3

#### Estimation of seawater $G'_e$

Considering that the main target of this work is the implementation of an efficient UWSN in seawater, the proposed VMGTL formalism, employing its equivalent electrical conductance  $G'_e$  and magnetic conductance  $G'_m$ , should be able to describe accurately the medium losses of underwater inductive links.

In the case of saltwater, since it is characterized by a magnetic behavior similar to the air ( $Re\{\mu\} \approx \mu_0, Im\{\mu\} = 0$ ) and an electric behavior 80 times greater than the air, with dielectric losses ( $Re\{\varepsilon\} \approx 80\varepsilon_0, Im\{\varepsilon\} \neq 0$ ), the equivalent VMGTL loss parameters are given by:

$$G'_m = 0 \quad (44)$$

$$G'_e = f(\omega, \text{salinity}) \quad (45)$$

As shown in Figure 3.22, the salinity level along Brazilian coast is extremely high, reaching 37000 ppm or 37 g/L. In [74], different models for the variation of  $Im\{\varepsilon\}$ , as a function of frequency and salinity are presented and validated by experimental data. However, the study only investigates the behavior of the seawater's dielectric constant for frequencies above 280 MHz. Since their model clearly demonstrate that it follows a decaying exponential behavior with frequency, an extrapolation can be made for lower frequencies by means of an exponential regression, like in Figure 3.23.

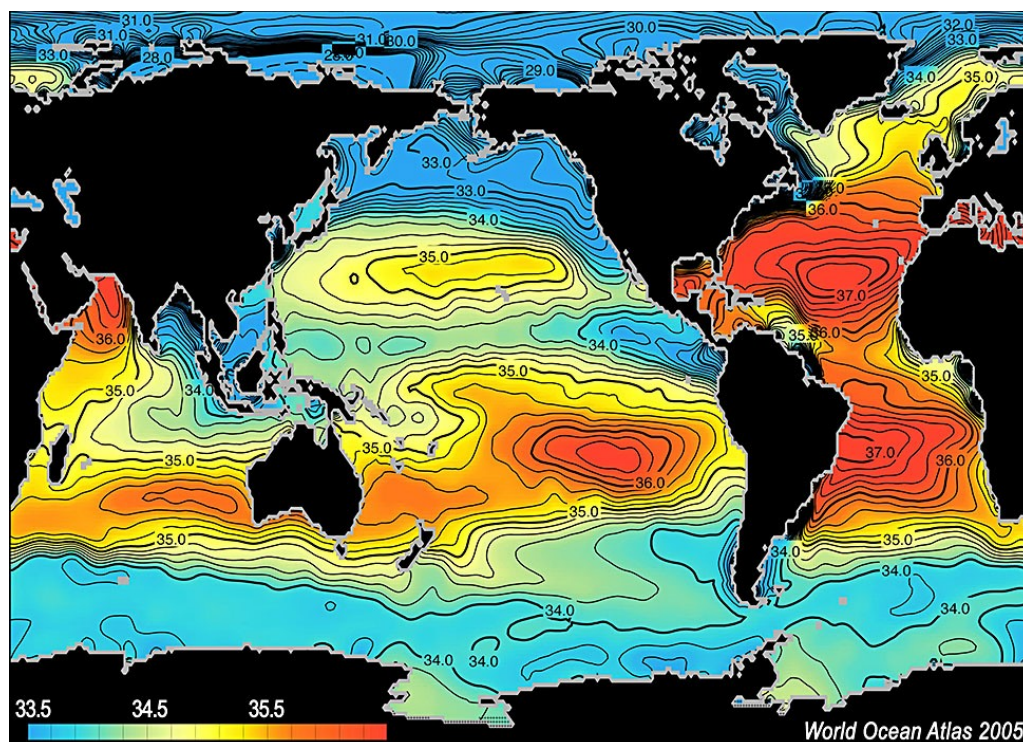


Figure 3.22: Distribution of the ocean's salinity

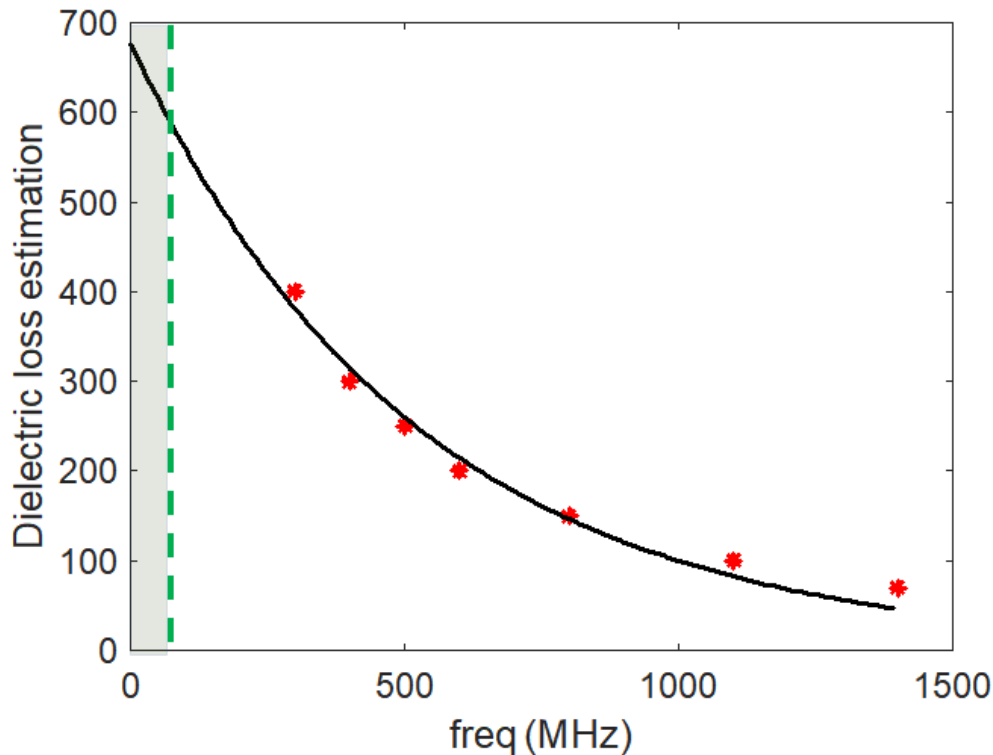


Figure 3.23: Dielectric loss in seawater: exponential regression estimation (black curve) and data extracted from [74] (red dots). The frequencies of interest for UWPT lies on the left region of the dashed green line

Based on the exponential regression results, it can be estimated that in the region of interest (below 100 MHz), the dielectric losses of seawater vary inside the range of  $Im\{\epsilon_r\} = [580, 680]$ . So, assuming the worst-case scenario, Brazilian seawater losses can be rounded to  $Im\{\epsilon_r\} = 700$  for a confined VMGTL. Nonetheless, notice that the seawater dielectric loss is also a function of the temperature  $T$ . The values presented in this section assume  $T = [23^\circ C, 26^\circ C]$ . As  $T$  decreases, dielectric losses tend to be higher. However, the assumed temperature range is a good approximation, considering most UWSNs operate in depths lower than 100 m, where the average  $T$  of the water is almost the same as in the surface, as shown in Figure 3.24.

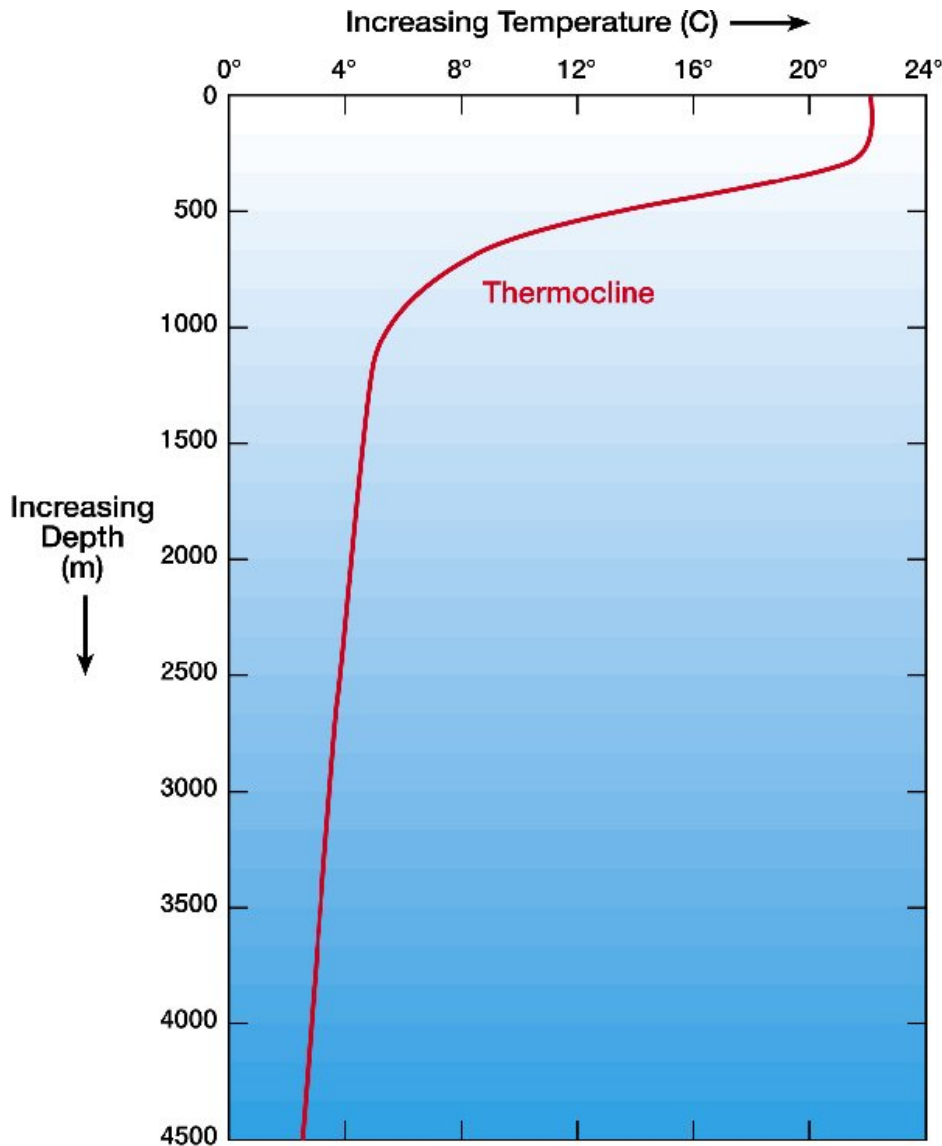


Figure 3.24: Ocean water temperature as a function of depth [75]

Nonetheless, due to the low values of  $\kappa_m$  and since saltwater will also interact with the MTM itself, the apparent  $Im\{\varepsilon\}$  of the lossy VMGTL is much higher. An estimation of the appropriated  $G'_e$  can be obtained by comparing the analytical prediction of the gain compression, shown in section 3.5.1, with the gain compression observed via numerical simulation of the underwater WPT system. For the numerical simulation on ADS, it was assumed that the medium has an electric conductivity of  $5 S/m$ , which is the average conductivity of seawater in depths smaller than  $500 m$  [76].

Figure 3.25 shows the obtained simulated results for the power gain in air, freshwater and seawater for one MTM-assisted WPT system using coils with  $r = 5 cm$ . As it can be seen in Figure 3.25, at the operating frequency, the MTM

presents a gain of  $7.3 \text{ dB}$  in air and freshwater, but only of  $5 \text{ dB}$  in seawater due to the appearance of eddy currents.

Since the simulated results indicate that the MTM gain is reduced in approximately  $2 \text{ dB}$ , it can be estimated from the results presented in Figure 3.25 that the equivalent  $G'_e$  for unconfined VMGTL in seawater is  $G'_e = 1.5 \cdot 10^6 \text{ S/m}$ . Notice that this value is non-physical, since it incorporates the coupling between the TX and RX coils and the virtual coils formed by the eddy currents, as shown in Figure 3.26. The unconfined value of  $G'_e$  only has meaning in the context of the VMGTL analogy.

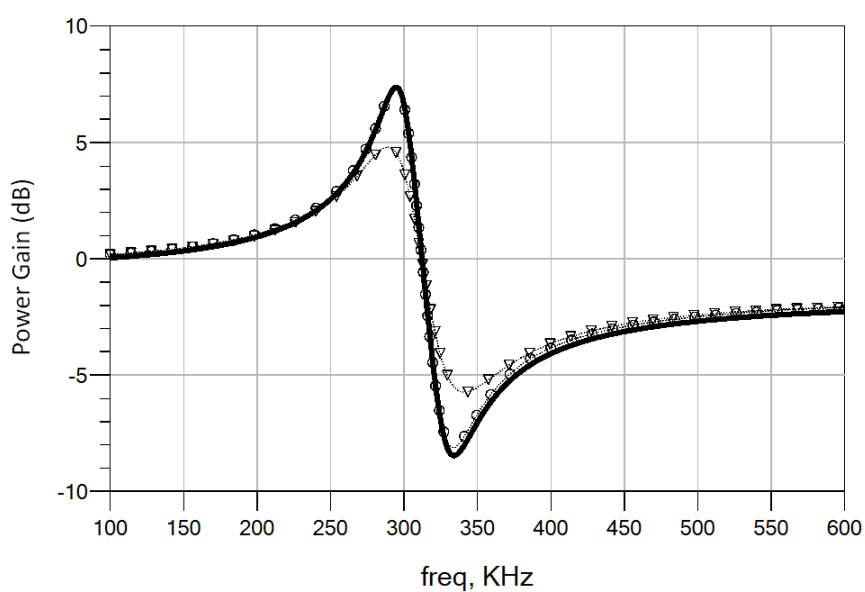


Figure 3.25: Simulated results for the MTM gain in air (solid line), freshwater (circle) and seawater (triangle) for a MTM-assisted WPT system using coils with  $r = 5 \text{ cm}$

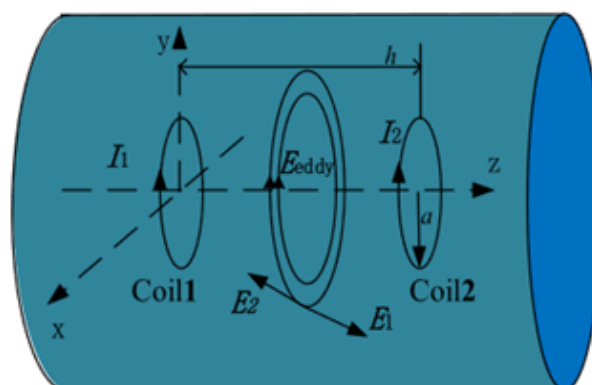


Figure 3.26: Representation of the interaction of the eddy currents. These eddy currents behave as virtual coils inside the inductive link

### 3.6

#### Final considerations

In this chapter, a parametric study of MTM-assisted inductive channels was presented. The channel modeling employed the proposed VMGTL approach in order to clarify the MTM mechanism of power enhancement. Based on VMGTL model, MTMs are shown to improve the power transmission between the drivers around the resonance not by means of enhanced coupling, as previously reported, but by backward propagating modes. The MTM response were shown to depend on  $Q$  and  $F$  parameters, which regulate the magnitude and bandwidth of the response, respectively. Similarly, it was shown that using more than one MTM slab to assist the inductive link helps to increase both gain and bandwidth, but this effect saturates when the number  $N$  of MTMs increase to the extent that the separation distance between the slabs  $D_2 \leq a$ . In this case, all MTMs inside the inductive link get coupled and start to behave as one single lens, operating at a frequency  $f_0/\sqrt{N}$ .

Besides that, the same approach was able to reveal, for the first time, that IPTs assisted by MTM lenses present two regions of interest: 1) the well-known high-gain region around the MTM operating frequency  $f_0$ , which is characterized by  $\beta < 0$  and is due to the emergence of travelling magnetic waves, and not to an enhanced  $\kappa_m$ , and 2) the minimum-distortion sub-resonance region, which is characterized by low  $\alpha$ . The latter, however, has just a slight power gain in comparison with the inductive channel assisted by no MTM, implying that MTM-assisted SIPDT must either maximize power transfer or data rate. In any case, both regions saturate in terms of bandwidth and gain with the increasing of  $N$ .

Considering losses, the minimum-distortion region bandwidth is shown to be quite sensible to  $G_e'$ , which means it is implementable only in extremely low-loss systems (low-loss TX and RX coils and low-loss surrounding media). Moreover,  $G_e'$  and  $G_m'$  are shown to degrade the maximum achievable MTM gain due to the emerging of forward propagating modes, represented by  $\beta > 0$ , which limits the maximum negative magnitude of  $\beta$  around the MTM operating frequency. One important consideration on the VMGTL modelling aspects is that the correspondence between VMGTL models, numerical simulations and experimental measurements are shown to increase assuming  $G_e' \neq 0$ , since the linear decay of the IPT transfer function observed at frequencies over the magneto-capacitive region, which is caused by the capacitive coupling between TX and RX coils, can be accurately described as dielectric losses. In addition,  $G_e'$

was shown to be a nonphysical parameter ( $G_e' \gg \sigma$ ). A strategy based on the expected compression of the MTM gain was presented aiming to estimate its corresponding value in seawater and other lossy medium in the context of VMGTL theory.

Finally, this chapter highlights the fact that, due to the anti-resonant, high attenuation region that follows the MTM gain region, two MTM slabs set to different  $f_0$  cannot operate at bandwidths too close to each other.

## 4

### MTM design for underwater SIPDT applications

#### 4.1

##### Design of MTM lenses

##### 4.1.1

##### Double-sided spiral resonator unit-cell

SRRs or SRs are used as cells for the synthesis of MNG MTM capable of magnetic near field focusing. However, SR-based unit cells have the advantage of presenting a Q-factor almost three times higher than an equivalent SRR with same outer dimensions [77]. Since the MTM gain is directly proportional to the Q-factor of its unit cells, SR will present a better focalization capability than SRR. Also, since SR is equivalent to a RLC series circuit, it will be directly proportional to  $\sqrt{L_{cell}}$ , which can be enhanced by the increasing of the length of the SR conductor path.

Nonetheless, since the operating frequency for UWSN is low (few MHz at most), the necessary inductance and/or capacitance of the unit cell should be remarkably high, implicating in prohibitively large dimensions of the cell (reaching in the order of meters). To reduce the cell size, it was adopted two basic strategies:

1. To double the inductance of the cell  $L_{cell}$  by designing a **double-sided spiral resonator (DSSR)** connected through a metallic via (see Figure 4.1). Notice that the proposed spiral maintains the same electric current orientation on both sides of the cell. Otherwise, the storage magnetic field in the up and the bottom faces would cancel each other, resulting in zero gain. Also, notice that, being the DSSR inductance twice higher than the SR one, its Q-factor will be about 41% higher, according to (13);
2. To insert a surface-mount device (SMD) capacitor ( $C_{SMD}$ ) in series with the DSSR circuitry, which will be called “coarse tuning element”, since it will be used to impose large frequency shifts to the MTM slab.

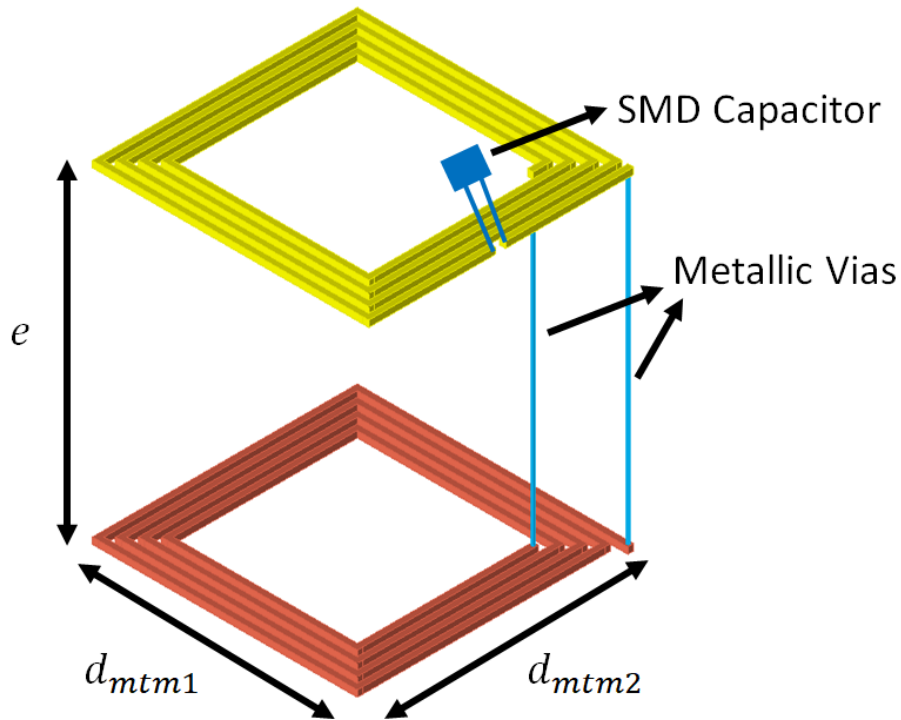


Figure 4.1: Proposed MTM DSSR unit cell with copper surfaces highlighted in yellow and red. The substrate with thickness  $e$  was kept transparent to highlight the metallic vias

The MTM gain is defined as:

$$Gain = \frac{S_{21_{MTM}}}{S_{21}} \quad (46)$$

where  $S_{21_{MTM}}$  and  $S_{21}$  are the transmission gain in the magnetic link with and without the MTM slab or cell, respectively.

In this chapter, it was considered a DSSR conceived on FR4 and copper ( $\epsilon_r = 4.4$ ,  $\tan \delta = 0.018$ ) with the following characteristics:

- **Outer dimensions:**  $d_{mtm1} = d_{mtm2} = 24 \text{ mm}$
- **Substrate thickness:**  $e = 1 \text{ mm}$
- **Coarse tuning element:**  $C_{SMD} = 0.15 \mu F$
- **Conductor width:**  $w = 1 \text{ mm}$
- **Gap:**  $g = 1 \text{ mm}$
- **Diameter of the electric via:**  $d_{via} = 0.5 \text{ mm}$
- **Number of turns:**  $N_{turns} = 4$

One important remark should be made concerning the frequency range considered for the numerical simulations in this chapter: most of the simulations were done in the range of hundred  $MHz$ , although the intended frequency range for underwater applications is much lower. Based on the metamaterial theory presented in section 2.1, MTMs should not change their main characteristics by varying the coarse tuning element  $C_{SMD}$  in frequency bands where the behavior of the EM fields is similar (i.e., throughout the RF band). Based on that fact, when simulating large arrays and the fields behavior,  $C_{SMD}$  was chosen in order to maintain the operating frequency in the range of ten up to hundred  $MHz$ . In this way, the size of the simulation on Computer Simulation Technology (CST) Studio Suite and ADS is much smaller. Note that the volume of the simulation space is proportional to  $\lambda^3$ , which is quite big in the ten or hundred kHz ranges. Nonetheless, since below 1  $GHz$  the behavior of structures with a scale of tens of millimeters are similar electromagnetically speaking (unit-cell dimensions are big regarding to  $\lambda$ ), we can expect that the behavior of the MTM seen in the hundred  $MHz$  range will be very similar to the one obtained in the hundred  $kHz$  one, if the losses introduced by  $C_{SMD}$  are negligible (the main drawback of  $C_{SMD}$  to the unit-cell performance is to degrade its  $Q$ ).

#### 4.1.2

##### **DSSR equivalent material properties**

Figure 4.2 shows a single-cell MTM inserted between the drivers of the magnetic link, aiming to use it as a lens. The considered IPT system used square coils with outer dimensions  $L_{out} = 40\text{ mm}$  and  $D = 20\text{ mm}$ . In this example, the width of the conductors  $w$  and the gap between the conductors  $g$  of the considered DSSR unit-cell were assumed to be  $1\text{ mm}$ . Figure 4.3 shows the equivalent  $\mu_r$  of the cell and the obtained gain, when it is employed as a lens in a 2-coil IPT system.

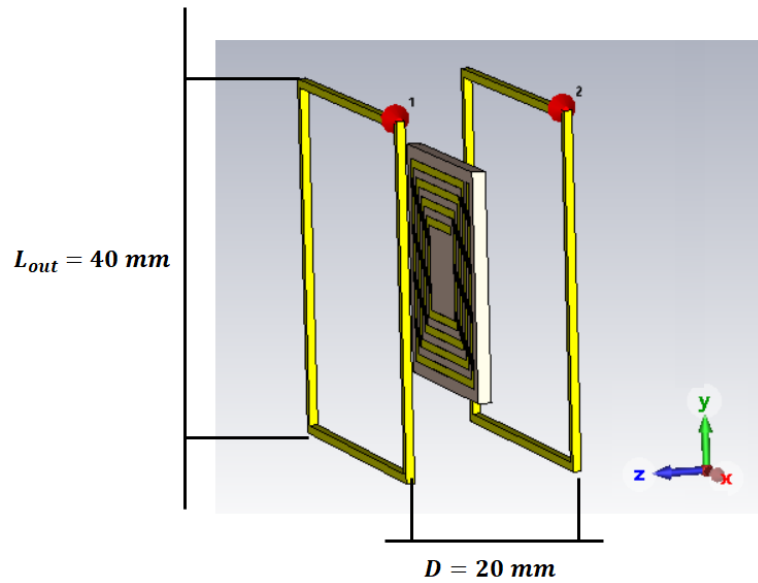


Figure 4.2: Proposed DSSR unit-cell employed as a lens

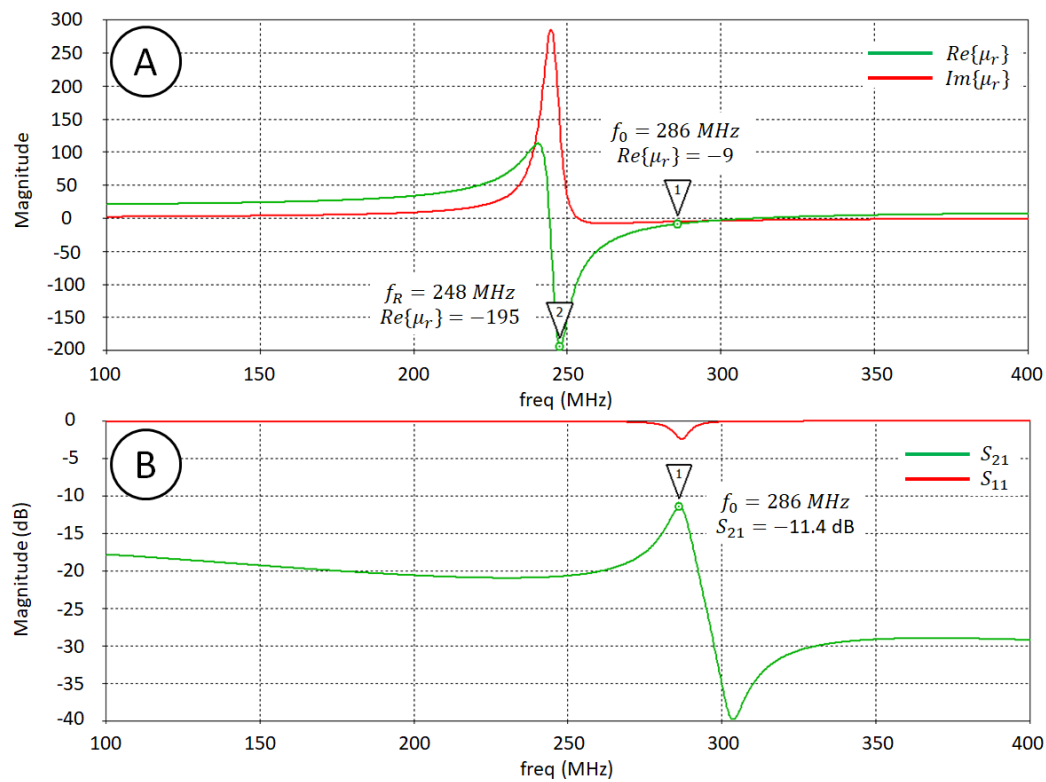


Figure 4.3: Equivalent (a)  $\mu_r$  and (b) gain of the proposed unit-cell, when it is employed as a lens in a IPT system. Notice that the gain occurs out of the resonance of the cell

One important aspect of the MNG MTMs' design and quite often confused in literature is the fact that the *resonance frequency*  $f_R$  of the unit-cell and the *operating frequency* (or *gain resonance*)  $f_0$  of the MTM are different frequencies. As it can be seen in Figure 4.3.(a), at the very resonance of the unit-cell  $f_R = 247 \text{ MHz}$ ,  $Re\{\mu_r\} \approx 0$  and  $Im\{\mu_r\} = 280$ , being extremely lossy. So, no gain can be perceived in the IPT transfer function. On the other hand, for frequencies slightly above  $f_R$ ,  $Re\{\mu_r\}$  is extremely negative ( $Re\{\mu_r\} \approx -200$ ), but MTM gain is near-zero because  $Im\{\mu_r\}$  is still considerably high ( $Im\{\mu_r\} \approx 100$ ).

Gain only starts to increase when  $Re\{\mu_r\} < 0$  and  $Im\{\mu_r\} \rightarrow 0$  around the MTM operating frequency  $f_0 = 286 \text{ MHz}$ . This means that not only the cell must behave as a MNG slab, but also must be low loss in order to let the MTM to realize a net gain, when assisting coupled coils. This is an important consideration on the design of these structures that most designers ignore or do not mention.

### 4.1.3

#### Fine tuning of the unit cell

Although coarse tuning of the unit-cell response can be controlled by means of lumped elements, the fine adjustment of the MTM equivalent  $\mu_r$  and  $\varepsilon_r$  must be made by means of geometric optimization of the cells. More specifically, considering the proposed DSSRs, this adjustment can be made by varying the gap and width of the unit-cell conductors, while keeping their summation constant:

$$w + g = \text{constant} \quad (47)$$

As shown in Figure 4.4, if their summation is constant and  $N_{turns}$  is fixed, the outer dimensions of the unit-cell will not vary with the increase of  $w$ , so the overall behavior of the MTM will be the same with a small shift in the frequency response. Notice that the amplitudes of the  $Re\{\mu_r\}$  and  $Im\{\mu_r\}$  do not vary a lot in frequency-shift range of more than  $100 \text{ MHz}$ . In this section, the summation constant was set at  $2 \text{ mm}$ , with  $N_{turns} = 4$ , which means that the outer dimensions of the cell will be  $24 \text{ mm}$ . Figures 4.5 and 4.6 show  $Re\{\mu_r\}$  and  $Im\{\mu_r\}$ , respectively, considering a DSSR with gaps ranging from  $0.2 \text{ mm}$  to  $1.8 \text{ mm}$ , in steps of  $0.2 \text{ mm}$ .

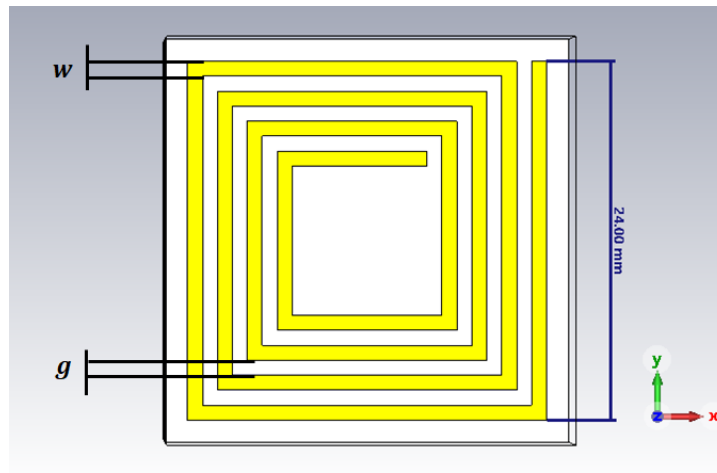


Figure 4.4: Geometric optimization of the unit-cell for fine tuning

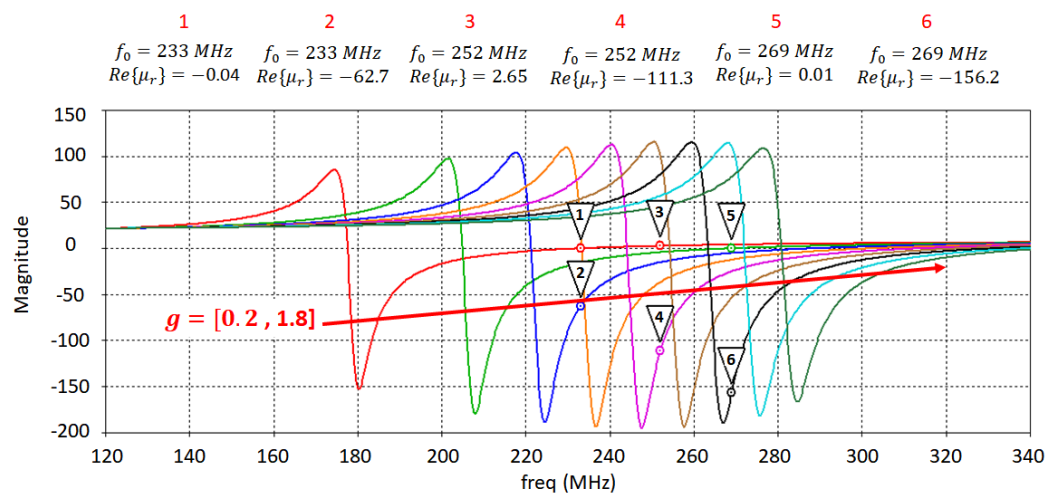


Figure 4.5: Equivalent  $Re\{\mu_r\}$  of the DSSR unit cell, for gap  $g = [0.2, 1.8]$ , in steps of 0.2

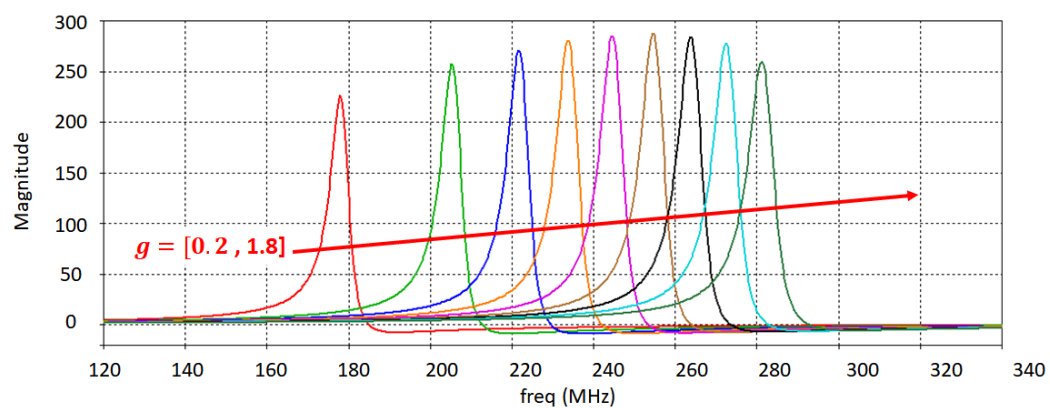


Figure 4.6: Equivalent  $Im\{\mu_r\}$  of the DSSR unit cell, for gap  $g = [0.2, 1.8]$ , in steps of 0.2

An important remark about the curves presented in Figures 4.5 and 4.6 is that the equivalent  $\mu_r$  of MTM cells, when put together in a lattice, suffers a deviation in their resonance and operating frequencies, due to the mutual coupling with their neighbors, which increases their apparent inductance and capacitance. This frequency shift depends on the lattice constant (the separation distance between the cells) and the gap  $g$ . When they are quite close to each other, the frequency shift could achieve a fractional bandwidth of 15% to 30%. Cells with low  $g$  and high  $w$  suffers higher frequency shifts since the magnitude of the mutual coupling is higher.

#### 4.1.4

#### Hybrid MTMs

The hybrid MTM lenses were firstly introduced in [78], as a mean to maximize the MTM gain. As shown in Figure 4.7, authors proposed a non-uniform distribution of the equivalent  $\mu_r$  of the unit cells, with  $\mu_r = 0$  at the MTM central region and  $\mu_r < 0$  at the MTM borders. In this way, authors could improve their MTM gain in about 3 dB. In this section, it is presented an extended discussion on the subject.

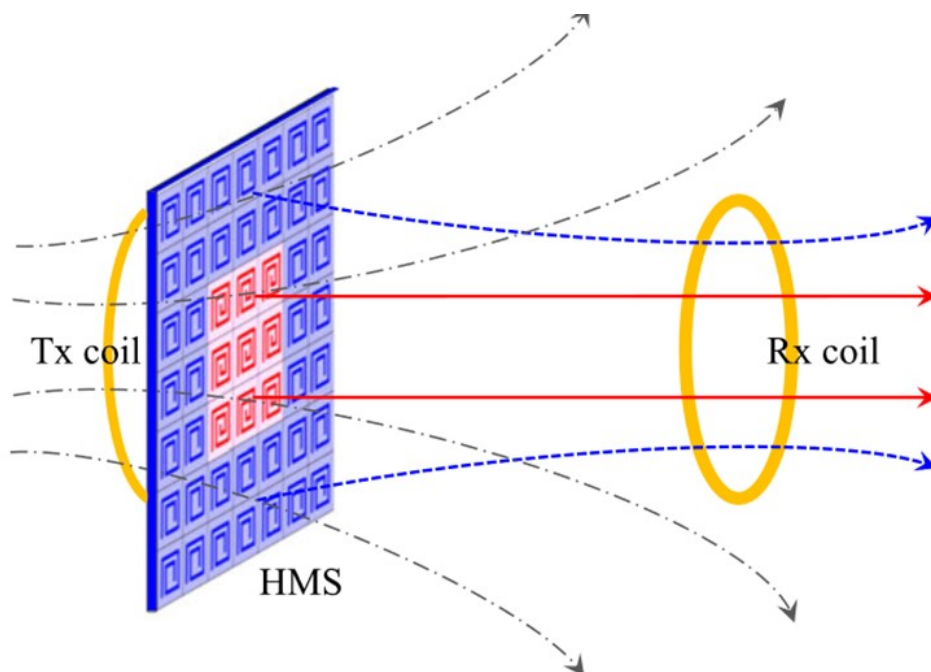


Figure 4.7: Enhanced focusing due to non-uniform central and border regions [78]

Based on the results obtained in section 4.1.3 (Figures 4.5 and 4.6), it is possible to adjust the geometric parameters of the unit cell to vary the magnitude of  $\mu_r$  and then create a hybrid MTM with a nonuniform distribution of  $\mu_r$ , keeping the cells with equal outer dimensions, which makes easier to arrange them together in the same lattice (with equal lattice constant).

Numerical simulations were performed on CST using frequency-domain finite element method, aiming to investigate the behavior of MTMs composed of 7x7 cells. The analyzed MTMs are subdivided in two regions only: 1) a central region consisting of 9 cells and 2) a border region consisting of 40 cells. The geometric parameters of the cells are chosen in a way that  $g + w = 2 \text{ mm}$ . The considered prototypes are presented in Figures 4.8 to 4.10.

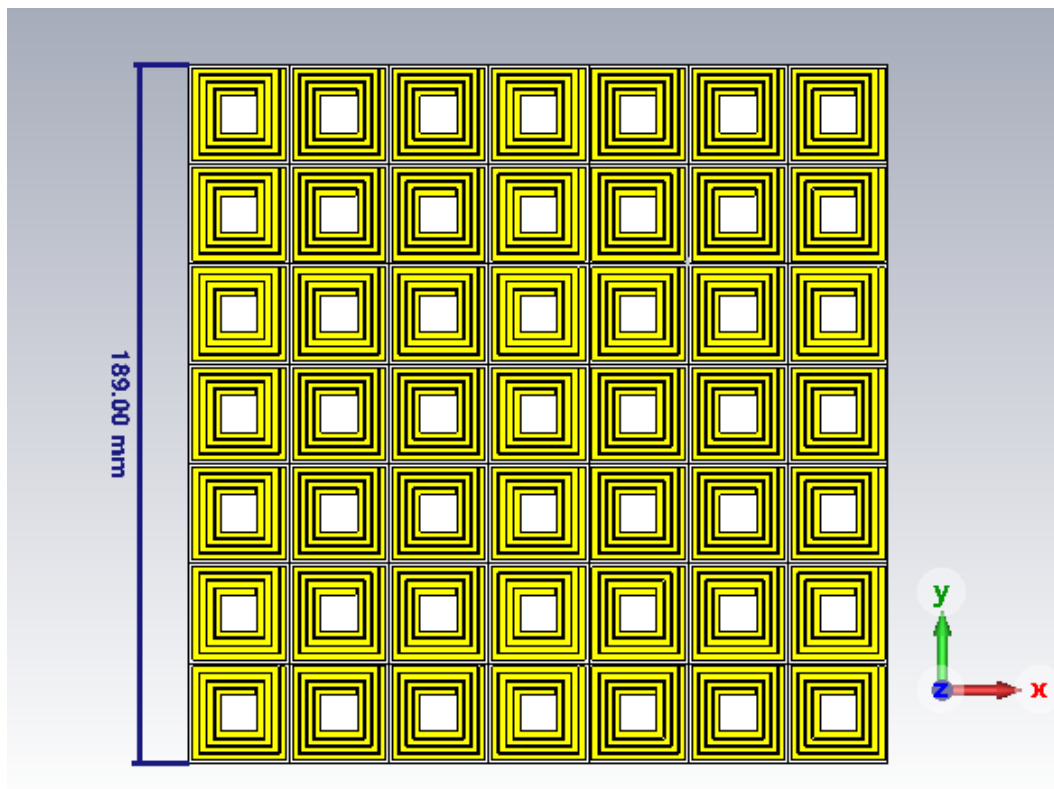


Figure 4.8: Prototypes U1 and U2 with equal central and border regions

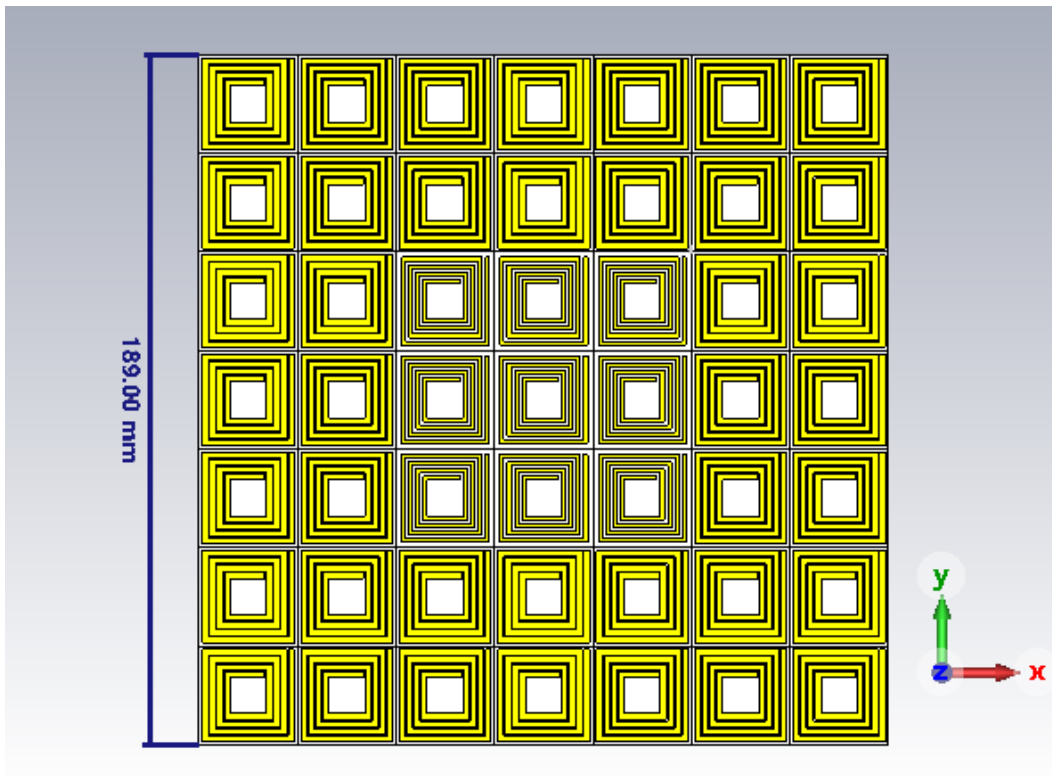


Figure 4.9: Prototype H1 with a central-region and a border-region

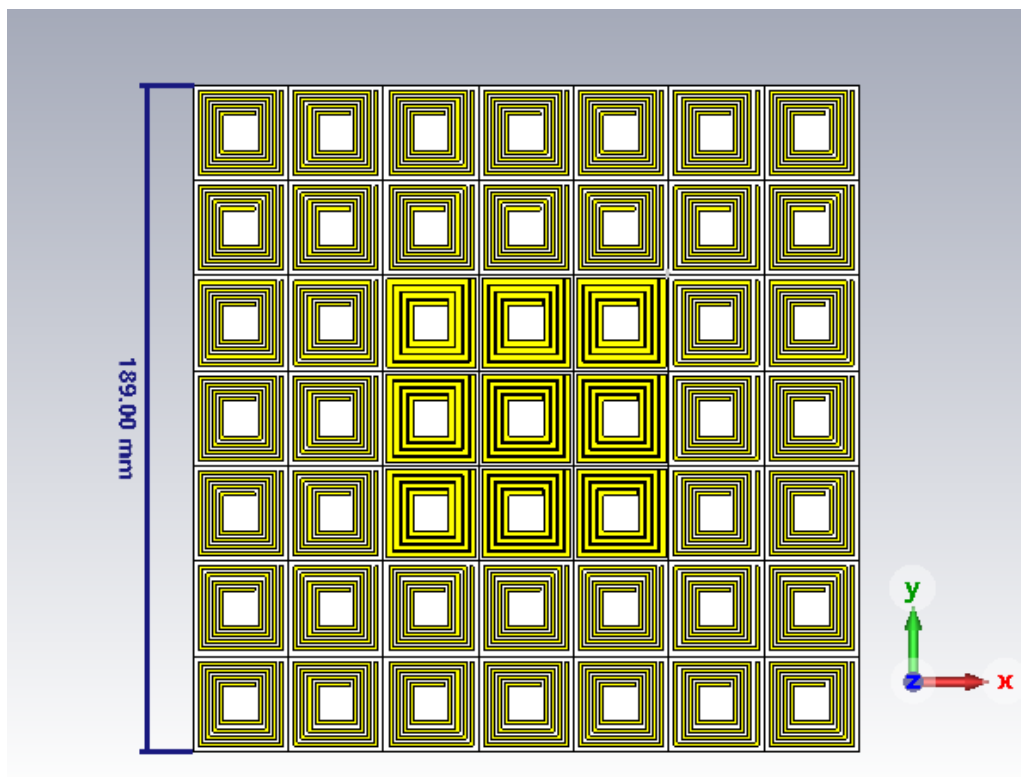


Figure 4.10: Prototype H2 with a central-region and a border-region

As we have discussed before, if both regions are chosen with the same  $g$  and  $w$  values, the maximum MTM gain is achieved in the region where the  $Re\{\mu_r\} < 0$  and  $Im\{\mu_r\} \rightarrow 0$ , as observed for prototypes U1 and U2 (see Table 1). Furthermore, a practical example of the lattice-induced frequency shift, mentioned in section 4.1.3, can be noticed by comparing the operating frequency obtained for U1 ( $f_0 = 245$  MHz) with the operating frequency  $f_0 = 286$  MHz obtained in section 4.1.2 for the same cell ( $g = w = 1$  mm).

Inspired on [78], we propose to evaluate two hybrid prototypes, H1 and H2. At  $f_0 = 245$  MHz, the unit cell ( $g = w = 1$  mm), named C1, presents  $\mu_r < 0$ , while the unit cell ( $g = 0.3$  mm,  $w = 1.7$  mm), named C2, presents  $\mu_r \approx 0$  (slightly negative). Conversely, at  $f_0 = 165$  MHz, the C1 presents  $\mu_r \approx 0$  (slightly positive), while the C2 presents  $\mu_r < 0$ . As it can be seen in Table 1 and Figure 4.11, for both prototypes, H1 or H2, the operating frequency is realized around the range where the central region cell, C1 or C2, presents  $\mu_r < 0$ .

These results suggest that the improved focalization due to  $\mu_r = 0$  at the MTM central region, as claimed by [78], does not occur, despite the fact that reported improvement of the MTM gain by 3 dB can be observed in the obtained results for prototypes H1 and H2 in Table 1 and Figure 4.11.

Table 1: Comparison between MTM uniform and hybrid topologies

Uniform Distribution						
Prototype	Region	$g$ (mm)	$w$ (mm)	$f_0$ (MHz)	$Re\{\mu_r\}$	Gain (dB)
U1	Both	1	1	245	< 0	9
U2	Both	0.3	1.7	165	< 0	5
Non-uniform Distribution						
Prototype	Region	$g$ (mm)	$w$ (mm)	$f_0$ (MHz)	$Re\{\mu_r\}$	Gain (dB)
H1	Central	1	1	252	< 0	12
	Border	0.3	1.7		$\approx 0$	
H2	Central	0.3	1.7	161	< 0	7.5
	Border	1	1		$\approx 0$	

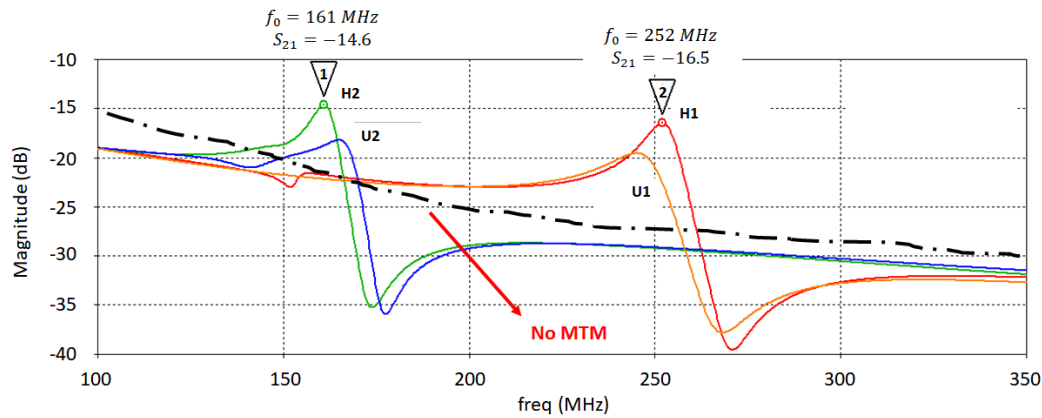


Figure 4.11:  $S_{21}$  of the 4 prototypes, compared with the system without MTM

So, the question remains: why does it happen? Why the MTM gain is improved by the hybrid cells if the central region seems to keep being negative. The answer to that phenomenon is straightforward if we compare the behavior of the fields in the four prototypes (U1, U2, H1 and H2).

The simulated results for prototypes U1 and U2, illustrated in Figure 4.8, are shown in Figures 4.12 to 4.17. Figures 4.12 and 4.13 show the average amplitude of the H-field normal and tangential to the surface of prototype U1, respectively, while Figures 4.14 to 4.15 show the average amplitude of the H-field normal and tangential to the surface of prototype U2, respectively. Moreover, Figures 4.16 and 4.17 show the average density of power flow through the surface of prototypes U1 and U2, respectively.

The obtained results indicate that the focalization of the magnetic field is rather imperfect, due to the intrinsic losses of the constituent materials of the unit cells. These imperfections affect the phase and amplitude of the magneto-inductive wave propagating on the surface of the MTM slab, which is the source of the lens-like behavior of the structure, as discussed in section 2.3, implying in a reduced MTM gain.

The simulated results for prototypes H1 (illustrated in Figure 4.9) and H2 (illustrated in Figure 4.10) are shown in Figures 4.18 to 4.23. Figures 4.18 and 4.19 show the average amplitude of the H-field normal and tangential to the surface of prototype H1, respectively, while Figures 4.20 and 4.21 show the average amplitude of the H-field normal and tangential to the surface of prototype H2, respectively. Moreover, Figures 4.22 and 4.23 show the average density of power flow through the surface of prototypes H1 and H2, respectively.

Curiously, the loss of coherence of the magneto-inductive wave observed in U1 and U2 is drastically reduced when hybrid MTM like H1 and H2 are employed, resulting in a higher net gain. Qualitatively speaking, due to the imperfection of the constituent materials of the unit cells (copper, FR4, etc), the magnitude of the equivalent  $\mu_r$  must be modulated throughout the MTM surface. In other words, a non-uniform distribution of  $\mu_r$  seems to contribute to compensate the imperfections of the employed constituent materials.

In order to understand in detail the effect of the modulation of the magnitude of  $\mu_r$  on the phase, amplitude and propagation of the magneto-inductive wave on MTM surfaces, the theory presented in section 2.3 must be extended for hybrid lattices, which is intended to be done in future works. Also, at the obtained numerical results for H1 and H2 must be compared with experimental evidence in order to confirm if  $\mu_r$  should be null or negative at the central region.

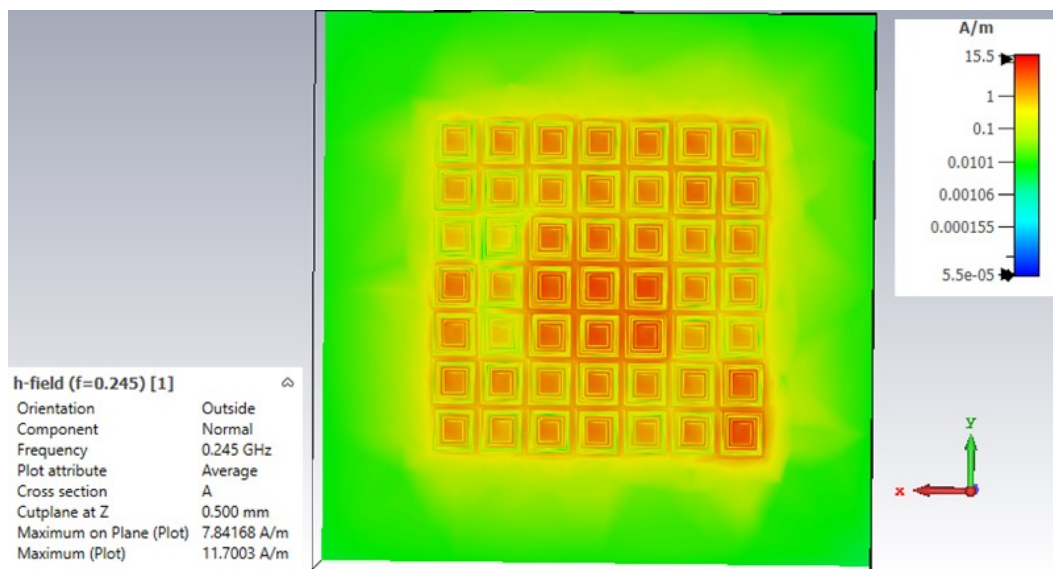


Figure 4.12: Average amplitude of the H-field normal to the surface of prototype U1

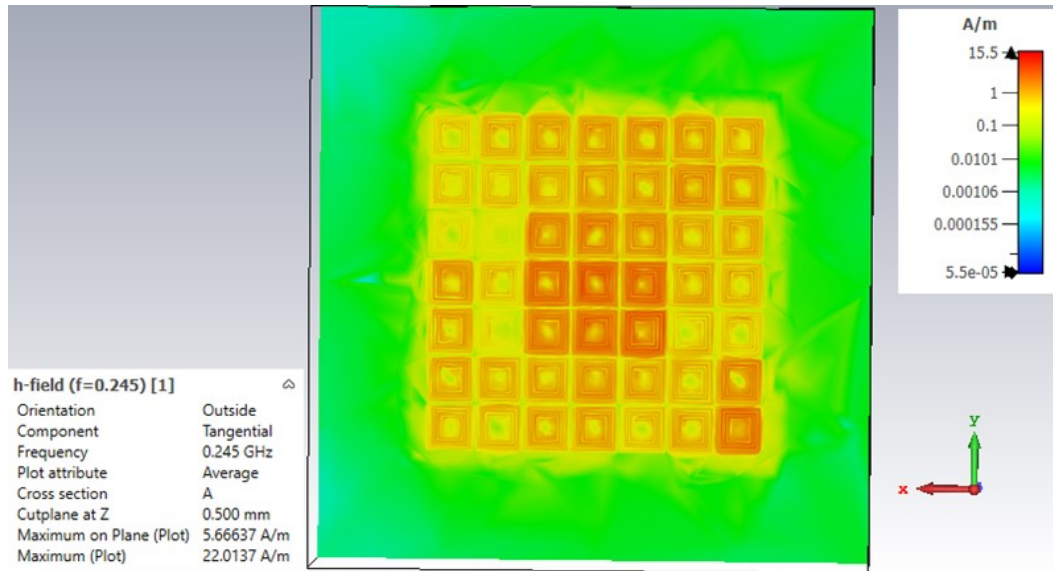


Figure 4.13: Average amplitude of the H-field tangential to the surface of prototype U1

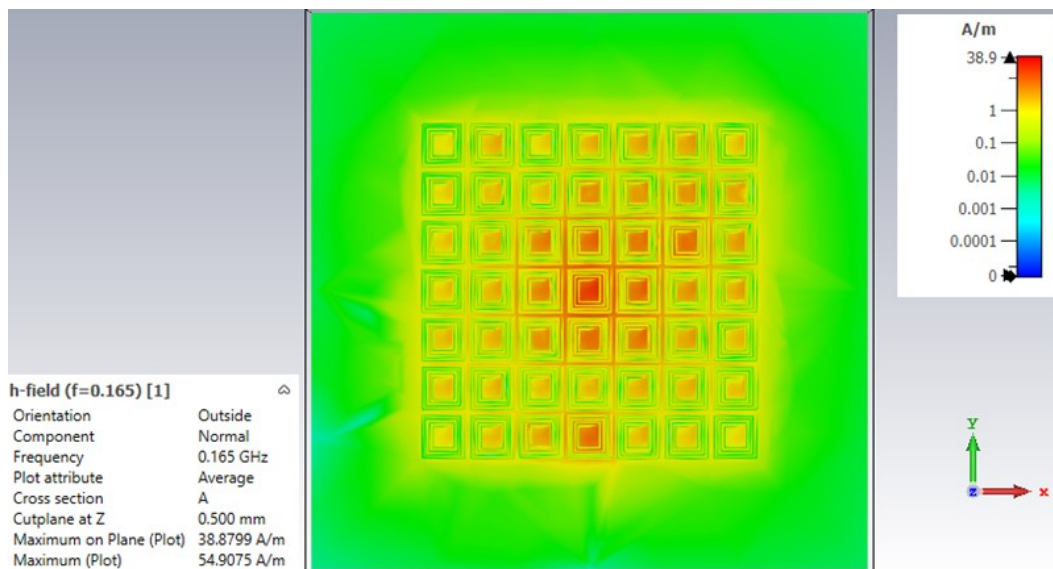


Figure 4.14: Average amplitude of the H-field normal to the surface of prototype U2

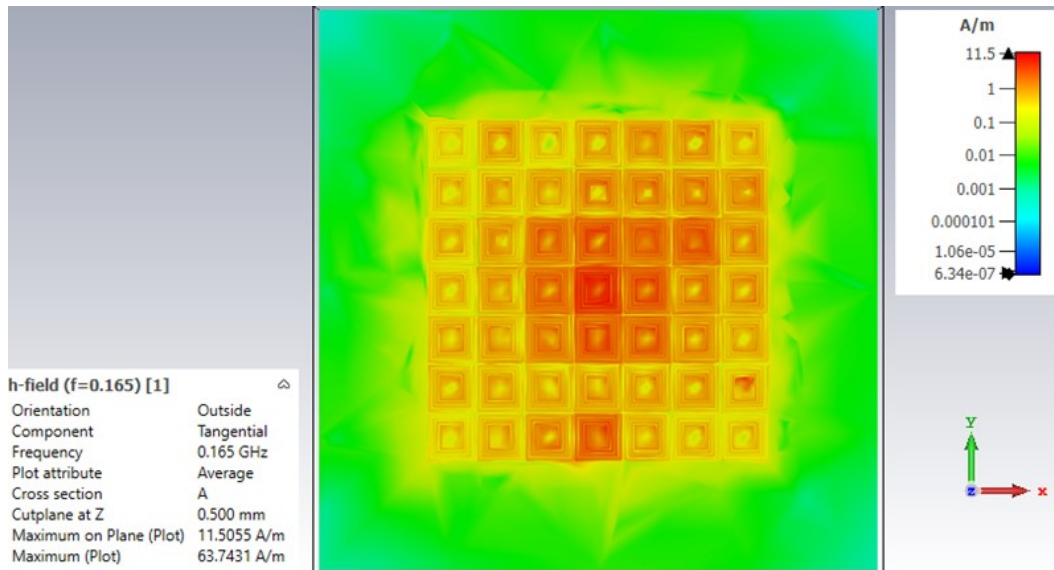


Figure 4.15: Average amplitude of the H-field tangential to the surface of prototype U2

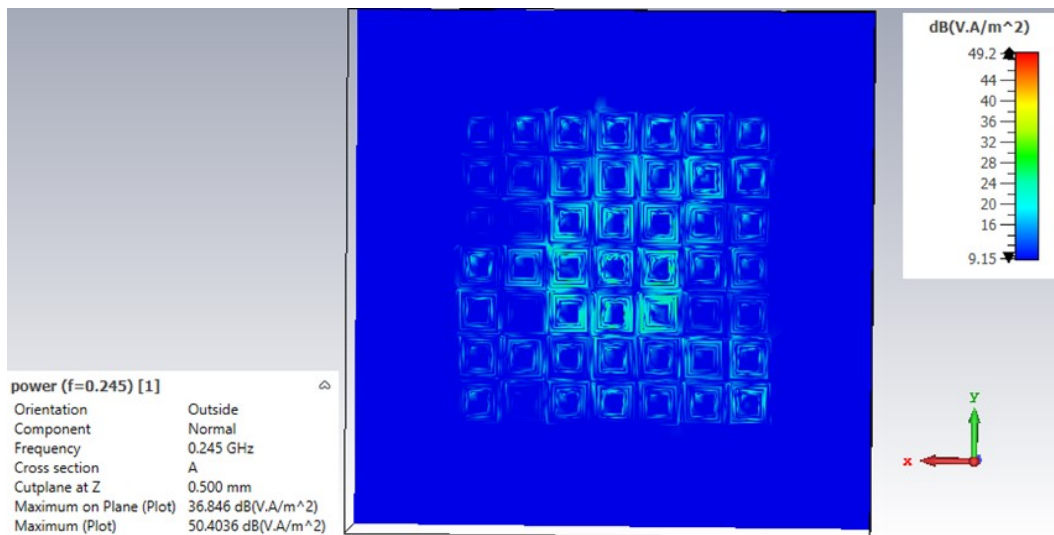


Figure 4.16: Average density of power flow through the surface of prototype U1

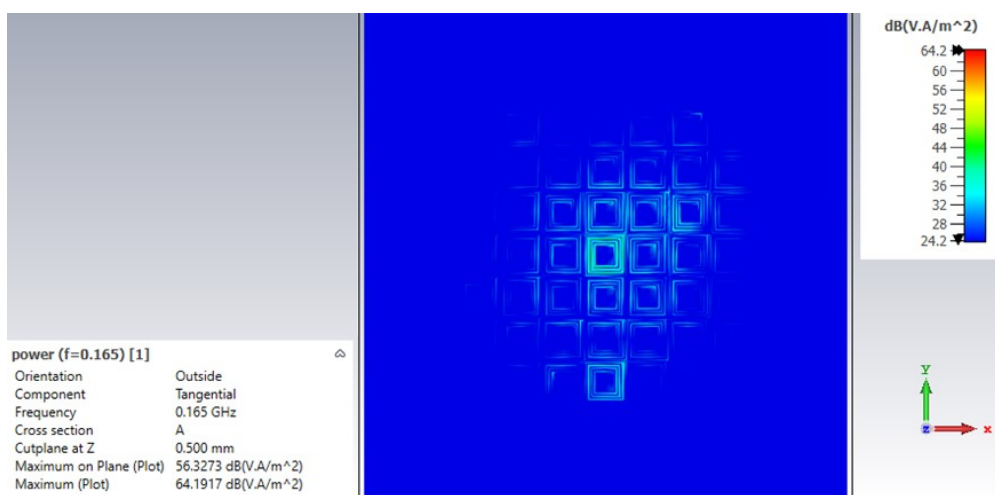


Figure 4.17: Average density of power flow through the surface of prototype U2

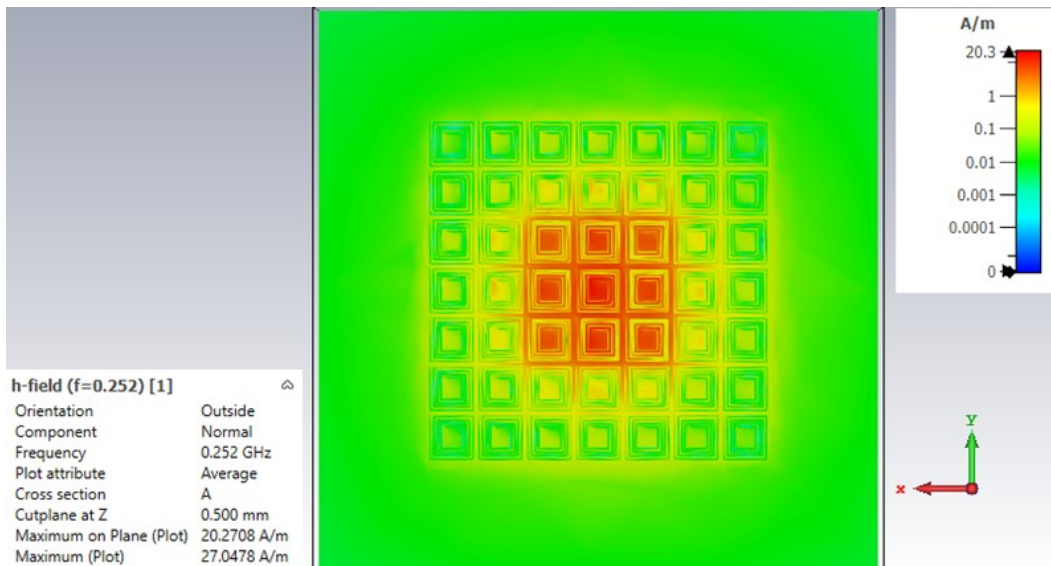


Figure 4.18: Average amplitude of the H-field normal to the surface of prototype H1

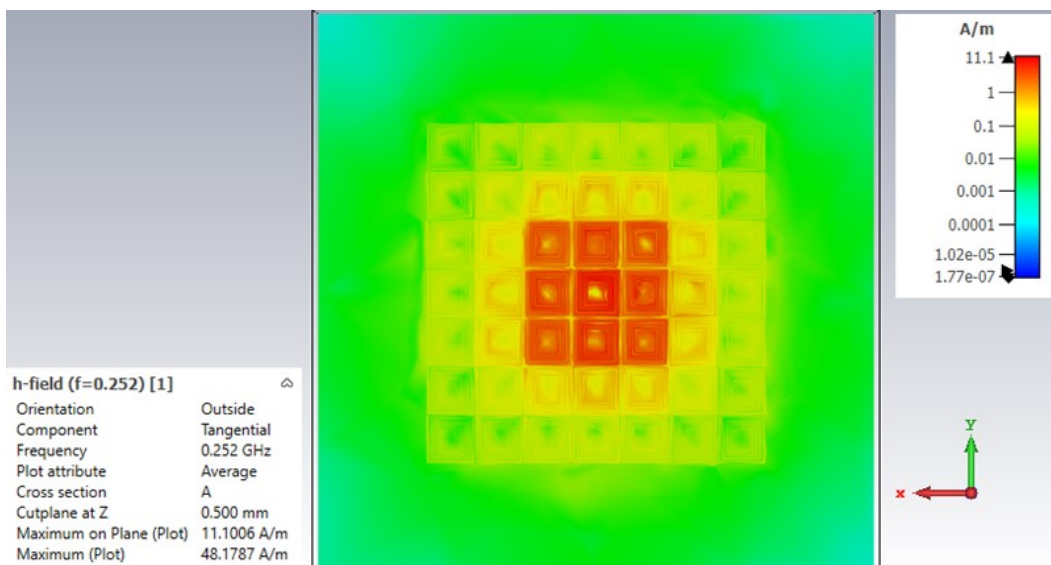


Figure 4.19: Average amplitude of the H-field tangential to the surface of prototype H1

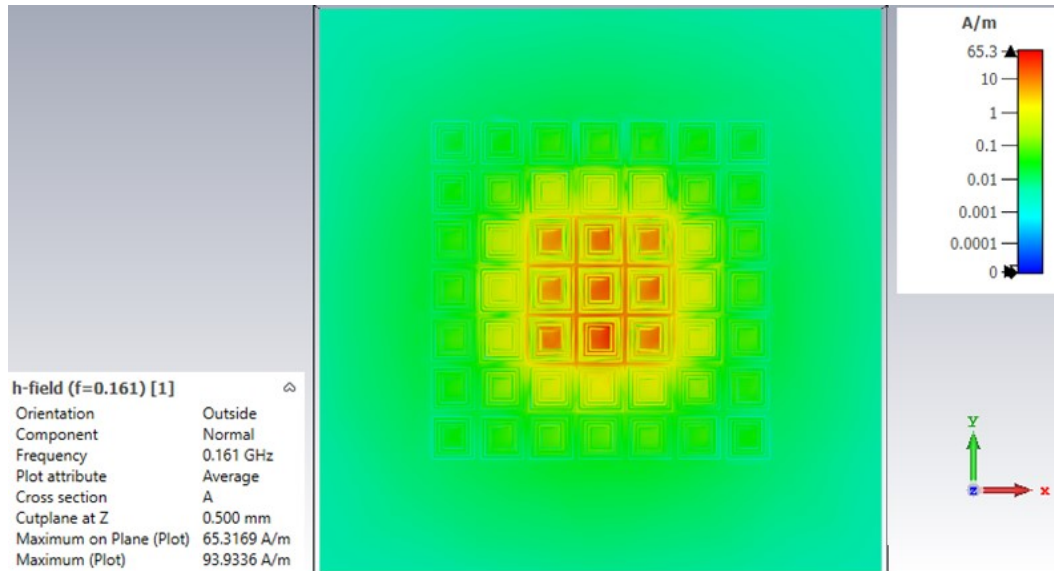


Figure 4.20: Average amplitude of the H-field normal to the surface of prototype H2

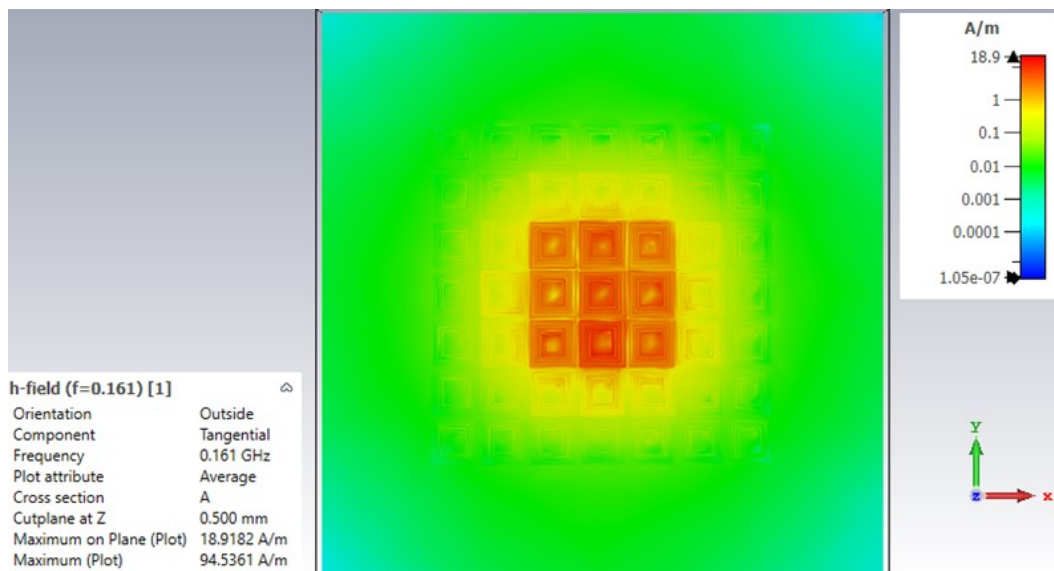


Figure 4.21: Average amplitude of the H-field tangential to the surface of prototype H2

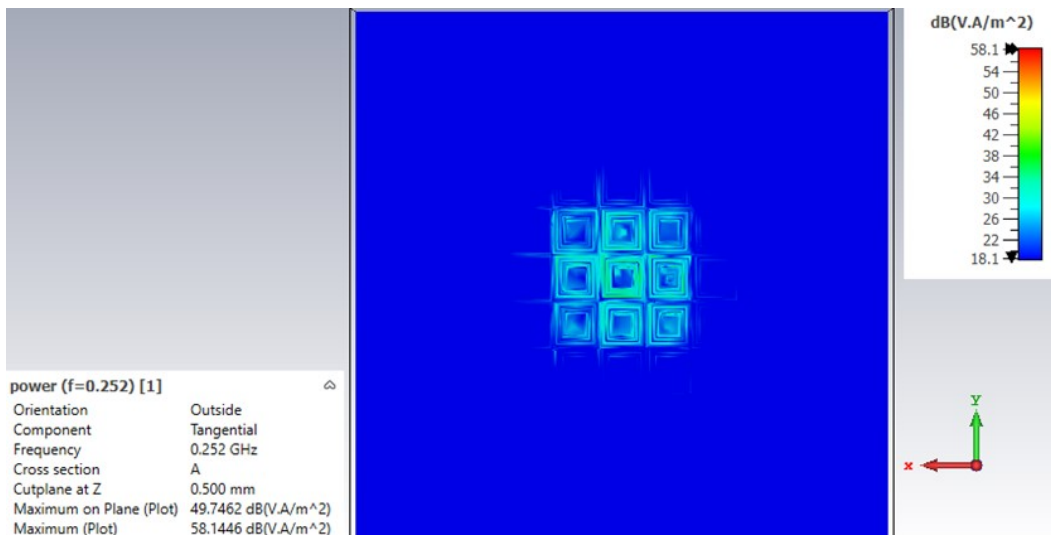


Figure 4.22: Average density of power flow through the surface of prototype H1

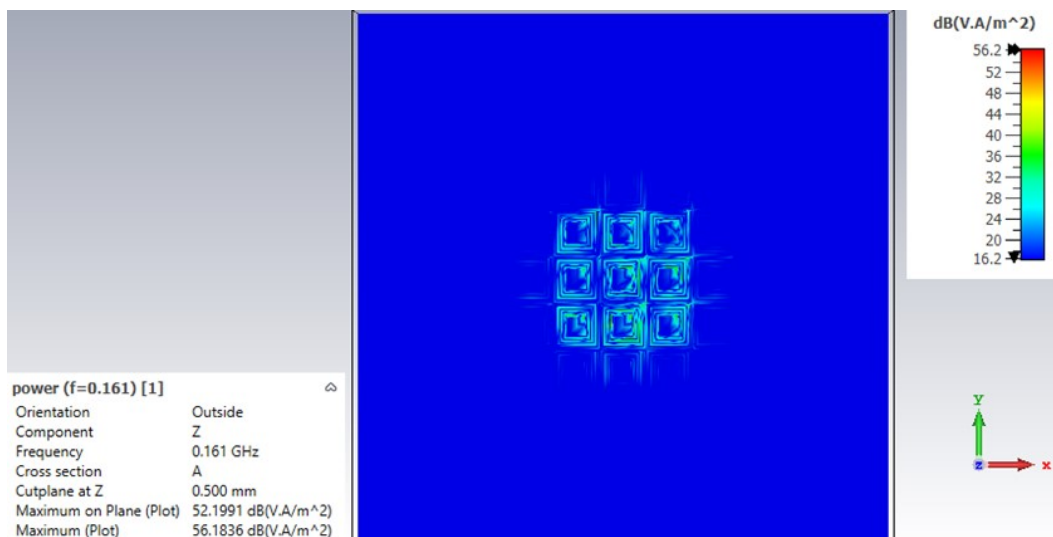


Figure 4.23: Average density of power flow through the surface of prototype H2

#### 4.1.5

##### DSRR with coarse tuning control in air, water and seawater

For the evaluation of the coarse tuning of the proposed DSRR unit-cell using  $C_{SMD} = 0.15 \mu F$ , the MTMs were inserted at the same plane of the coil to maximize the coupling between the drivers and lenses. Since the MTM has a square shape, two square coils were considered for the circuitry of the transmitter and receiver, aiming to simplify their integration with MTM crystals for simulation purposes. Since the results would be similar if a large array were used, only a 2x2 lattice was considered in order to reduce the simulation time.

Two basic scenarios were considered: the first one, called prototype 1 (P1), assumes that both the transmitting and receiving coils have the same dimensions (see Figures 4.24 and 4.25); and the second one, called prototype 2 (P2), considers that the receiving coil is much smaller than the transmitting one (see Figures 4.26 and 4.27). The dimensions of P1 and P2 are:

- $d_{11} = d_{12} = 55 \text{ mm}$
- $d_{21} = d_{22} = 25 \text{ mm}$
- $d_1 = d_2 = 10 \text{ mm}$

Furthermore, both scenarios (P1 and P2) considered three different inductive transmission media: air ( $\epsilon_r = 1$ ), freshwater ( $\epsilon_r = 81$ ) and seawater ( $\epsilon_r = 81, \sigma = 5 \text{ S/m}$ ).

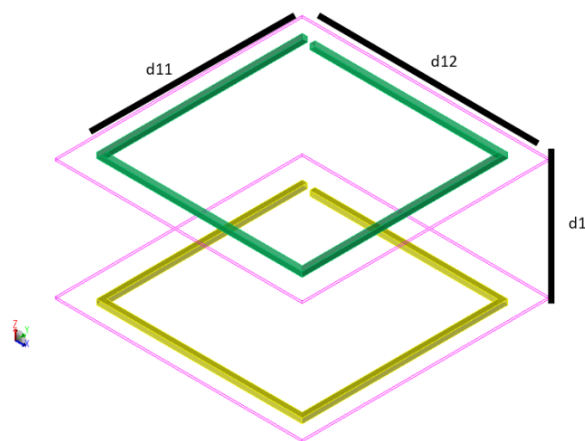


Figure 4.24: P1 system

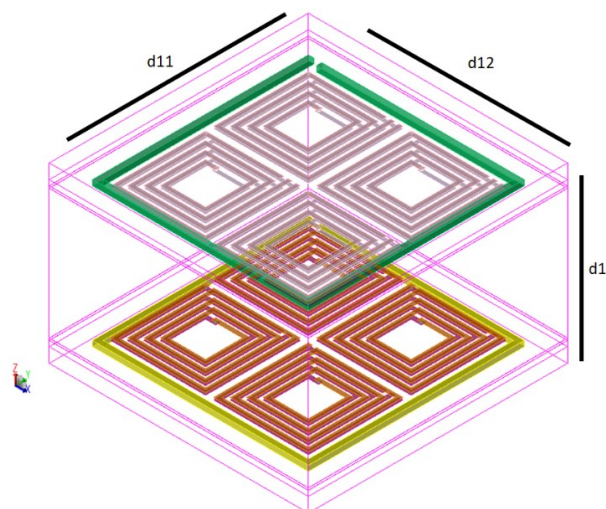


Figure 4.25: P1 system assisted by MTM

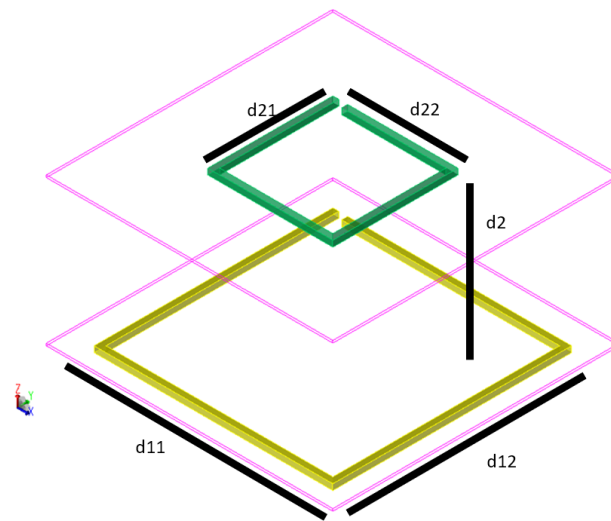


Figure 4.26: P2 system

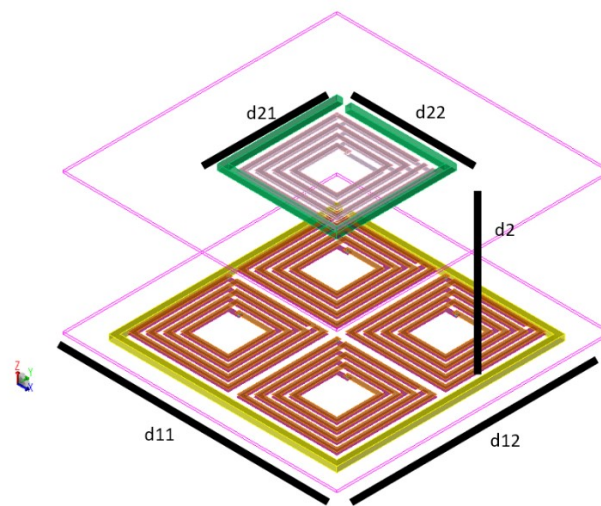


Figure 4.27: P2 system assisted by MTM

Figure 4.28 and Figure 4.29 show the simulated results obtained for the MTM gain in air, freshwater and seawater, for both scenarios P1 and P2, respectively. The transfer functions were computed in relation to the respective prototypes in the air, without MTM. As it can be seen, the MTM gain of the system is the same in both P1 and P2 cases:  $10\text{ dB}$ , in the air and in freshwater, and  $6.2\text{ dB}$ , in seawater. However, due to the reduction of the coil effective area,  $S_{21}$  is much smaller (more than  $20\text{ dB}$ ) for P2, as shown in Figure 4.30. The size difference between the drivers is then a major source of loss.

Considering the UWSNs, this is particularly problematic for the transmission between the UD and the sensor field, since the SN coil is necessarily smaller than the UD one. On the other hand, the power transfer between the BS and the UD can be optimized since they can have coils with the same dimensions.

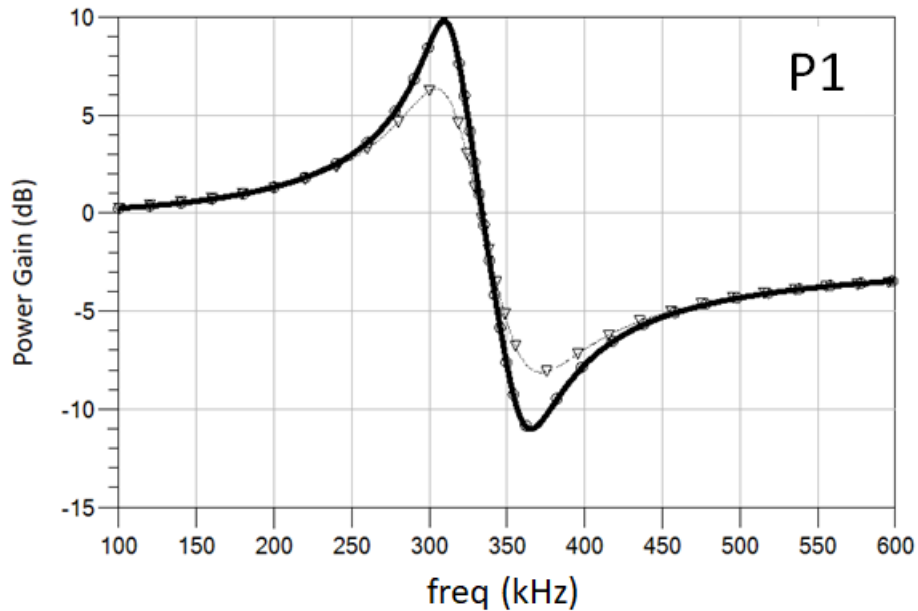


Figure 4.28: MTM gain of P1 in air (solid line), freshwater (circle) and seawater (triangle) in comparison with P1 in the air without MTM

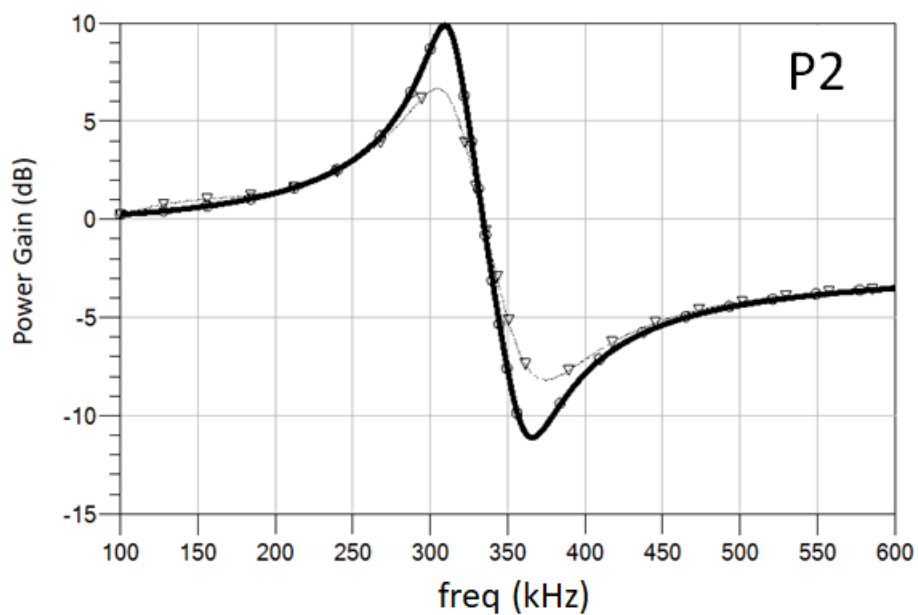


Figure 4.29: MTM gain of P2 in air (solid line), freshwater (circle) and seawater (triangle) in comparison with P2 in the air without MTM

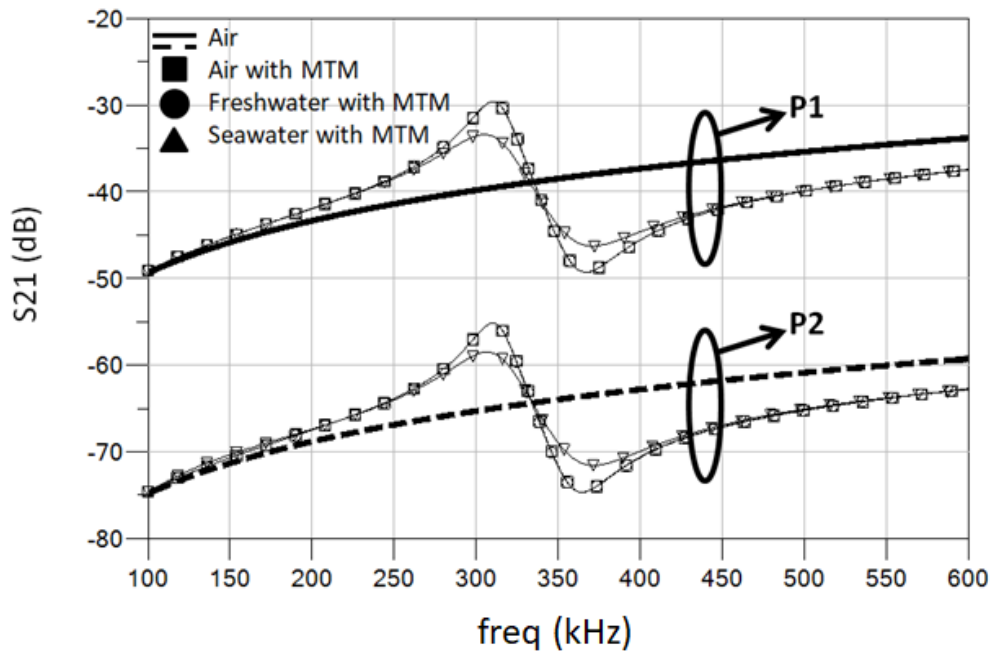


Figure 4.30:  $S_{21}$  of P1 and P2 in different environments

Besides, the impact of the misalignment between the coils is also investigated. In this way, simulations were performed considering a misalignment of 50% between the coils of P1 without and with MTM, as illustrated in Figures 4.31 and 4.32, respectively. As shown in Figures 4.33 and 4.34, even for a misalignment up to 50%, the simulated results indicate that a misaligned P1 still has a better performance than a perfectly aligned P2. It implies that new MTM structures conceived and adapted for power transfer between heterogeneous coils must be investigated.

Finally, notice that the behavior of the MTMs in this section is basically the same, in shape and magnitude of the curves, obtained in sections 4.1.1 to 4.1.4, only shifted in frequency by the coarse tuning element  $C_{SMD}$ .

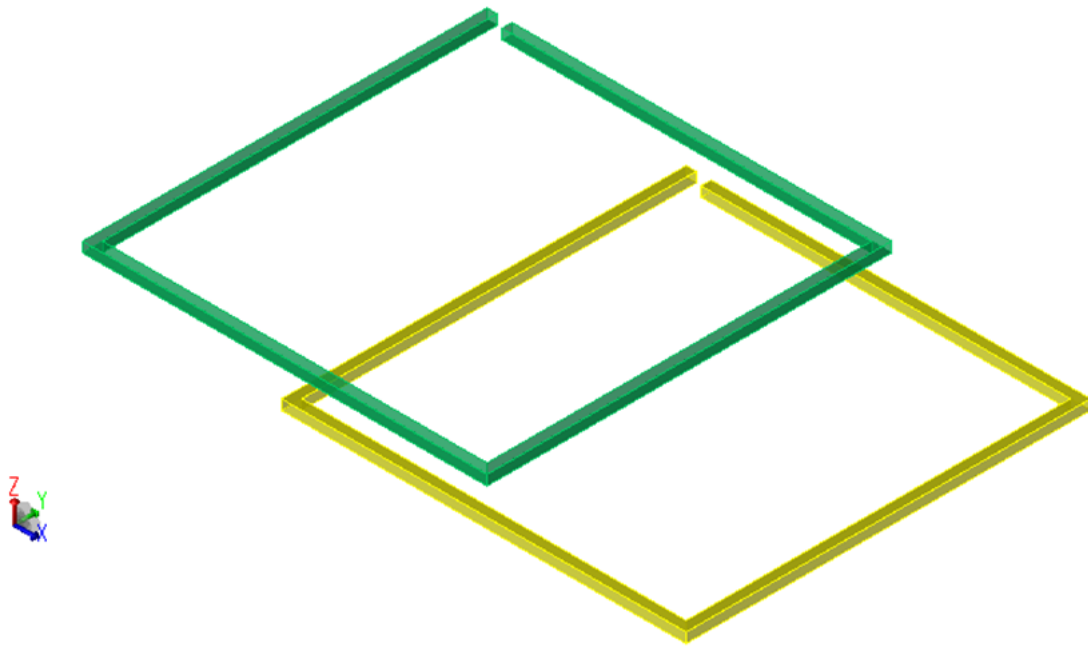


Figure 4.31: Misaligned P1 system

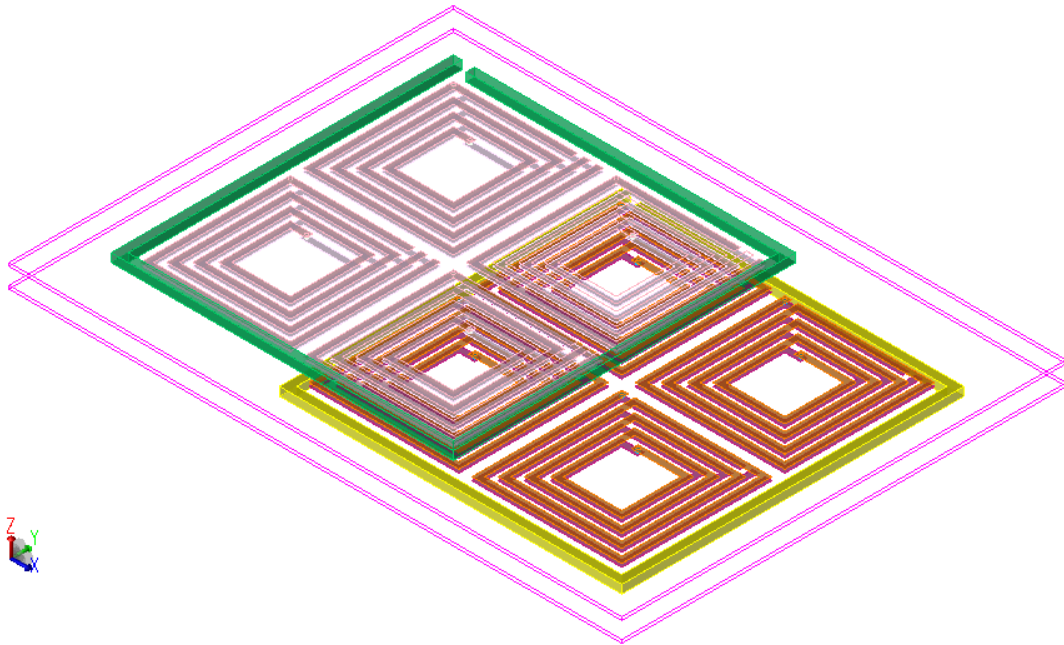


Figure 4.32: Misaligned P1 system assisted by MTM

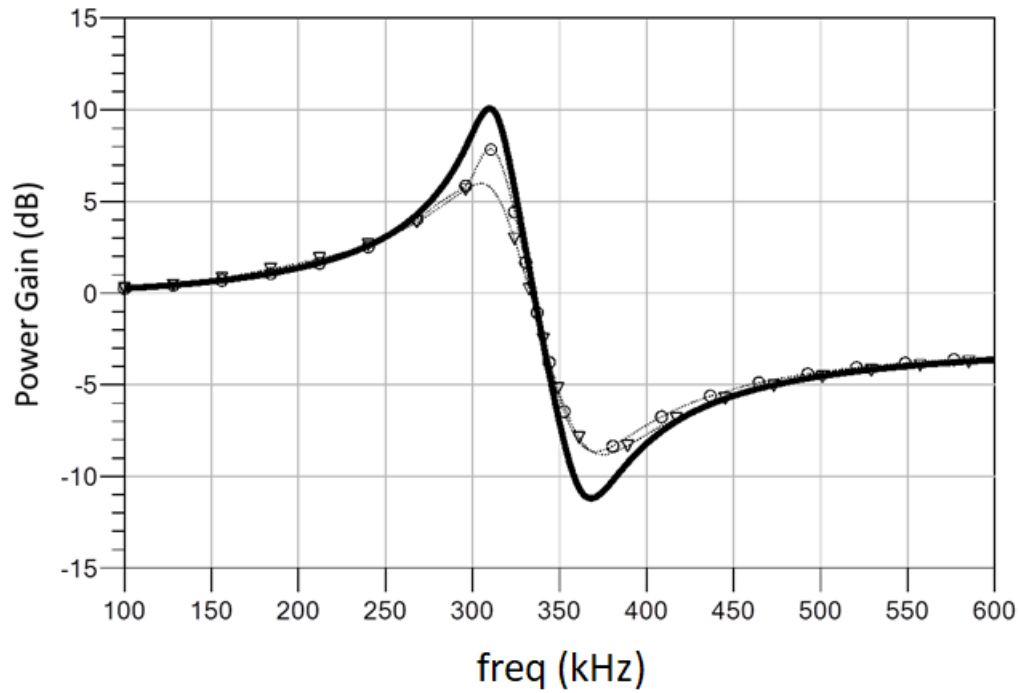


Figure 4.33: MTM gain of misaligned P1 in air (solid line), freshwater (circle) and seawater (triangle) in comparison with misaligned P1 in the air without MTM

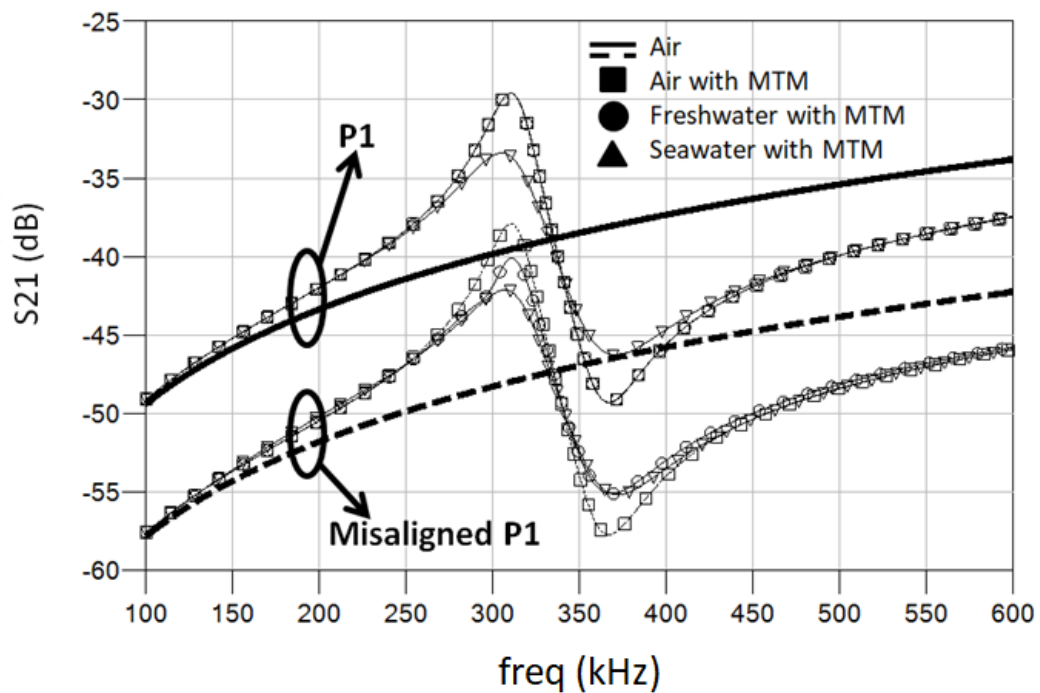


Figure 4.34:  $S_{21}$  of the P1 and misaligned P1 in the considered environments

## 4.2

### Effect of insulation on efficiency

A way of preventing losses in seawater is to insulate the conductors of the TX and RX coils with a dielectric material. Figure 4.35 shows non-insulated coils and Figure 4.36 shows insulated coils immersed in seawater.

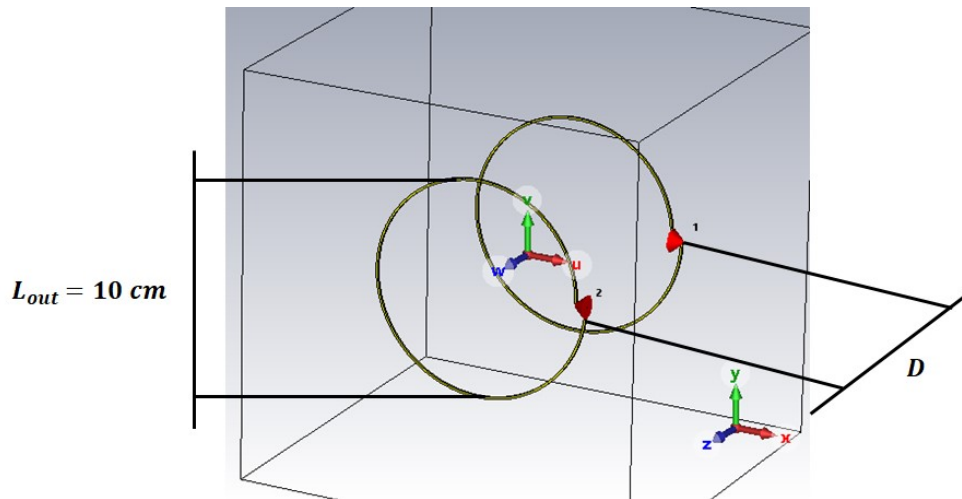


Figure 4.35: Non-insulated coils immersed in seawater:  $\sigma = 5 \frac{S}{m}$ ,  $r = 5 \text{ cm}$

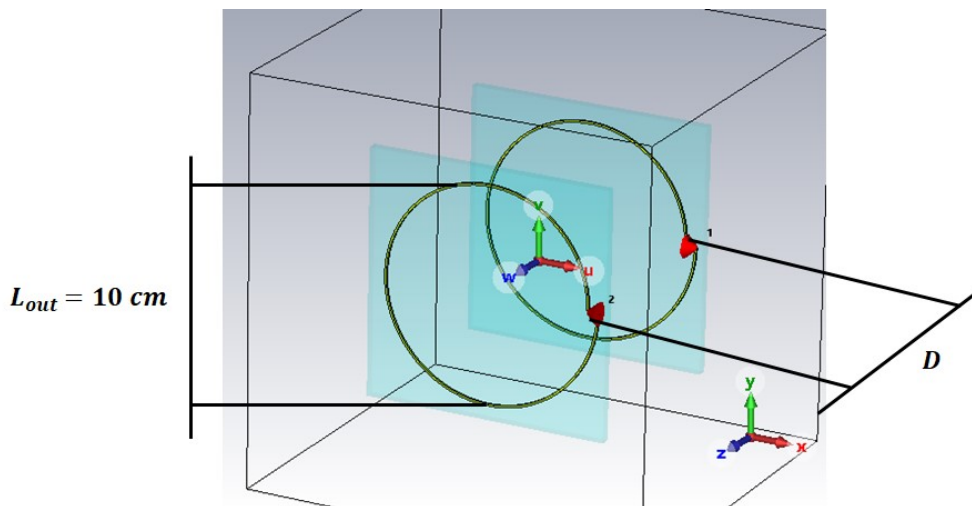


Figure 4.36: Insulated coils immersed in seawater:  $\sigma = 5 \frac{S}{m}$ ,  $r = 5 \text{ cm}$

Figures 4.37 to 4.39 show the simulated transfer functions for non-insulated coils (Figure 4.37), air-insulated coils (Figure 4.38) and freshwater-insulated coils (Figure 4.39) immersed in seawater, considering three different separation distances:  $1 \text{ cm}$ ,  $5 \text{ cm}$  and  $15 \text{ cm}$ . Note that the achieved results indicate that insulation reduces losses in more than  $10 \text{ dB}$ .

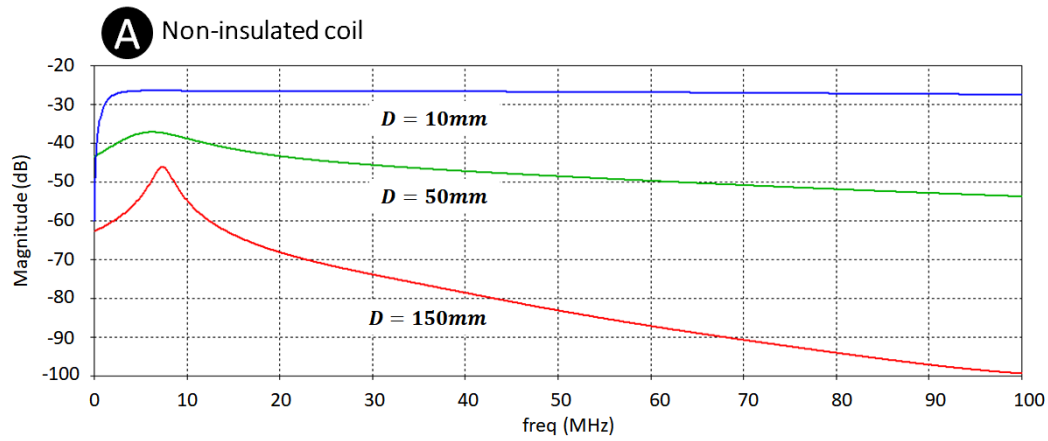


Figure 4.37: Transfer function of the non-insulated coils immersed in seawater, with separation distance  $D = 1\text{ cm}$ ,  $D = 5\text{ cm}$  and  $D = 15\text{ cm}$

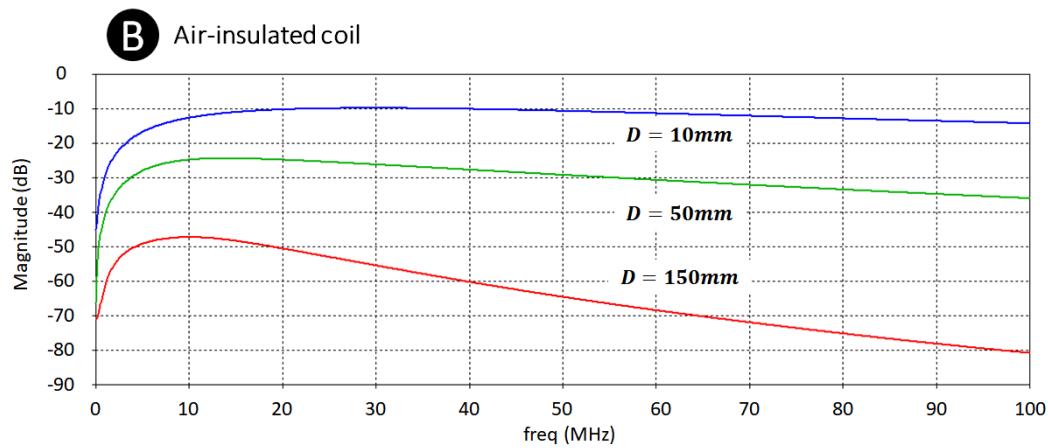


Figure 4.38: Transfer function of the air-insulated coils immersed in seawater, with separation distance  $D = 1\text{ cm}$ ,  $D = 5\text{ cm}$  and  $D = 15\text{ cm}$

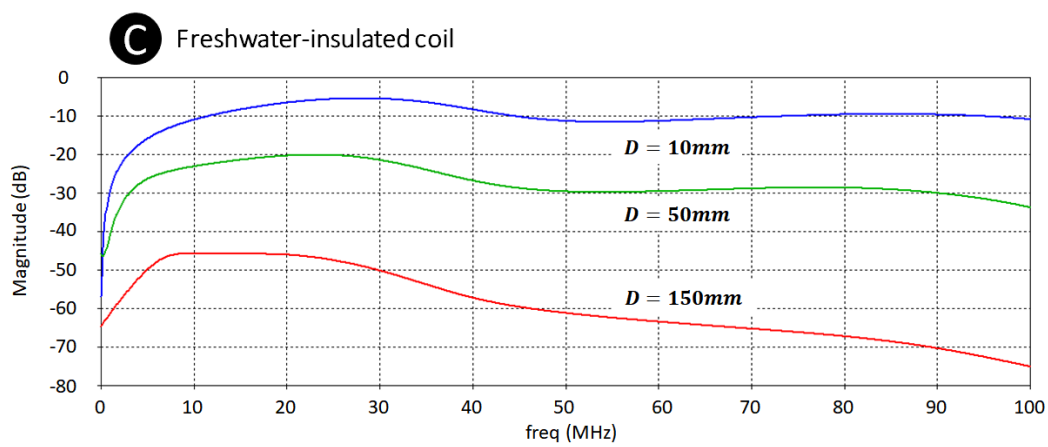


Figure 4.39: Transfer function of the freshwater-insulated coils immersed in seawater, with separation distance  $D = 1\text{ cm}$ ,  $D = 5\text{ cm}$  and  $D = 15\text{ cm}$

However, one important aspect usually ignored by most designers of UWPT systems is the influence of the module of the dielectric constant of the insulation on the PTE. In this way, Figure 4.40 presents a comparison between the transfer function with air (green) and freshwater (red) insulation, for  $D = 5 \text{ cm}$ . As shown in Figure 4.40, when the dielectric constant of the insulating material is similar to the seawater, PTE is improved in some frequency ranges. This material matching gain could achieve values as high as  $5 \text{ dB}$ , which is far from being negligible gain. Notice that the high-dielectric gain in Figure 4.40 become null with a defined periodicity. This effect is due to a sort of surface resonance mode that can propagates at the interface insulation-seawater at  $50 \text{ MHz}$  and any of its harmonics.

The source of this high-dielectric gain is an improvement of the E-field distribution around the TX coil conductor. Computational simulations were performed to demonstrate this fact. Figures 4.41 and 4.42 show the average amplitude of the E-field tangential of the air-filled (Figure 4.41) and freshwater-filled (Figure 4.42) insulation slab. As it can be seen, when the insulating permittivity is close to the water one, the component of the E-field perpendicular to the magnetic flux is more smoothly distributed, which is equivalent to say that the impedance matching between the drivers is facilitated when the insulation has a dielectric constant similar to the medium.

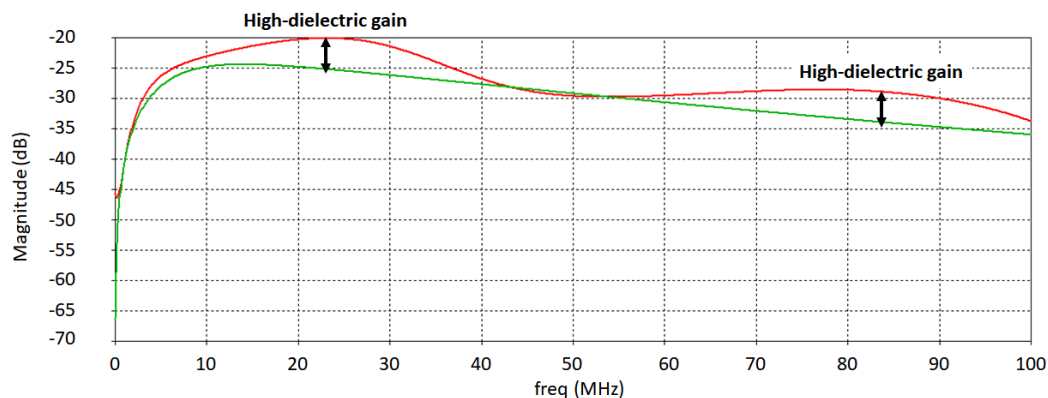


Figure 4.40: Comparison between the transfer function with air (green) and freshwater (red) insulation for  $D = 5 \text{ cm}$

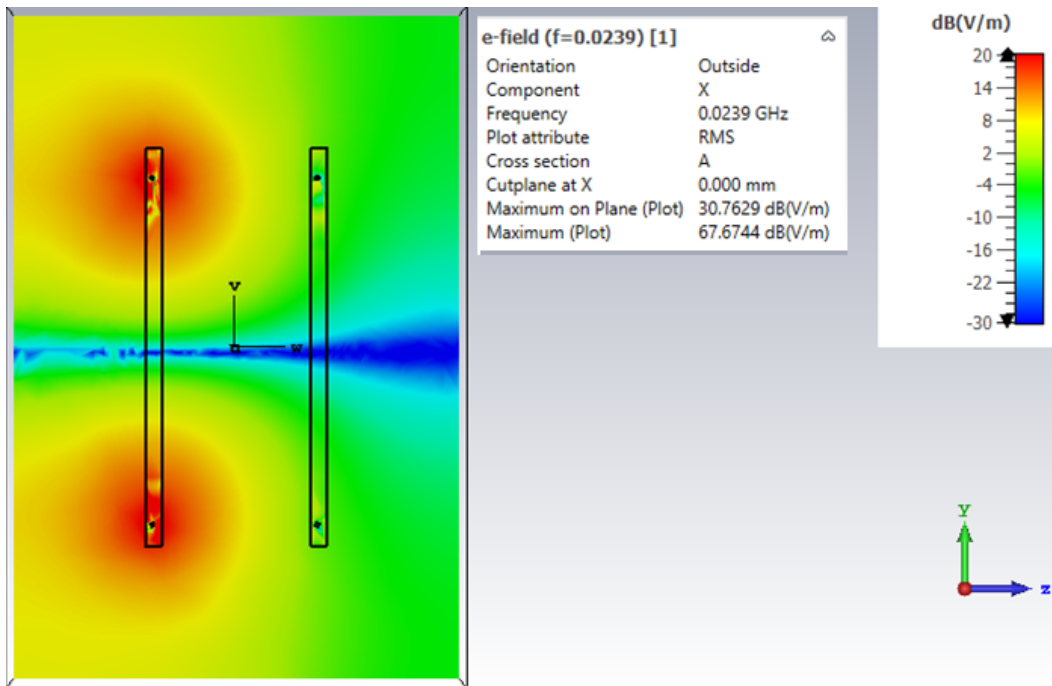


Figure 4.41: Average amplitude of the component of the E-field perpendicular to the magnetic flux at  $f_0 = 23.90 \text{ MHz}$  with air-insulated coils

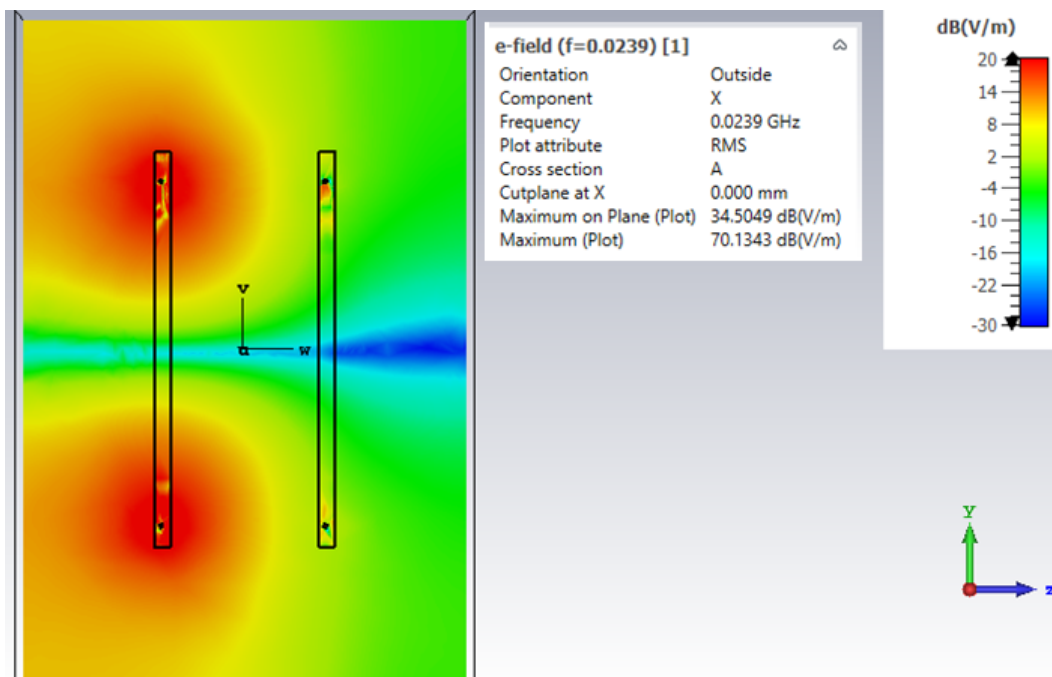


Figure 4.42: Average amplitude of the component of the E-field perpendicular to the magnetic flux at  $f_0 = 23.90 \text{ MHz}$  with freshwater-insulated coils

### 4.3

#### Artificial magnetic reflectors based on TL-mode coils

As shown in Figure 4.43, a bifilar coil structure can be excited in TL or antenna mode. When the coil is excited using the TL mode, not only its radiation resistance is set to a minimum, but almost no magnetic flux can pass through it. This means TL-mode coils can be used as a highly efficient unit cells for MTM-based magnetic reflectors, as it is further demonstrated in this section.

One important feature of TL-mode coils is that their response cannot be controlled by lumped capacitors connected in series with the conductor, like in MNG MTM lenses, because in this case the intrinsic capacitance of the TL-mode coil will also be in series with the added capacitance:

$$\frac{1}{C_{total}} = \frac{1}{C_{added}} + \frac{1}{C_{intrinsic}} \quad (48)$$

which means  $C_{total} \rightarrow C_{intrinsic}$ , since  $C_{added} \gg C_{intrinsic}$ .

Hence, the effective control of the coarse tuning of TL-mode unit cell must be made connecting the lumped element in parallel with the coil conductor, as shown in Figure 4.44.

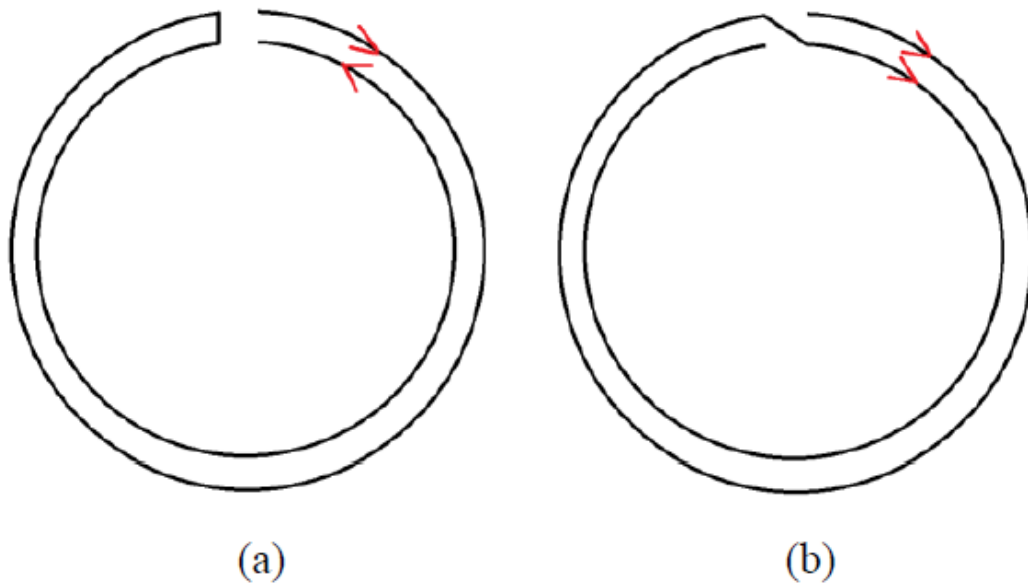


Figure 4.43: Currents on TL (a) and antenna (b) mode coils

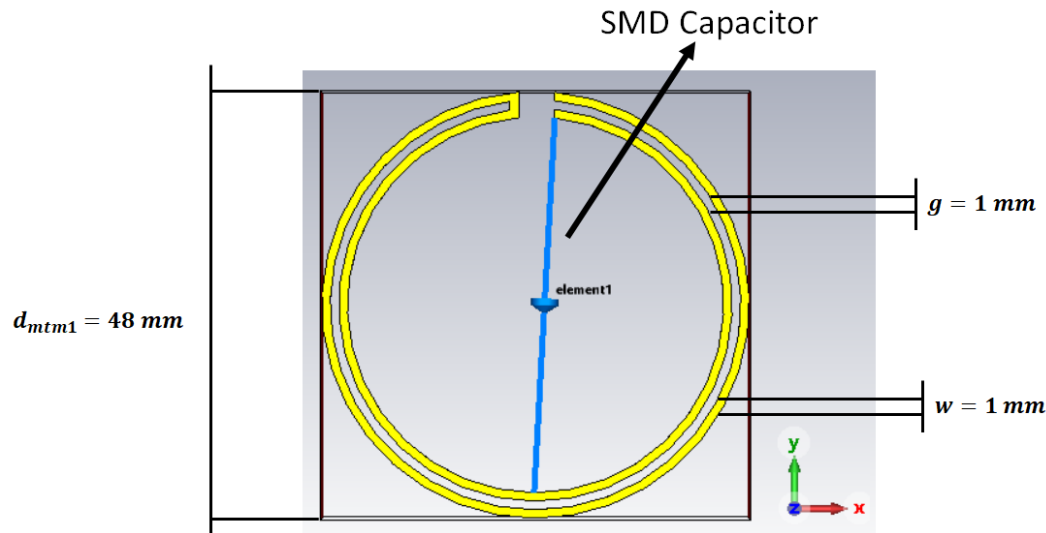


Figure 4.44: TL-mode unit cell with coarse tuning control

For the examples shown in this section it was considered a TL-mode unit cell, consisting of copper conductors using air as substrate, with the following characteristics:

- **Outer diameter:**  $d_{mtm1} = 48 \text{ mm}$
- **Coarse tuning element:**  $C_{SMD} = 10 \text{ pF up to } 1 \text{ nF}$
- **Conductor width:**  $w = 1 \text{ mm}$
- **Gap between turns:**  $g = 1 \text{ mm}$

The simulated results show that, when the proposed TL-mode cell is employed as a magnetic reflector (see Figure 4.45), placed not in-between but behind the TX and RX coils, a high MTM gain is also achieved (see Figure 4.46). The simulations were performed considering that the excitation coils outer dimensions  $L_{out} = 60 \text{ mm}$ , separated by  $D = 25 \text{ mm}$  from each other, and separated by  $D_2 = 3 \text{ mm}$  from their assistant reflector. In fact, the obtained gain with this strategy is even higher (about  $15 \text{ dB}$ ) than the one (less than  $10 \text{ dB}$ ) obtained with MTM lenses, and with a better bandwidth.

As shown by Figure 4.47, the obtained response of the equivalent  $\mu_r$  of the TL-mode unit cell present a loss-free ( $Im\{\mu_r\} \approx 0$ ), paramagnetic response ( $Re\{\mu_r\} > 1$ ) in its gain region, and not a MNG one, as in MTM lenses. In fact, paramagnetic materials are already employed as reflectors in UWPT systems in order to increase their performance, as the one presented by Do Won Kim from Curtin University, Australia, during the 2019 Autonomous Underwater Technology

(AUT) Conference promoted by the SUT [79] (see Figure 4.48). However, in [79], the reflectors are made of an array of ferromagnetic bars, which are bulky, expensive and power consuming.

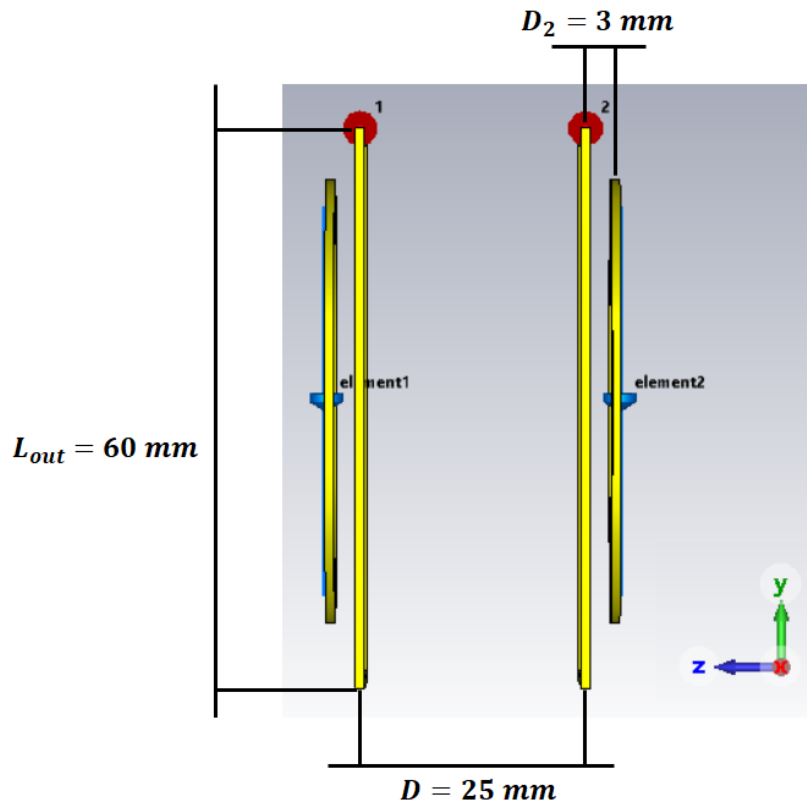


Figure 4.45: TL-mode cells employed as reflectors. Notice that the MTM cells are placed behind the coupled coils

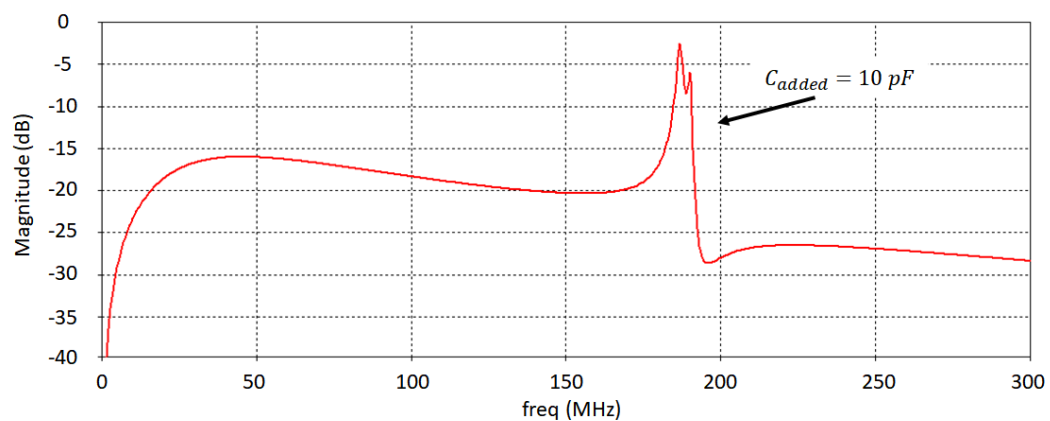


Figure 4.46: Simulation of the gain when the TL-mode unit-cell is employed as a reflector

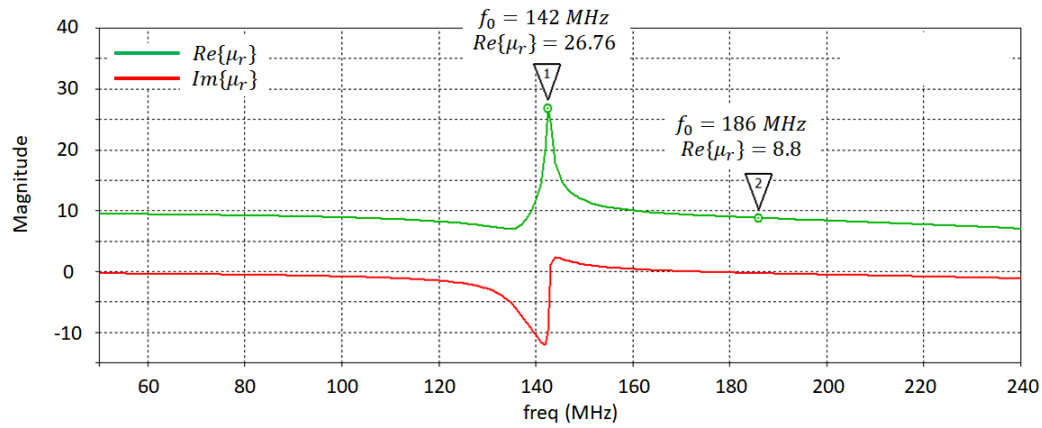


Figure 4.47: Equivalent  $\mu_r$  of the proposed TL-mode unit-cell

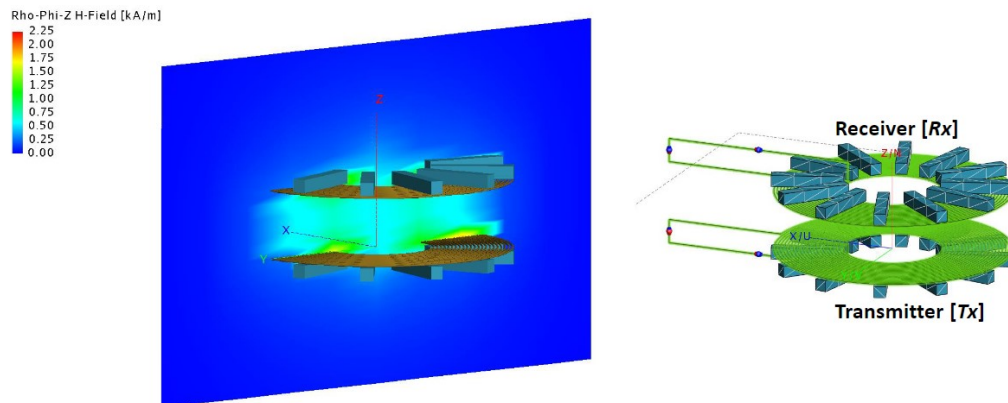


Figure 4.48: UWPT system using an array of ferromagnetic bars as a reflector [79]

Moreover, TL-mode cells present a feature which is particularly interesting for data transmission: they are intrinsically dual band, presenting two gain regions, as it is shown in Figure 4.49. Nonetheless, as it can be seen by comparing Figure 4.49.(a) and Figure 4.49.(b), the proposed coarse-tuning strategy for TL-mode cells can only control the gain region at the lower band. In this way, when  $C_{added} = 10 \text{ pF}$  is changed to  $C_{added} = 1 \text{ nF}$ , only the first gain band moves to lower operating frequency, while the second gain band remains completely transparent to the coarse tuning element. Also, the TL-mode cell second resonance tends to present a much lower gain than the first one. Despite that, further investigations must be performed to figure out if both bands could be controlled simultaneously and if their gain can be equalized.

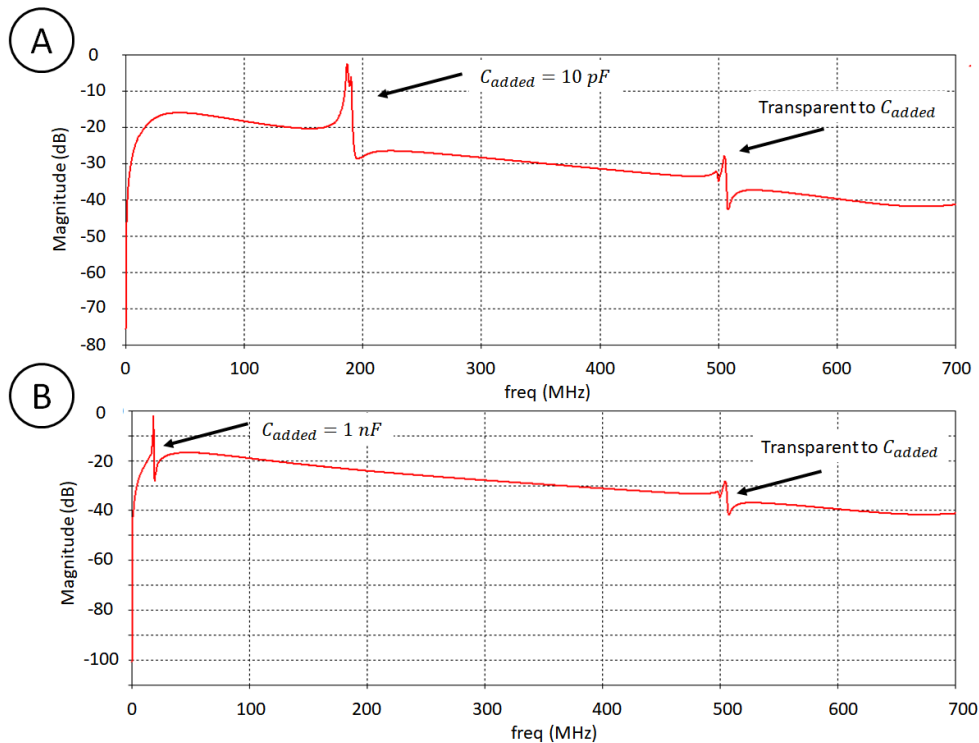


Figure 4.49: TL-mode gain regions cells with  $C_{added} = 10 \text{ pF}$  (a) and  $C_{added} = 1 \text{ nF}$  (b). Notice that the second resonance is not affected by  $C_{added}$

Finally, we proposed a 3x3 lattice made of TL-mode unit cells with  $C_{added} = 10 \text{ pF}$ , shown in Figure 4.50, in order to investigate how the magnetic flux is reflected by MTM and confined in between the TX and RX drivers. The simulated  $S_{21}$  response of the TX and RX coils assisted by this 3x3 MTM reflectors is highlighted in Figure 4.51, while Figure 4.52 shows the H-field at the MTM operating frequency  $195 \text{ MHz}$ . As it can be seen in Figure 4.52, the vortex-like behavior of the H-field on the MTMs' surfaces causes the magnetic flux to be reflected, like the ferromagnetic bars used in [79], meaning they could be replaced by TL-mode based MTM with the advantage of being planar (easy to integrate), low-cost (made of ordinary materials) and power efficient. Notice that gain resonance of the 3x3 MTM, at  $f_0 = 196 \text{ MHz}$ , is slightly different of a sole unit cell, at  $f_0 = 180 \text{ MHz}$ , due to the mutual coupling of the cells, as discussed in sections 4.1.3 and 4.1.4.

The results of this section were summarized in a conference paper accepted at the 11th International Conference on Metamaterials, Photonic Crystals and Plasmonics (Meta'20), postponed due to the outbreak of the COVID-19 pandemic. Because of that, these preliminary results will now be presented at Meta'21 to be held in Warsaw - Poland, in July 2021.

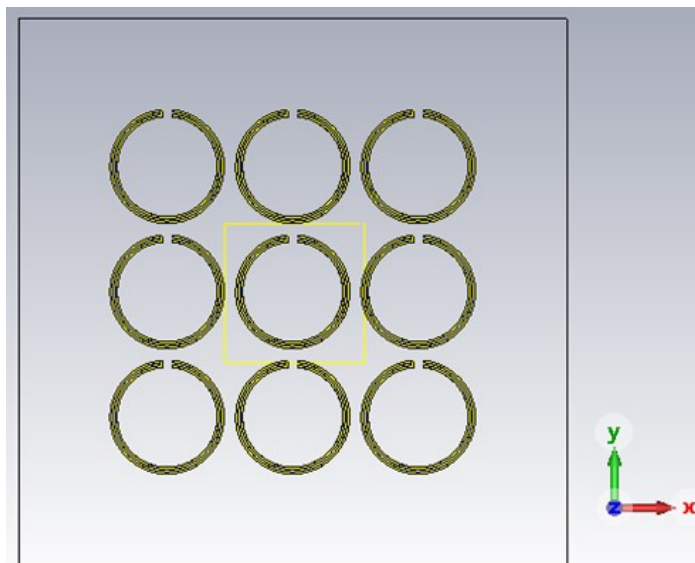


Figure 4.50: 3x3 MTM reflectors

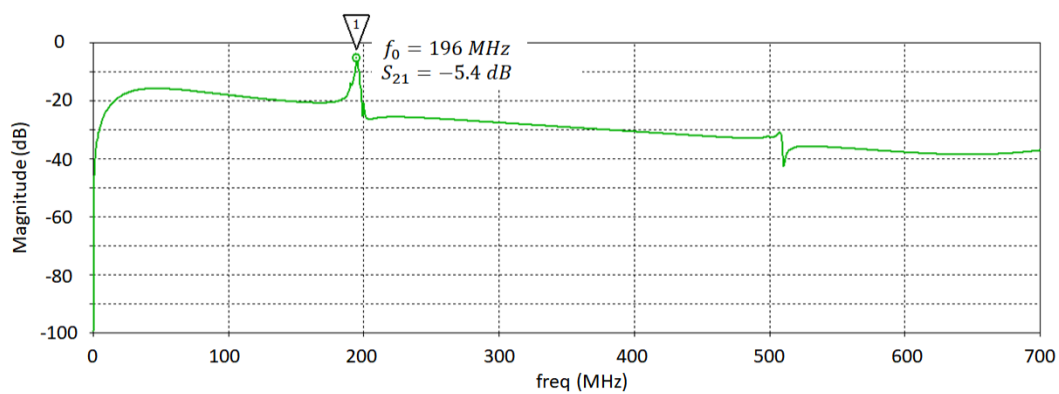


Figure 4.51: Transfer function of the TX and RX coils assisted by 3x3 MTM reflectors

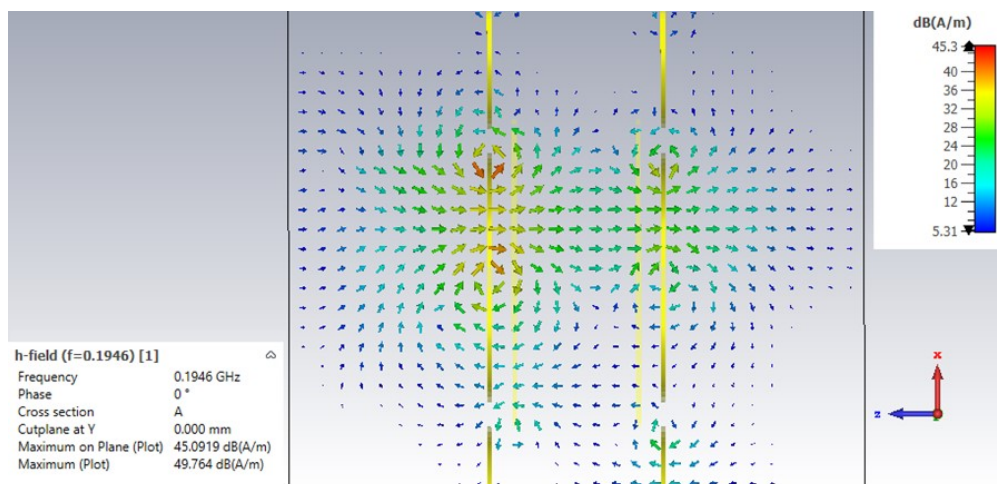


Figure 4.52: TX and RX coils assisted by 3x3 MTM reflectors. Notice that the vortex-like behavior around the MTM surface creates the apparent magnetic-flux reflection

## 4.4

### Final considerations

In this chapter, it was presented the design strategies of both MTM -based lenses and reflectors aiming at underwater applications. Considering the MNG lenses, it was shown that their SR-based unit-cell inductance should be maximized, since their circuits are characterized as RLC series. Therefore, DSSR unit-cells, with twice  $L_{cell}$  and 41% higher Q-factor, were proposed to enhance the MTM gain. It was shown that DSSR cells should be conceived as mirrored SRs to keep their electric currents with the same orientation on both planes of the MTM. Besides, there were presented DSSRs fine and coarse tuning mechanisms to ensure the precise control of the equivalent material response of the cell in the frequency domain. While the fine tuning is achieved by geometric optimization of the DSSR cell, the coarse tuning is realized inserting a SMD capacitor in series with the DSSR conductor.

Using a 2x2 lattice with coarse control, it was demonstrated that DSSR cells can operate in frequency ranges as low as hundreds of  $kHz$  with minimum degradation of their Q-factor and consequently their gain. Also, it was shown that although the MTM gain is insensitive to the medium dielectric constant when the system is aligned, it is affected by the high permittivity of water in misaligned scenarios, independently of the salinity level.

Moreover, it was shown that hybrid MTMs, conceived with different unit-cells, can be used to compensate the inherent losses of the MTM constituent materials (substrate and metallic surfaces), increasing the MTM gain up to 3  $dB$ . Even though, in literature [78], the optimum distribution of the equivalent  $\mu_r$  on the MTM surface has been described as  $\mu_r = 0$  at the central region and  $\mu_r < 0$  at the borders, the results obtained in this work suggest otherwise, the optimum distribution should be  $\mu_r < 0$  at the MTM central region and  $\mu_r = 0$  at the MTM borders. In any case, further investigations must be conducted to demonstrate it experimentally.

Considering the TX and RX coils insulation, it was shown that, when the drivers are insulated, IPT systems are almost insensitive to the medium conductivity at low frequencies. Also, it was shown that if the medium and the insulation slab have the same dielectric constant, a high-dielectric gain, due to improved impedance matching between materials, can be realized in certain

frequency ranges, except in frequencies that support propagating modes at the insulation-seawater interface.

Finally, it was shown, for the first time, that TL-mode coils can be effectively used as the unit cells of MTM-based magnetic reflectors. The response of the proposed TL-mode cell, differently of DSSR cells, must be controlled with the insertion of a parallel coarse tuning element. They are naturally dual band, but its second operating band presents low gain and cannot be controlled with the proposed coarse tuning mechanism. Further studies should investigate mechanisms for equalize the TL-mode cell gain in both bands and how to control them.

One important observation made in this chapter was the fact, usually neglected in literature, that the resonance frequency  $f_R$  of the unit-cell differs from the MTM operating frequency  $f_0$ , that is the frequency at which the maximum MTM gain is obtained.

## 5

### Modulation scheme for efficient MTM-assisted SIDPT

#### 5.1

##### Evaluation using phase modulation

Since IPT transmitters demand input signals with constant envelope for high-efficient DC-RF power conversion [80], most IPT architectures are based on phase or frequency modulation schemes. In this section, the effects of phase modulation on MTM-assisted IPT systems are investigated. The following results were obtained using the signal processing library of ADS (see Figure 5.1). The considered modulation schemes were the binary phase shift keying (BPSK) and the quadrature phase shift keying (QPSK) since their implementation is simple and cost-effective. Also, as it is well-known in digital modulation theory [81], BPSK and QPSK have the same performance in terms of bit error rate (BER) and error vector magnitude (EVM). For the simulations presented in this section, it was considered the same system configuration P1 employed in section 4.1.5.

Figures 5.2 to 5.5 show the BPSK symbol constellation for different data bandwidth (BW). To facilitate the comparison independently of the channel attenuation and the chosen frequency range, both input and output data are presented normalized by their maximum magnitude. Also, BW was normalized by the operating frequency  $f_0$ , being presented in terms of its occupied fractional bandwidth (FBW):

$$FBW = 100 \frac{BW}{f_0} \quad [\%] \quad (49)$$

Considering FBW values, the simulated BPSK constellation diagrams are shown in Figure 5.2 (in air without MTM), Figure 5.3 (in air with one MTM slab), Figure 5.4 (in freshwater with one MTM slab) and Figure 5.5 (in seawater with one MTM slab).

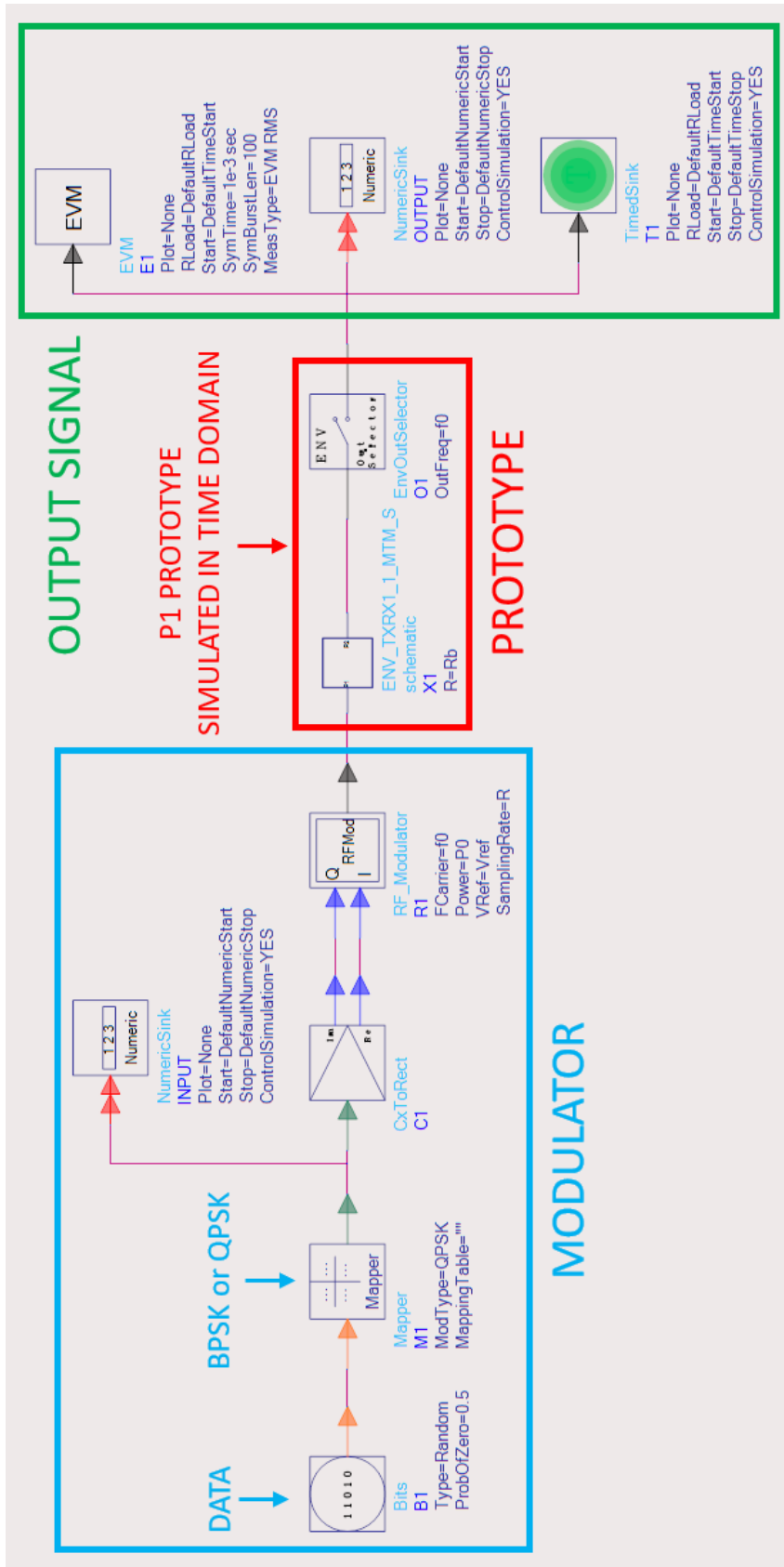


Figure 5.1: Data flow cosimulation on ADS for BPSK and QPSK

As shown in Figure 5.2, when data is transmitted between two coupled coils in air, with no MTM slab in the link using BPSK, the only distortion imposed by the system is to phase shift the output data by  $90^\circ$  regarding the input data, which can be easily explained by the fact that the voltage induced in the RX coils is phase-shifted by the displacement current  $I_{m,d}$ , due to its reactive nature:

$$V_{RX} = I_{m,d}Z_{RX} = j\omega\phi_m Z_{RX} \quad [V] \quad (50)$$

where  $\phi_m$  is the magnetic flux, and  $V_{RX}$  and  $Z_{RX}$  are the RX-coil induced voltage and impedance, respectively.

As shown in Figure 5.3, if a MTM is inserted in the link, this phase shift between the input and output symbols is reduced for about  $40^\circ$ . According to the analytical results obtained in section 3.3 using VMGTL theory, if a MTM slab is presented in the link, the primary power transfer mechanism is not the magnetic coupling anymore, but travelling magnetic waves. Since the phase gain of the travelling magnetic modes depends of  $\beta$  and  $\beta < 0$ , the total phase gain of the symbols is reduced due to the interaction with the MTM slab. Once more, the VMGTL analogy demonstrate to be a powerful mechanism to explain in simple terms the side effects of MTM-assisted IPT systems. The reduction of the phase shift between input and output data is basically the same independently of the surrounding media, as shown in Figures 5.3 to 5.5.

By comparing the results presented in Figure 5.2 (without MTM) with the other simulated results shown in Figures 5.3 to 5.5 (with MTMs in the link), we notice that the main drawback of the MTM to data transmission using BPSK is the fact that the lattice gain causes the BPSK constellation diagram to multiply its symbols by a factor that increases with the size of the array. In fact, this phenomenon is highly deleterious to the data transmission performance.

x Input symbols    x Output symbols

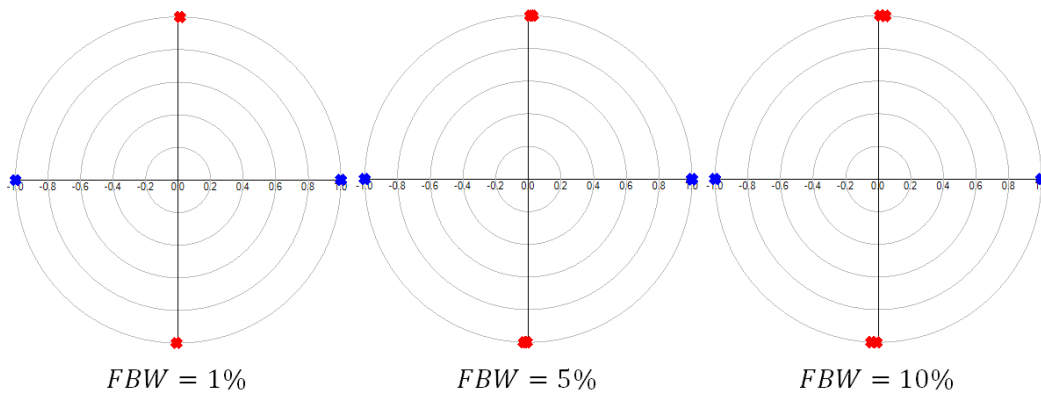


Figure 5.2: BPSK constellation diagram in air without MTM for  $FBW$  values. Notice that input and output symbols are phase-shifted by  $90^\circ$ , as expected by Eq. (50)

x Input symbols    x Output symbols

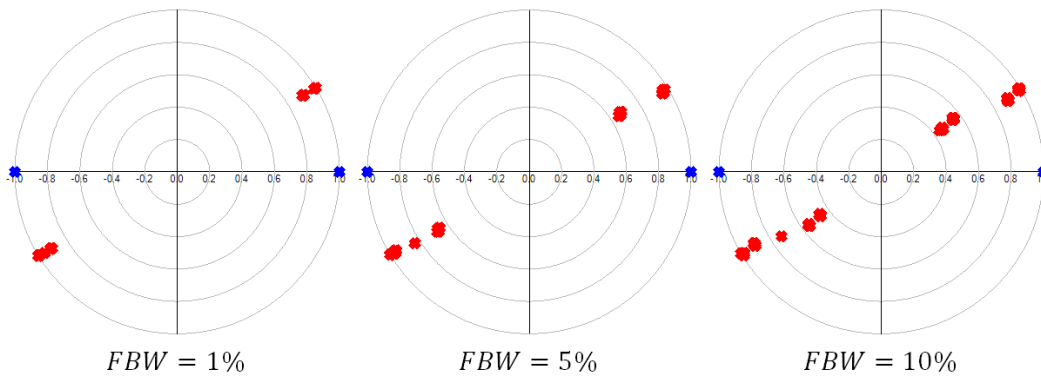


Figure 5.3: BPSK constellation diagram in air with one MTM slab for  $FBW$  values. Notice that the MTM slab changes the phase relationship between the input and output symbols for less than  $90^\circ$ . Besides, copies of the output symbols are generated by the MTM

x Input symbols    x Output symbols

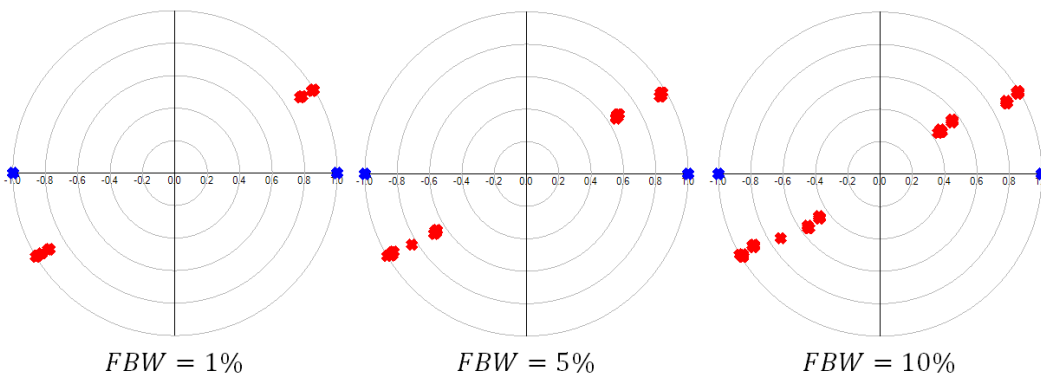


Figure 5.4: BPSK constellation diagram in freshwater with one MTM slab for  $FBW$  values. Notice that the results for air and freshwater are the same

x Input symbols    x Output symbols

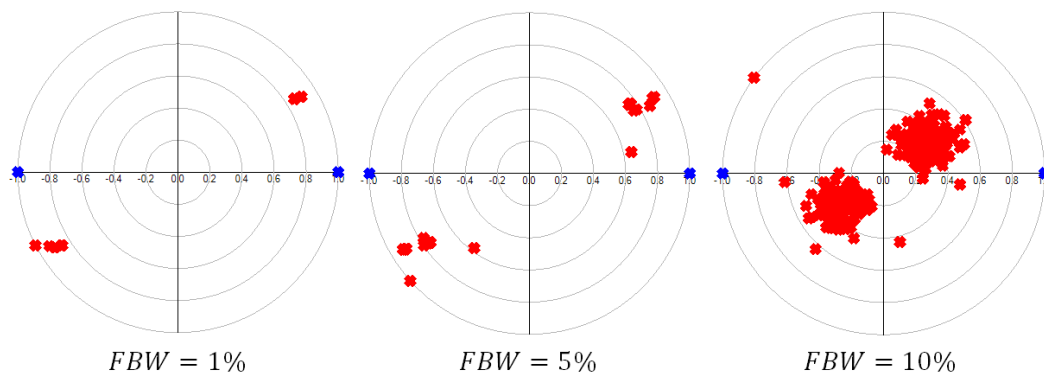


Figure 5.5: BPSK constellation diagram in seawater with one MTM slab for  $FBW$  values. Notice that the seawater losses reduce that MTM-induced repetition of the symbols due to the reduction of the MTM gain

Figure 5.6 shows the error vector magnitude (EVM) of the MTM-assisted SIDPT in air, freshwater and seawater, compared with the system without MTM in air, using BPSK modulation. As shown in Figure 5.6, when assisted by MTM, the EVM is much higher, independently of the medium. Notice that in seawater, the EVM, although still high, is smaller than in air and freshwater due to a reduced Q-factor of the MTM cells, and consequently, a reduced MTM gain.

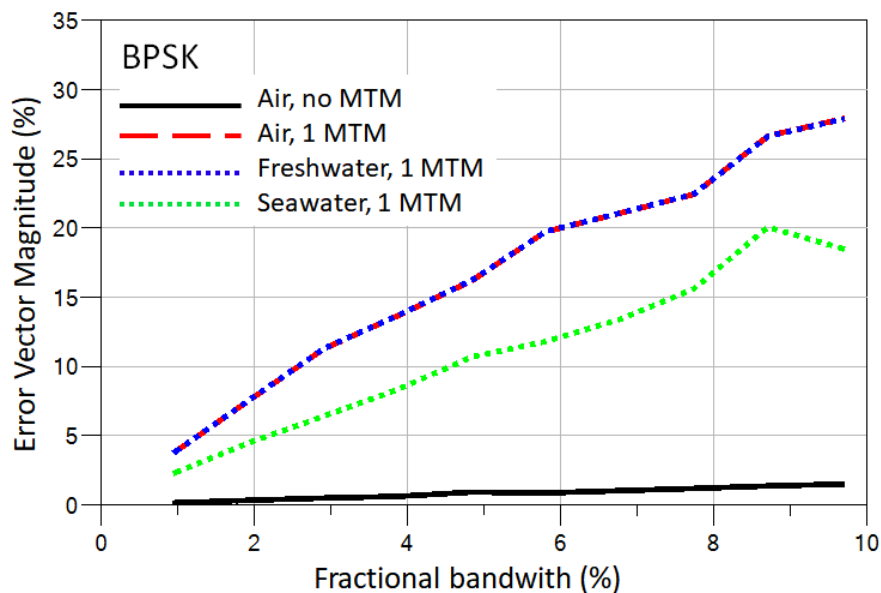


Figure 5.6: EVM of the MTM-assisted IPT in air (red dash), in freshwater (blue dot) and seawater (green dot) compared with the IPT system without MTM in air (solid black) using BPSK modulation

In turn, Figures 5.7 to 5.10 show the QPSK symbol constellation, for different FBW. The simulated QPSK constellation diagrams are shown in Figure 5.7 (in air without MTM), Figure 5.8 (in air with one MTM slab), Figure 5.9 (in freshwater with one MTM slab) and Figure 5.10 (in seawater with one MTM slab). Furthermore, Figure 5.11 shows the error vector magnitude (EVM) of the MTM-assisted SIPDT in air, freshwater and seawater, compared with the system in air without MTM, using QPSK modulation.

As expected, since the performance of QPSK and BPSK are equivalent (QPSK is essentially two BPSK implemented in quadrature), the results using QPSK are the same obtained with BPSK in terms of EVM, as it can be seen by comparing Figure 5.11 with Figure 5.6. One important remark concerning QPSK is that the input and output symbols in the constellation diagram, shown in Figure 5.7, are also phase-shifted by  $90^\circ$ . Nonetheless, due to the symmetry of QPSK diagram, it cannot be easily noticed like in the BPSK one.

Since the reduction of the MTM Q-factor was positive for phase-modulated data transmission although deleterious for power transfer, one possible strategy aiming the performance enhancement of data transmission would be to conceive MTMs with reconfigurable Q-factor. If more efficiency is required,  $Q$  is enhanced, otherwise it is reduced to minimize MTM-induced distortions. However, this sort of mechanism for varying  $Q$  keeping  $f_0$  constant would be too complex, as well as expensive in terms of the system overall power consumption.

Finally, considering the results presented in Figure 5.6 and Figure 5.11, it can be said that the maximum FBW (assuming an EVM tolerance of 5%) in MTM-assisted SIPDT, using either BPSK or QPSK, is about 1% in air and freshwater, and 2% in seawater. Usually, UWSN applications demand a bandwidth of the order of tens of kHz. This means that BPSK/QPSK modulation scheme could only be applied effectively for operating frequencies  $f_0 > 1 \text{ MHz}$ .

x Input symbols    x Output symbols

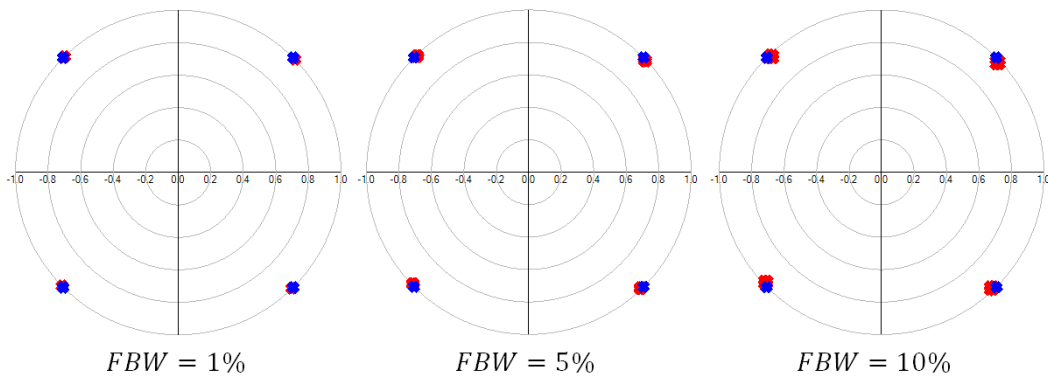


Figure 5.7: QPSK constellation diagram in air without MTM for  $FBW$  values. Notice that the output symbols are also rotated in  $90^\circ$  in relation to the input ones although it is disguised by the symmetry of the QPSK constellation

x Input symbols    x Output symbols

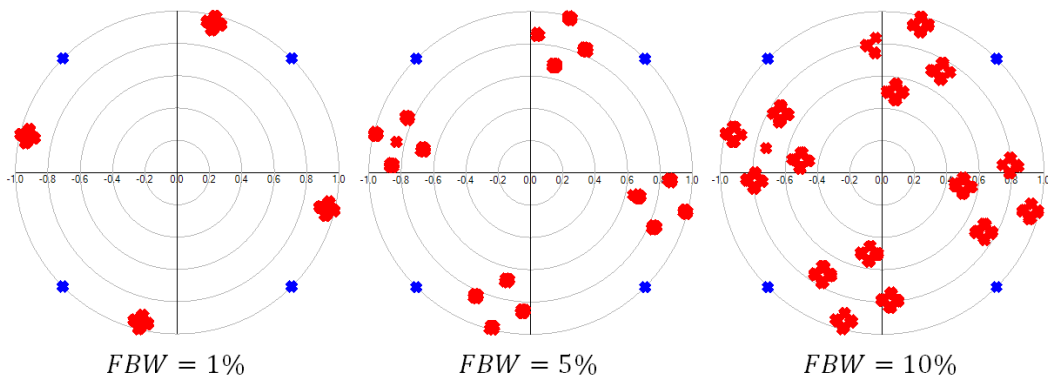


Figure 5.8: QPSK constellation diagram in air with one MTM slab for  $FBW$  values. Notice that the QPSK symbols are repeated by the MTM lattice

x Input symbols    x Output symbols

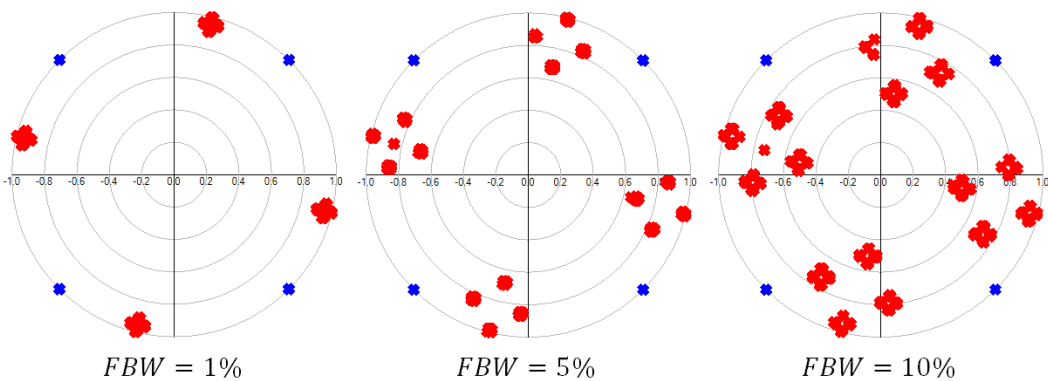


Figure 5.9: QPSK constellation diagram in freshwater with one MTM slab for  $FBW$  values. Notice that the results in air and freshwater are the same

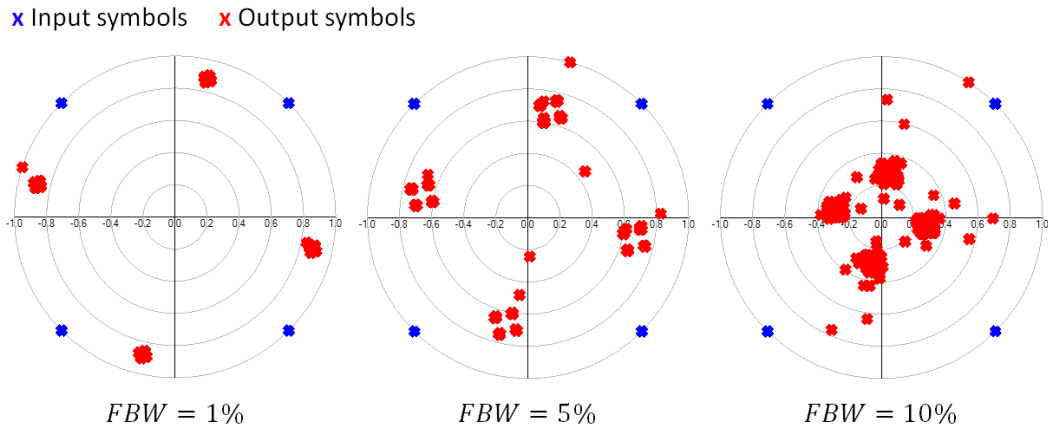


Figure 5.10: QPSK constellation diagram in seawater with one MTM slab for  $FBW$  values

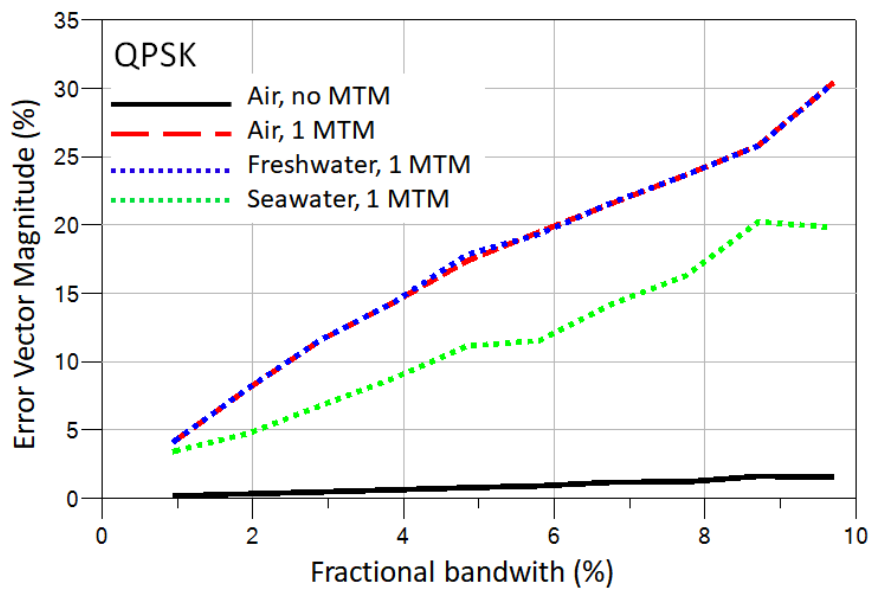


Figure 5.11: EVM of the MTM-assisted IPT in air (red dash), freshwater (blue dot) and seawater (green dot), compared with the IPT system without MTM in air (solid black) using QPSK modulation

## 5.2

### Evaluation using frequency modulation

#### 5.2.1

#### Comparison between FSK and PSK

Beside the drawbacks in terms of MTM-induced symbol multiplication, which highly degrades the system's EVM, phase modulation such as BPSK and QPSK suffer from envelope amplitude fluctuations caused by phase discontinuities during symbol transition, as shown in Figure 5.12. Usually, this amplitude modulation of the signal's envelope imposes losses to the TX-coil PA blocks. Hence, based on that and on the arguments presented in section 5.1, directly modulate the data via frequency shifting key (FSK) seems to be a better option, as it has also been stated in [82], although they have not considered the particular case of MTM-assisted IPT systems.

In fact, considering the results presented in section 3.4.3, it seems natural that MTM-assisted IPT systems should be based on FSK since MNG MTM are 1) narrowband in nature and 2) can be made multi-band by using slabs tuned to different  $f_0$ .

As shown in Figure 5.13, FSK spectrum is composed of a set of narrowband channels, while PSK or amplitude modulation, like the Amplitude Shift Keying (ASK), have a continuous, compact spectra. Consequently, the MTM gain and the BW, in PSK and ASK, are limited by a fundamental trade-off related to  $Q$ . While MTM gain is directly proportional to  $Q$ , as discussed in section 3.4.1, BW is inversely proportional, as it can be deduced from:

$$Q = \frac{f_0}{BW} \quad (51)$$

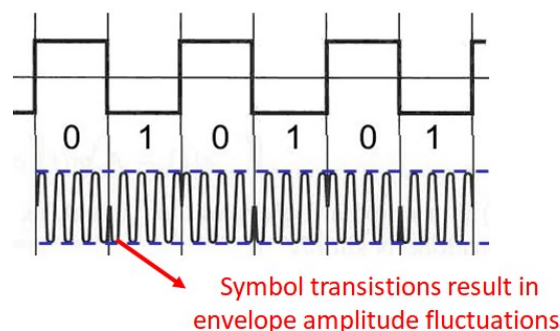


Figure 5.12: Amplitude fluctuations due to fast phase shifts during symbol transitions

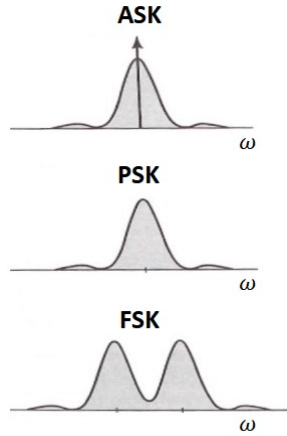


Figure 5.13: Comparison between typical (a) ASK, (b) PSK and (c) FSK spectra

On the other hand, since FSK symbols are represented by individual channels, the trade-off described by Eq. (51) does not apply, which facilitates the integration of this sort of modulation with IPT systems assisted by MTM lenses and/or reflectors. However, in FSK, the large frequency variation of the system imposes another limitation given by the time delay  $t_d$  of the TX and RX drivers as well as of the MTM unit cells. As discussed in section 2.2.4, the symbol period  $T_s$  and, consequently, the symbol rate  $R_s$ , are limited by Eq. (14). Assuming a PP compensation topology for minimum  $t_d$  at the TX and RX drivers, the system's  $t_d$  will be limited by the MTM's  $t_d$ . Knowing that  $t_{d_p} \approx 8RC$ ,  $t_{d_s} \approx 8\frac{L}{R}$ ,  $Q_s = \frac{1}{R}\sqrt{\frac{L}{C}}$  and  $Q_p = R\sqrt{\frac{C}{L}}$  are, respectively, the RLC-series time delay, the RLC-parallel time delay, the RLC-series Q-factor and RLC-parallel Q-factor, it can be deduced that:

$$Q_s = \frac{t_{d_s}}{8\sqrt{LC}} = \frac{t_{d_s}\omega_0}{8} \quad (52)$$

$$Q_p = \frac{t_{d_p}}{8\sqrt{LC}} = \frac{t_{d_p}\omega_0}{8} \quad (53)$$

Eqs. (52) and (53) represent the fundamental trade-offs for RLC-series and RLC-parallel MTM cells, when transmitting FSK-modulated signals. In both cases, in order to minimize  $t_d$  keeping  $Q$  high,  $\omega_0$  must be maximized. Consequently, FSK cannot be used efficiently in the proposed MTM-assisted IPT at low-frequency ranges. Note that the same result is valid for RMC topologies, since strong coupling regime is equivalent to a single-cell MTM.

Based on the classic results presented in [83] and shown in Figure 5.14, where the normalized bit rate of the system is plotted as a function of normalized bit energy using different modulation schemes, for  $BER = 10^{-5}$ , FSK can also be

characterized as presenting 1) high power efficiency and 2) extremely low bandwidth efficiency. Since UWSN / IoUT applications are power limited and not bandwidth limited (i.e., as in mobile communication), the employed modulation scheme must be chosen aiming at minimum power consumption, particularly in the UD transceiver. However, FSK only outstands PSK performance in terms of bit power efficiency when the number of symbols  $M > 4$ . Despite that, it is important to highlight that this consideration on FSK/PSK power efficiency considers only the required energy per bit for efficient communication. It does not include the power required by the RX detection system to process the incoming data, which is higher in any PSK since it demands a more complex architecture being a coherent modulation scheme.

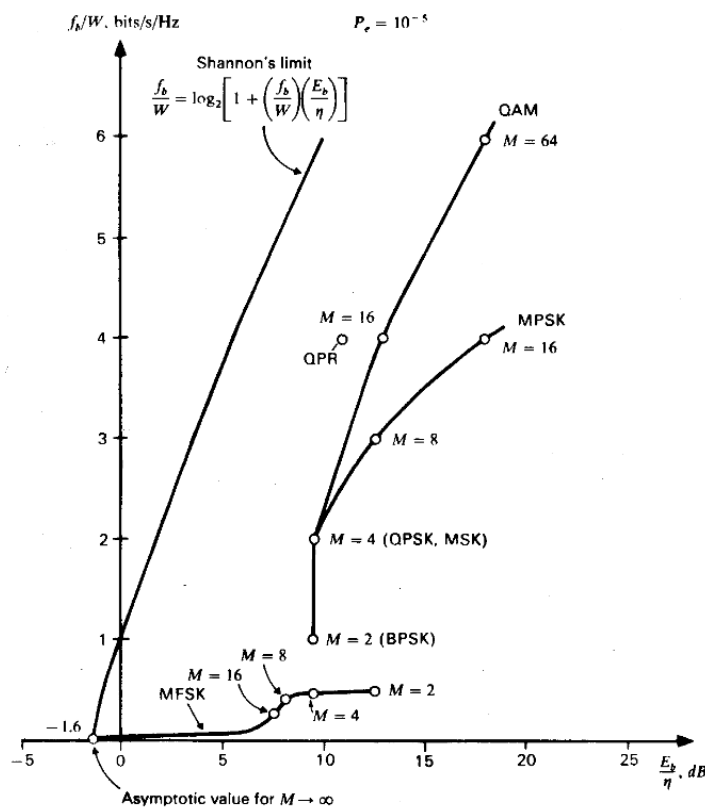


Figure 5.14: Normalized bit rate as a function of the normalized bit energy using different modulation schemes, for  $BER = 10^{-5}$  [83]. Notice that FSK only outstands bit power efficiency of PSK systems when the number of symbols  $M > 4$

Coherent detection architectures (BPSK, QPSK and coherent FSK) have a better bandwidth efficiency in comparison with the incoherent ones (ASK and non-coherent FSK), since coherence detection minimizes spectrum spreading effects on the incoming signal, but they consume much more power for the same BER, due to the fact they require local oscillators at the RX. That is why low-power consuming UWSNs typically employ non-coherent demodulation. Another typical advantage of coherent detection is to be more robust over fading channels due to multipath. Nonetheless, near-field communication are not affected by multipath-related problems.

## 5.2.2

### Optimum frequency range for FSK

Although authors in [48-50] have concluded that high-efficient IPT systems in seawater can only operate in frequency ranges lower than a few hundred *kHz*, it is important to remark that they are trying to transmit power over distances much longer than the diameter of the coils. Assuming that the UWSN will be assisted by UDs, capable of travelling to the vicinity of the BS and the sensor field, power and data transmission can be assumed to occur in short distances, at both sides of the link. It means that the operating frequency could be increased, at some extent, without imposing too much additional losses to the system.

But how high could the operating frequency be? This question can be answered by defining a normalized skin depth  $\delta_n$ :

$$\delta_n = \frac{1}{D} \sqrt{\frac{2}{\omega \mu_0 \sigma}} \quad (54)$$

where  $D$  is the separation distance between the drivers and  $\sigma$  is the medium conductivity.

Figure 5.15 shows a comparison between the transfer function in air and seawater for air-insulated coils with  $D = r$  and  $D = 2r$ , where  $r$  is the TX and RX coils' radius. On the other hand, Figure 5.16 shows the normalized skin depth  $\delta_n$  as a function of frequency for  $D = r$ , while Figure 5.17 show the divergence between a 2-coil IPT system in air and seawater (or any conductive medium), as a function of frequency and  $\sigma$ .

As shown in Figure 5.15, if the magnitude of  $\kappa_m$  is strong  $D < r$ , the system is insensitive to seawater's high dielectric constant. However, for  $D > r$ , high-dielectric effects start to be perceived by the system. For the limiting case  $D = r$ ,

the system is insensitive to  $\sigma$  for most frequencies in the purely reactive region, discussed in section 3.5.1 (see Figure 3.16). As shown in Figure 5.16 and Figure 5.17, the maximum medium insensitivity frequency is achieved at  $\delta_n = 1$ .

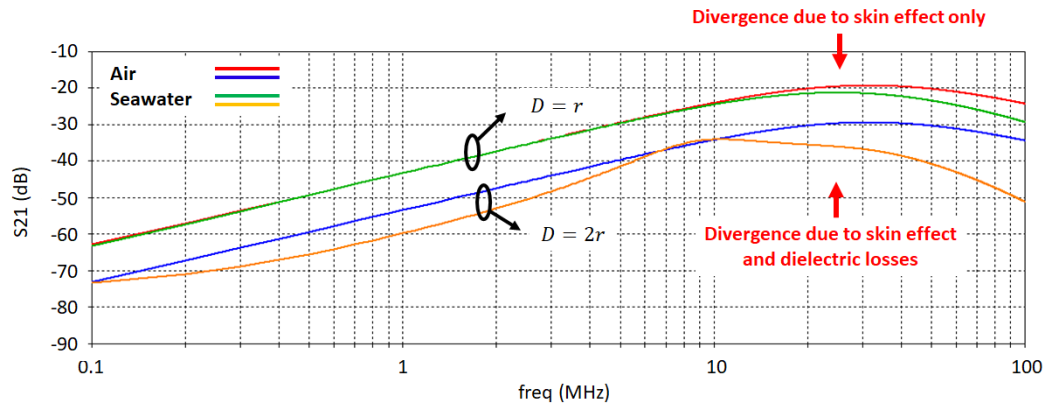


Figure 5.15: Comparison between the transfer functions of the 2-coil IPT system, in air and seawater ( $\sigma = 5 \text{ S/m}$ ), for separation distance  $D = r$  and  $D = 2r$

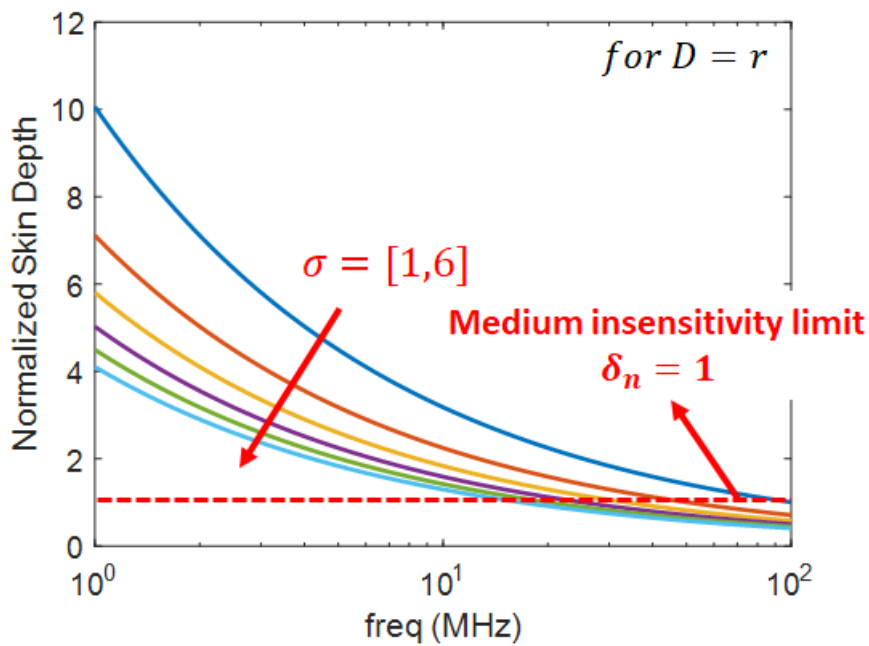


Figure 5.16: Normalized skin depth  $\delta_n$  as a function of frequency, for  $\sigma$  varying from 1 to 6  $\text{S/m}$ , in steps of 1  $\text{S/m}$ , and  $D = r$

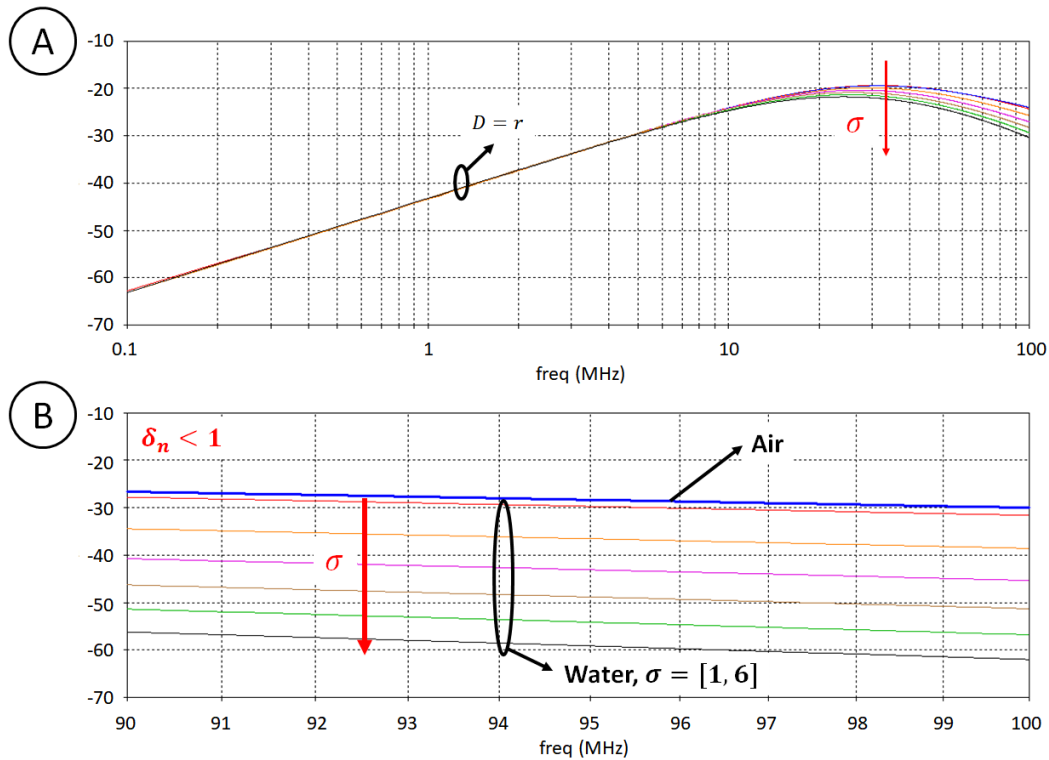


Figure 5.17: Transfer function divergence between a 2-coil IPT system in air and seawater as a function of frequency, for  $\sigma$  varying from 1 to 6 S/m, in steps of 1 S/m, and  $D = r$ . The results are presented in a frequency range (a) from 0.1 MHz to 100 MHz and (b) zoomed in the frequency range where all curves present  $\delta_n < 1$

Figure 5.18 shows the maximum insensitivity range for  $\delta_n = 1$  as a function of  $\sigma$ , while Figure 5.19 shows the loss of the 2-coil IPT system in comparison with the air-medium case if  $\delta_n < 1$  as a function of  $\sigma$ . The results shown in Figure 5.18 are deduced from Figure 5.17.(a). On the other hand, the results shown in Figure 5.19 are deduced from Figure 5.17.(b).

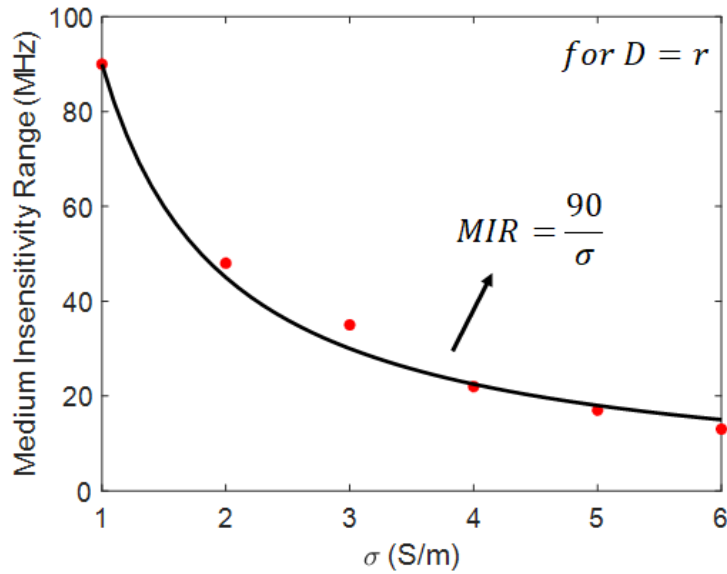


Figure 5.18: 2-coil IPT system insensitivity range to the medium properties, for  $D = r$

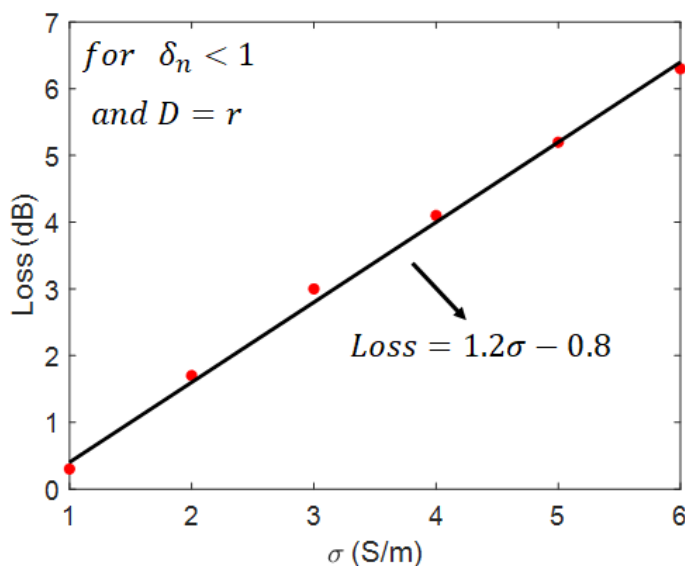


Figure 5.19: 2-coil IPT system loss in seawater in comparison with air-medium case, for  $\sigma$  varying from 1 to 6 S/m, in steps of 1 S/m, and  $D = r$ . Notice that after the frequency range achieves  $\delta_n < 1$  the relative loss varies linearly with  $\sigma$

Assuming that relative loss to the air-case is intended and considering the results presented in Figures 5.18 and 5.19, it can be said that the FSK could be used in MTM-assisted SIDPT systems, employing UDs for frequencies up to 10 MHz, if the separation distance between the UD and its BS or the UDs and the sensor field is smaller than the UD transceiver radius. Notice that this result assumes that the system will be excited by FSK narrowband signals (almost discrete channels) and not signals with a compact, continuous bandwidth such as

PSK or ASK. If low medium losses are tolerated, that range could be increased to up 20 MHz.

Finally, the magneto-inductive factor of two 2-coil IPT system, defined as the product of the magnetic flux  $\phi_m$  and the input current  $I_{IN}$ , is investigated in order to determine the optimum frequency range. Based on the results presented in section 3.2.1 and Eq. (31), and knowing that  $V_m(at TX) = I_{IN}$ , the magneto-inductive factor can be shown to be given by:

$$|\phi_m I_{IN}| = \frac{P_{IN}}{\omega} \quad [J] \quad (55)$$

Notice that magneto-inductive factor is a measure of system's energy utilization. As shown in Figure 5.20, for a fixed  $P_{IN} = 1 W$  delivered to the TX coil, the total energy required by the system to generate the same 1-watt of useful power is much higher for low frequencies. This is the reason, for example, no power can be transmitted by means of inductive coupling in extremely low frequencies, since the total energy required by the system would tend to infinity. In this way, if FSK is employed as the modulation scheme of SIDPT systems, symbols should have ideally similar magneto-inductive factors, otherwise  $I_{IN}$  will vary too much in amplitude for different transmitted symbols. Based on the curve shown in Figure 5.20, the most energy-effective range would be above  $f_0 = 1 MHz$ .

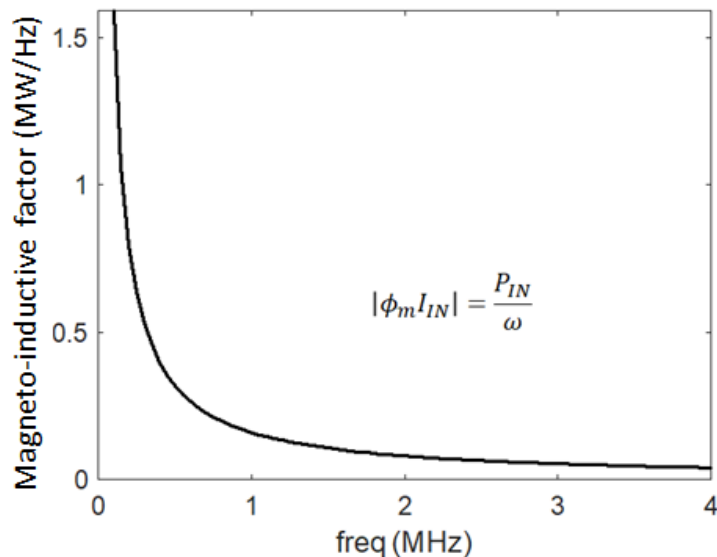


Figure 5.20: Magneto-inductive factor as a function of frequency, for  $P_{IN} = 1 W$

### 5.2.3

#### Dual-band MTM-assisted SIPDT

In order to employ a 2-FSK in MTM-assisted SIPDT, the net MTM gain should be the same for both symbols, otherwise the incoming data will be distorted in amplitude. Figure 5.21 shows the two proposed strategies to combine the gains of two different MTMs set to different operating frequencies: 1) prototype D1 (Figure 5.21.(a)), where two MNG MTM lenses are set to two different frequencies,  $f_1$  and  $f_2$ , and 2) prototype D2 (Figure 5.21.(b)), where the TX and RX coils are assisted by two MTM reflectors set to  $f_1$  and one MTM lens set to  $f_2$ . In D1, for optimum bandwidth with equivalent gain, the lenses employ DSSR cells, with coarse tuning elements  $C_{SMD1}^{D1} = 2.37 \text{ nF}$  and  $C_{SMD2}^{D1} = 0.19 \text{ nF}$ , for symbols  $f_1$  and  $f_2$ , respectively. On the other hand, in D2, the optimum bandwidth is obtained with reflectors employing a TL-mode unit cell, with  $C_{SMD1}^{D2} = 1.72 \text{ nF}$ , for  $f_1$ , and a lens with  $C_{SMD2}^{D2} = 0.465 \text{ nF}$ , for  $f_2$ .

Figures 5.22 and 5.23 show the results for D1 and D2, compared with the equivalent one-band cases, obtained when one of the coarse tuning elements,  $C_{SMD1}$  or  $C_{SMD2}$ , is null. In this way, in order to obtain two equal-gain bands, D1 frequency deviation between both symbols must occupy a minimum bandwidth  $BW = 15 \text{ MHz} = 3f_1$ , while D2 occupies only  $BW = 2.2 \text{ MHz} = 0.23f_1$ . As discussed in section 3.4.3, the strong anti-resonance response of the MNG MTM after its gain region makes difficult to set two lenses to operate in different, adjacent channels. Hence, it can be concluded that for unit cells of similar size and shape, the combination of reflectors and lens is a better option in terms of spectrum efficiency.

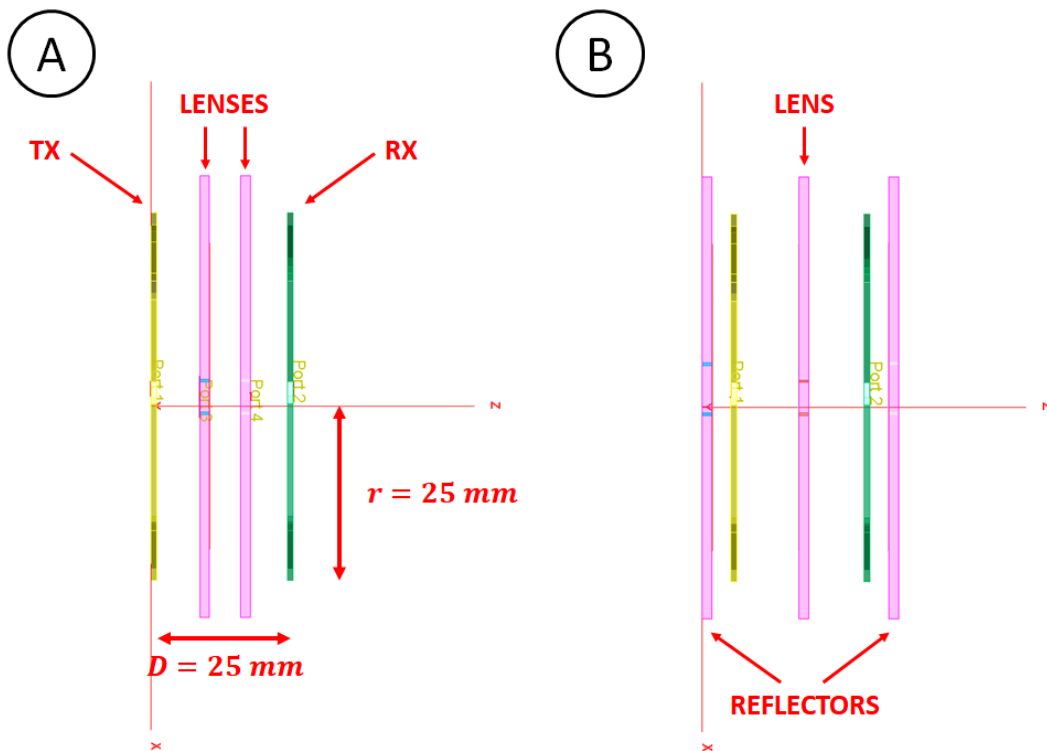


Figure 5.21: Proposed dual-band strategies using (a) two MTM lenses and (b) one MTM lens and two reflectors

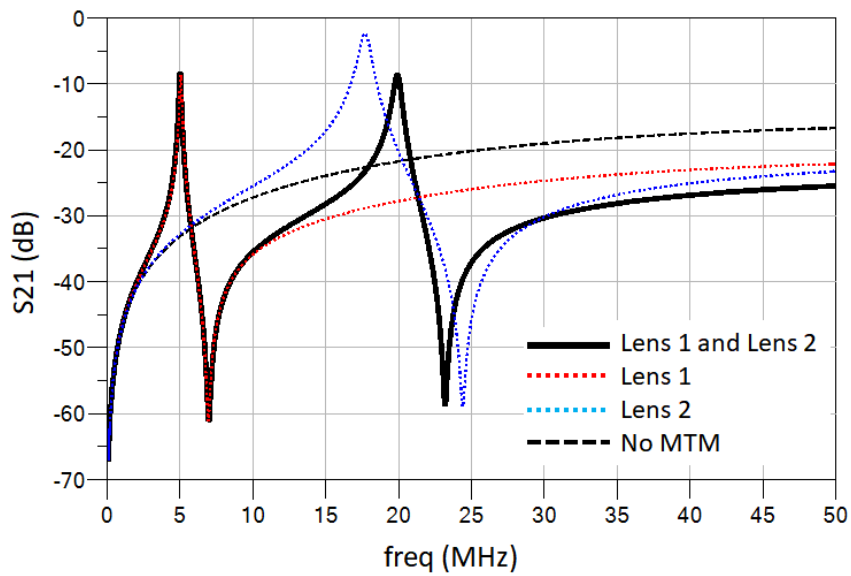


Figure 5.22: Transfer function of the system using two MTM lenses with different  $f_0$  with optimal frequency deviation for maximum dual-band gain

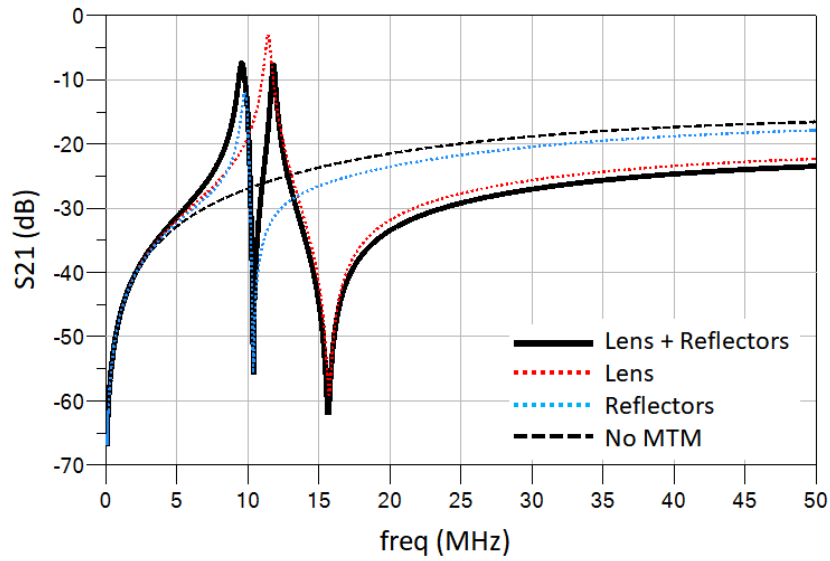


Figure 5.23: Transfer function of the system using a combination of one MTM and two MTM reflectors

In order to illustrate that point, let us consider a different D1 configuration, with  $C_{SMD2}^{D1} = 0.7 \text{ pF}$ . The increasing of  $C_{SMD2}^{D1}$  reduces  $f_2$ , as shown in Figure 5.24. Note that, when the frequency deviation between  $f_1$  and  $f_2$  becomes smaller than  $15 \text{ MHz}$  in D1, it forces the gain region of  $f_2$  into the anti-resonance of gain region  $f_1$ , which attenuates the magnitude of gain region of  $f_2$ .

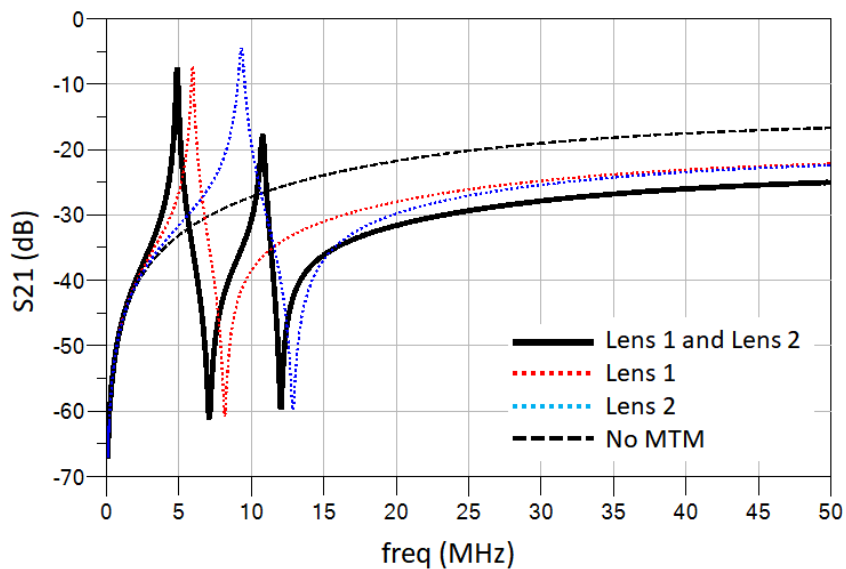


Figure 5.24: Transfer function of the system using two MTM lenses with different  $f_0$  with sub-optimal frequency deviation

### 5.2.4

#### Maximum data rate of MTM-assisted SIPDT using FSK

Let us consider the prototypes D1 and D2 presented in section 5.2.3, assuming a PP compensation topology for the TX and RX coils. Replacing Eqs. (14) and (15) into Eqs. (52) and (53), the maximum symbol rate  $R_s$  achievable by any MTM (lenses or reflectors) is:

$$R_s = \frac{\omega_0}{16Q_{cell}} = \frac{\pi f_0}{8Q_{cell}} \quad (56)$$

In multi-band MTM-assisted SIPDT systems, the FSK symbol with the smaller  $R_s$  limits the system data rate. In Table 2, the maximum data rates achievable by the prototypes D1 and D2 are compared. D1 data rate is limited by  $R_{s1}$ , while D2 data rate is limited by  $R_{s2}$ . As it can be seen, while the maximum D1 data rate is 59 *kbps*, D2 can achieve 102 *kbps*. In this way, D2 not only has a better bandwidth efficiency regarding D1, but also offers a higher data rate. Since most conventional UWSN data rate varies from 5 up to 20 *kbps*, the obtained data rate using MTMs is 5 times higher than the current topologies being employed.

Table 2: Comparison between the data rates of the MTMs

Prototype	$f_{01}$ (MHz)	$Q_1$	$R_{s1}$ (kbps)	$f_{02}$ (MHz)	$Q_2$	$R_{s2}$ (kbps)
D1	5	33	59	20	35	225
D2	9.5	20	186	12	46	102

### 5.3

#### Final considerations

In this chapter, phase and frequency modulation scheme were investigated considering MTM-assisted SIDPT applications for UWSN since they dissipate less power at the PA blocks. Considering PSK modulation, it has been shown that the optimum operating bandwidth is limited to  $FBW < 2\%$  in seawater and  $FBW < 1\%$  in air and freshwater for both BPSK and QPSK, due to the distortion caused by the MTM-induced symbol pattern multiplication. Hence, effective PSK-based UWSN would demand  $f_0 > 1$  MHz for bandwidths in the order of tens of kHz.

Considering FSK, it has the advantage of being a multiband modulation scheme instead of a compact band one, such as PSK or ASK. Nonetheless, just like PSK, it demands high operating frequencies  $f_0$ , due to the fundamental trade-

off between the high  $Q$  and low  $t_d$ . Since FSK symbols are orthogonal bands, the number of symbols is limited by 1) the number of operating bands of the MTM slabs and 2) the maximum  $f_0$  insensitive to medium losses (conductivity and dielectric losses). As it has been shown, IPT systems are medium insensitive if  $\delta_n > 1$  and  $D \leq r$ . In these conditions, FSK could be used in MTM-assisted SIDPT systems for frequencies up to 10 MHz. If low medium losses are tolerated, that range could be increased up to 20 MHz. In order to limit the input current variation when transmitting different FSK symbols,  $|\phi_m I_{IN}|$  must be slow varying with frequency over the chosen operating range. This means that for FSK, the minimum operating frequency is  $f_0 > 1$  MHz.

Although in general FSK-based MTM-assisted SIDPT operates with higher  $f_0$  and occupies a larger bandwidth than PSK ones, the fact that it does not require a coherent demodulation circuit at the SN level makes FSK easier and cheaper.

Finally, two basic strategies for multi-band MTM-assisted SIDPT systems were compared: 1) using two lenses with different  $f_0$  and 2) a combination of a lens with a pair of reflectors. Based on the obtained results, it can be said that the second strategy presents a better performance in terms of both total occupied bandwidth and maximum achievable data rate.

## 6

### Conclusion

#### 6.1

##### Final comments

Underwater exploration is the last frontier for the expansion of the global economy. Brazil and the State of Rio de Janeiro, due to their strategic location, natural characteristics and tradition on the development of underwater technologies, occupy a distinguished position and will both play a major role in the future Blue Economy in South Atlantic. This means that Brazilian and Fluminense societies and rulers should consider more seriously the development of high-tech industries connected with the exploration of deep-water environments, aiming to boost the economic development of Brazil, to reinforce the country's sovereignty over non-Brazilian interests, and to extend Brazilian influence, both regional and internationally. Since UWSNs are the foundation technology supporting any of these activities, this thesis focused on the development of reliable SIPDT using UDs and MTMs.

In summary, this work has shown, by means of analytical calculations based on VMGTL approach and numerical simulations on ADS and CST, that, if the IPT drivers are assumed insulated from their surroundings, there will be a region of medium insensitivity depending on both  $\delta_n > 1$  and  $D \leq r$  that can be exploited to effectively and efficiently implement SIDPT systems based on PSK or FSK. However, due to the simplicity of its receptor, which can employ noncoherent detection techniques, FSK is preferred over PSK for UWSN applications, since SNs are highly limited in terms of space and power. Concerning the assisting MTM slabs, it was shown that the multiband gain required for FSK implementation has an improved performance in terms of occupied bandwidth and data rate if a set of lenses and reflectors are employed.

## 6.2

### Contributions

The main contributions of this thesis to the UD-assisted UWSN using MTMs field were:

- The demonstration that MTM-assisted IPT systems benefits over conventional RMC topology using the strong coupling regime is due to a sort of array gain, emerging from the coupling of MI waves on the MTM surface, which behave as magnetic currents and supports source-free fields [61];
- The development of a new analytical model that keeps the physical meaning of the power transmission in-between two magnetically coupled systems [27-28];
- Based on the VMGTL approach, it was shown that the high-gain region of MTM lenses is not due to the enhancement of  $\kappa_m$  but to the rise of travelling magnetic modes characterized by  $\beta < 0$ . Also, it was shown, for the first time, that MTM lenses possess a minimum-distortion region characterized by a low  $\alpha$ ;
- The development of an extension to hybrid MTM theory, for improved MTM gain, suggesting that the optimum distribution of  $\mu_r$  could be a central region with  $\mu_r < 0$  and borders with  $\mu_r = 0$ ;
- The demonstration, by numerical simulation, of the advantages of high-dielectric insulation of the coils;
- The demonstration, by numerical simulation, that TL-mode coils can be used as artificial magnetic reflectors and that they are intrinsically dual band;
- The demonstration, by numerical simulation, that phase modulation schemes, such as BPSK and QPSK, are affected by the MI waves on the surface of the MTM, multiplying the symbol constellation pattern; and
- The demonstration, by numerical simulation, that combining MTM lens with MTM reflectors is more efficient for dual-band MTM-assisted SPIDT systems using FSK, in terms of total occupied bandwidth and data rate, than multiple lenses set to two different operating frequencies.

## 6.3

### Future work

The following works are proposed as a continuation of this thesis:

#### 6.3.1

##### Experimental verification of intermediary results

First, all the intermediary results of the present work, concerning the hybrid MTMs, TL-mode based MTM reflectors, high-dielectric insulation gain, data constellation pattern multiplication due to the interaction with the MTM lattice, and so on, must be experimentally proved, since so far the obtained results were based on numerical simulations and the proposed system is derived from these results.

Due to several incidents occurred during the realization of this thesis, including health problems of the original supervisor and the COVID-19 pandemic, most experimental tests could not be implemented. Nonetheless, as shown in Figure 6.1, the MTM lenses and reflectors investigated in this work have already been manufactured by a local PCB manufacturer from Rio de Janeiro City.

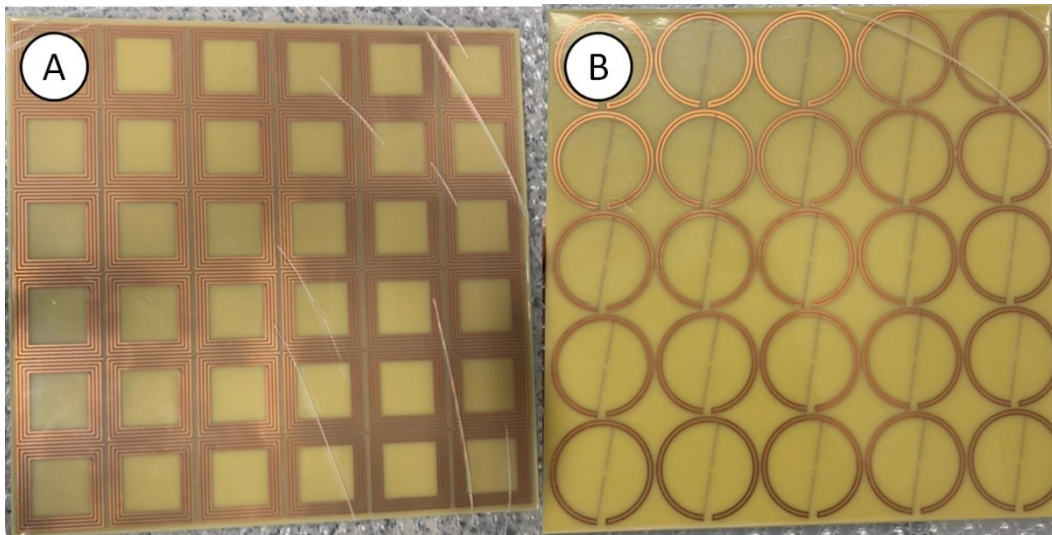


Figure 6.1: Manufactured MTM (a) lenses and (b) reflectors

### 6.3.2

#### Improvement of the VMGTL theory

The presented VMGTL theory must be adapted to include not only MTM lenses, but MTM reflectors as well. Besides, the proposed simplifying hypotheses validity were verified under specific conditions and then should be further verified, for example, with different geometries of TX and RX coils. Better estimation methods of the VMGTL parameters should also be considered in future researchers.

### 6.3.3

#### Diversity schemes and MIMO VMGTL

In the present work, it was only considered the single-input-single-output (SISO) scenario. To increase the efficiency and output power capacity of the system various diversity schemes should be simulated and verified. Particularly, further investigations should be conducted about the impact of diversity in transmission and reception (separately and combined) on the MTM gain and on modulation scheme (particularly FSK). Finally, the proposed VMGTL model must be adapted to include MIMO IPT.

### 6.3.4

#### Dual-band MTM unit-cells based on TL-modes

In the present work, MTM unit-cells based on the so-called TL modes were presented. Although the conducted studies indicate that they have high-gain regions, when employed as magnetic reflectors, further investigations should be performed to better understand their behavior. One extraordinary virtue of TL modes that must be pointed out is its dual-band characteristic, which could be most naturally used for efficient FSK-based data transmission. However, the control of the TL-mode unit cell second resonance must still be better investigated. Moreover, it would be of great interest to investigate the possibility of hybrid TL-mode based reflectors.

### 6.3.5

#### Implementation and experimental validation of the proposed system

As a mean to validate the analytical and numerical results, a small-scale UWSN must be implemented and tested in a controlled environment. Besides, the signal and power integrity of the SIPDT system should also be investigated, as well as the rise of the water temperature around the implemented UWSN. This implementation requires an experimental recharging BS. In order to maximize the BS efficiency, it would be interesting to develop class-E based switches for the DC-AC inverter block, since the ideal load of class-E PAs is inductive, meaning the TX coil can be easily integrated in the PA architecture. Ideally, in order to minimize the costs, only one RF chain should be used for the power amplification of the proposed harmonic-spaced 2-FSK signal. However, it is a real challenge, since it is quite difficult to implement dual-band class-E PAs with a frequency deviation between the two carriers larger than the lower carrier frequency. Such a topology would be a great contribution to the field, but it is not granted that it can be done (maybe with reconfigurable output load network). In case it cannot be done, the proposed harmonic-spaced FSK could only be implemented with two parallel PA blocks. For the experimental verification of the proposed UD transceiver, the BS does not need to be optimum, but it would be interesting to have a PhD thesis dedicated to that topic as well.

Based on the report presented by the U.S. Department of Energy, reliable UD-assisted UWSN, using ROVs and AUVs, should attend the requirements summarized in Table 3 [84]. Since at PUC-Rio, we lacked the resources to work using such high power and energy densities, this thesis focused on low-power applications based on small commercial UD. For that reason, the CNPq funding for equipment and materials provided to doctoral students were used to buy a ROV for the implementation of small-scale, proof-of-concept only demonstration of the main results of this thesis. The purchased UD, model PowerVision PowerRay, is shown in Figure 6.2. It operates in a depth range up to 30 *m* and its required power is 95 *Wh* only (a little bit more than a conventional laptop).

Table 3: UD-assisted UWSN

<b>Required Energy per BS</b>	<i>60 kWh up to 2 MWh</i>
<b>Transmitted Power</b>	<i>200 W to 500 W</i>
<b>Recharge Time</b>	<i>4 h to 8 h</i>
<b>Operating Depth Range</b>	<i>50 m up to 1 km</i>



Figure 6.2: Purchased UD, PowerVision PowerRay

### 6.3.6

#### **Simultaneous magnetic and electric coupling based power and data transmission system, for underwater applications**

In this work, it was considered only the magnetic-coupling based transmission. Nonetheless, as pointed out by [19], due to the high-dielectric constant of water, electric coupling can be an efficient mechanism for underwater power transmission. Based on that, the advantages and disadvantages of the electric-coupling based power and data transmission systems in underwater applications should be deeply investigated. Furthermore, special attention should be given to possibility of using both couplings simultaneously, electric and magnetic ones, to boost the overall efficiency of the system. A great challenge following this path would be how to conceive MTMs to serve as lenses and reflectors for these both fields simultaneously.

## References

- 1 OECD. **The Ocean Economy in 2030**. Paris: OECD Publishing, 2016.
- 2 ALLARD, Y.; SHAHBAZIAN, E. **Unmanned Underwater Vehicle (UUV) Information Study**. Toronto: OODA Technologies Inc. 2014.
- 3 GILLIS, J. M. The Future of Autonomous Marine Systems in the Canadian Navy. **Canadian Naval Review**, v. 6, n. 4, p. 22-26, 2011.
- 4 DEPARTMENT OF THE NAVY. **The Navy Unmanned Undersea Vehicle(UUV) Master Plan**. US Department of Defense. Washington - DC, p. 55 - 66. 2004.
- 5 ASKARI, A. et al. **Underwater wireless power transfer**. 2015 IEEE Wireless Power Transfer Conference (WPTC). Boulder, CO, USA : IEEE. 2015.
- 6 LIN, M. et al. **Design and analysis of the load adaptive IPT system applied to underwater docking system**. OCEANS 2016 MTS/IEEE Monterey. Monterey, CA, USA : IEEE. 2016.
- 7 SONG, B. et al. Advances in Mechanical Engineering. **Research on wireless power transfersystem for Torpedo autonomous underwater vehicles**, v. 10, n. 9, p. 1 - 8, 2018.
- 8 OILER, J. et al. **Thermal and biofouling effects on underwater wireless power transfer**. 2015 IEEE Wireless Power Transfer Conference (WPTC). Boulder, CO, USA : IEEE. 2015.
- 9 WANG, Y.; SONG, B.; MAO, Z. Application of Shielding Coils in Underwater Wireless Power Transfer Systems. **Journal of Marine Science and Engineering**, v. 7, n. 8, 2019.
- 10 SATO, N.; KIFUNE, H.; KOMEDA, S. A coil layout of wireless power transfer systems based on multicoil arrangement for underwater vehicles. **Electrical Engineering in Japan**, v. 139, n. 1, p. 13-21, 2019.

- 11 ZHANG, K. et al. A New Coil Structure to Reduce Eddy Current Loss of WPT Systems for Underwater Vehicles. **IEEE Transactions on Vehicular Technology**, v. 68, n. 1, p. 245 - 253, 2019.
- 12 HE, Z. et al. **Research on three-dimensional omnidirectional wireless power transfer system for subsea operation**. OCEANS 2017 - Aberdeen. Aberdeen, UK: IEEE. 2017.
- 13 CAI, C. et al. **A strong misalignment tolerance magnetic coupler for autonomous underwater vehicle wireless power transfer system**. 2018 IEEE International Power Electronics and Application Conference and Exposition (PEAC). Shenzhen, China : IEEE. 2018.
- 14 YAN, Z. et al. A Rotation-Free Wireless Power Transfer System With Stable Output Power and Efficiency for Autonomous Underwater Vehicles. **IEEE Transactions on Power Electronics**, v. 34, n. 5, p. 4005 - 4008, 2019.
- 15 KAN, T. et al. A Rotation-Resilient Wireless Charging System for Lightweight Autonomous Underwater Vehicles. **IEEE Transactions on Vehicular Technology**, v. 67, n. 8, p. 6935 - 6942, 2018.
- 16 HASABA, R. et al. **Experimental Study on Underwater Wireless Power Transfer with Degree of Free Position Inside the Coils**. 2019 IEEE Underwater Technology (UT). Kaohsiung, Taiwan: IEEE. 2019.
- 17 CHU, S. et al. Fields and coupling between coils embedded in conductive environments. **EPJ Applied Metamaterials**, v. 5, 2018.
- 18 ZHOU, W. et al. A Wideband Strongly Coupled Magnetic Resonance Wireless Power Transfer System and Its Circuit Analysis. **IEEE Microwave and Wireless Components Letters**, v. 28, n. 12, p. 1152 - 1154, 2018.
- 19 URANO, M.; TAKAHASHI, A. **Study on underwater wireless power transfer via electric coupling**. 2016 IEEE International Meeting for Future of Electron Devices, Kansai (IMFEDK). Kyoto, Japan : IEEE. 2016.

- 20 ALI, M. F. et al. Recent Advances and Future Directions on Underwater Wireless Communications. **Archives of Computational Methods in Engineering**, 31 ago. 2019. 1-34.
- 21 AWAN, K. M. et al. Underwater Wireless Sensor Networks: A Review of Recent Issues and Challenges. **Wireless Communications and Mobile Computing**, v. 2019, n. 6470359, p. 20, 2019.
- 22 GUIDA, R. et al. **An Acoustically Powered Battery-less Internet of Underwater Things Platform**. 2018 4th Underwater Communications and Networking Conference (UComms). Lerici, Italy: IEEE. 2018.
- 23 SONG, K. et al. Sound Pressure Level Gain in an Acoustic Metamaterial Cavity. **Scientific Reports**, v. 4, n. 7421, 2014.
- 24 KHALIGHI, M. et al. **Underwater Wireless Optical Communication: Recent Advances and Remaining Challenges**. 2014 16th International Conference on Transparent Optical Networks (ICTON). Graz, Austria: IEEE. 2014.
- 25 HAYSLETT, T. M.; OREKAN, T.; ZHANG, P. **Underwater Wireless Power transfer for Ocean System Applications**. OCEANS 2016 MTS/IEEE Monterey. Monterey, CA, USA : IEEE. 2016.
- 26 OREKAN, T.; ZHANG, P. Study and Analysis of Underwater Wireless Power Transfer. In: OREKAN, T.; ZHANG, P. **Underwater Wireless Power Transfer: Smart Ocean Energy Converters**. 1. ed. Cham, Switzerland: Springer International Publishing, 2019. Cap. 3, p. 35 - 48.
- 27 DE ALMEIDA, J. V. et al. Mu Negative Metamaterials Seen as Band Limited Non Foster Impedances in Inductive Power Transmission Systems. **Journal of Microwaves, Optoelectronics and Electromagnetic Applications**, v. 18, n. 4, p. 492 - 504, 2019.
- 28 DE ALMEIDA, J. V. et al. A Parametric Study of Inductive SWIPT Systems Assisted by Metamaterial Using Virtual Magnetic TL-Based Channel Modeling. **Journal of Microwaves, Optoelectronics and Electromagnetic Applications (JMoe)**, v. 20, n. 1, p. 195–207, 2021.
- 29 CAPOLINO, F. **Theory and Phenomena of Metamaterials**. [S.l.]: CRC Press, 2009.

- 30 CAPOLINO, F. **Applications of Metamaterials**. [S.l.]: CRC Press, 2009.
- 31 ZIOLKOWSKI, R. W.; ENGHETA, N. **Electromagnetic Metamaterials: Physics and Engineering Explorations**. Piscataway: Wiley-IEEE Press, 2006. 88-91 p.
- 32 VESELAGO, V. G. The Electrodynamics of Substances With Simultaneously Negative Values of Epsilon and Mu. **Soviet Physics Uspekhi**, v. 10, n. 4, 1968.
- 33 CALOZ, C. Metamaterial Dispersion Engineering Concepts and Applications. **Proceedings of the IEEE**, v. 99, n. 10, p. 1711-1719, 2011.
- 34 CHRISTOGEORGOS, O. et al. Extraordinary Directive Emission and Scanning from an Array of Radiation Sources with Hyperuniform Disorder. **Phys. Rev. Applied**, v. 15, n. 1, p. 014062, 2021.
- 35 EKMEKÇI, E.; TURHAN-SAYAN, G. **Investigation of Effective Permittivity and Permeability for a Novel V-shaped Metamaterial using Simulated S-parameters**. 5th International Conference on Electrical and Electronics Engineering. [S.l.]: [s.n.]. 2007.
- 36 DE ARAÚJO, J. B. et al. An Ultrathin and Ultrawideband Metamaterial Absorber and an Equivalent-Circuit Parameter Retrieval Method. **IEEE Transactions on Antennas and Propagation**, v. 68, n. 5, p. 3739 - 3746, 2019.
- 37 DE ALMEIDA, J. V. et al. Experiments on Metamaterials for Sub-wavelength Antenna Insulation at PEC Boundaries. **Microwave and Optical Technology Letters**, v. 59, n. 6, p. 1420–1423, 2017.
- 38 TONG, X. C. **Functional Metamaterials and Metadevices**. [S.l.]: Springer, 2018.
- 39 LI, J. L.-W. **Wireless Power Transmission: State-of-the-Arts in Technologies and Potential Applications**. Proceedings of the Asia-Pacific Microwave Conference. [S.l.]: [s.n.]. 2011.
- 40 COVIC, G. A.; BOYS, J. T. Inductive Power Transfer. **Proceedings of the IEEE**, v. 101, n. 6, p. 1276 - 1289, 2013.

- 41 HARRINGTON, R. F. **Time-Harmonic Electromagnetic Fields**. Piscataway: Wiley-IEEE Press, 2001. 61-66 p.
- 42 HOURAN, M. A.; YANG, X.; CHEN, W. Magnetically Coupled Resonance WPT: Review of Compensation Topologies, Resonator Structures with Misalignment, and EMI Diagnostics. **Electronics**, v. 7, n. 11, p. 296, 2018.
- 43 FOTOPOULOU, K.; FLYNN, B. Inductive Wireless Power Transfer Using Circuit Theory. In: AGBINYA, J. I. **Wireless Power Transfer**. 2. ed. [S.l.]: River Publishers, 2016. Cap. 5, p. 165 - 216.
- 44 KURS, A. et al. Wireless Power Transfer via Strongly Coupled Magnetic Resonances. **Science**, n. 317, p. 87, 2007.
- 45 WEI, X.; WANG, Z.; DAI, H. A Critical Review of Wireless Power Transfer via Strongly Coupled. **Energies**, v. 7, n. 7, p. 4316 - 4341, 2014.
- 46 CORRÊA, D. C.; RESENDE, U. C.; BICALHO, F. S. Experiments With a Compact Wireless Power Transfer System Using Strongly Coupled Magnetic Resonance and Metamaterials. **IEEE Transactions on Magnetism**, v. 55, n. 8, 2019.
- 47 AHN, D.; KIANI, M.; GHOVANLOO, M. Enhanced Wireless Power Transmission Using Strong Paramagnetic Response. **IEEE Transactions on Magnetism**, v. 50, n. 3, 2014.
- 48 CHENG, Z. et al. Design and Loss Analysis of Loosely Coupled Transformer for an Underwater High-Power Inductive Power Transfer System. **IEEE Transactions on Magnetism**, v. 51, n. 7, p. 8401110, 2015.
- 49 SAWAHARA, Y. et al. **Development of Underwater WPT System Independent of Salinity**. 2014 Asia-Pacific Microwave Conference. Sendai, Japan: IEEE. 2014.
- 50 DOU, Y. et al. **Investigation and Design of Wireless Power Transfer System for Autonomous Underwater Vehicle**. 2019 IEEE Applied Power Electronics Conference and Exposition (APEC). Anaheim, CA, USA: IEEE. 2019.

- 51 WANG, Y. et al. An LC/S Compensation Topology and Coil Design Technique for Wireless Power Transfer. **IEEE Transactions on Power Electronics**, v. 33, n. 3, p. 2007 - 2025, 2018.
- 52 YAN, Z. et al. Study of Wireless Power and Information Transmission Technology Based on the Triangular Current Waveform. **IEEE Transactions on Power Electronics**, v. 33, n. 2, p. 1368 - 1377, 2017.
- 53 URZHUMOV, Y.; SMITH, D. R. Metamaterial-enhanced Coupling between Magnetic Dipoles for Efficient Wireless Power Transfer. **Phys. Rev. B**, v. 83, n. 205114, 2011.
- 54 NISHIMURA, S. I. et al. **Enhancing the Inductive Coupling and Efficiency of Wireless Power Transmission System by Using Metamaterials**. 16º SBMO - Simpósio Brasileiro de Micro-ondas e Optoeletrônica e 11º CBMag. Curitiba: MOMAG. 2014.
- 55 WANG, B. et al. **Wireless Power Transfer with Metamaterials**. European Conference on Antennas and Propagation. Rome, Italy: [s.n.]. 2011. p. 3905-3908.
- 56 WU, J. et al. **Wireless Power Transfer with Artificial Magnetic Conductors**. IEEE Wireless Power Transfer Conference. [S.I.]: [s.n.]. 2013.
- 57 KWON, D.-H.; WERNER, D. H. Transformation Electromagnetics: An Overview of the Theory and Applications. **IEEE Antennas and Propagation Magazine**, v. 52, n. 1, p. 24 - 46, 2010.
- 58 BESNOFF, J.; CHABALKO, M.; RICKETTS, D. S. A Frequency-Selective Zero-Permeability Metamaterial Shield for Reduction of Near-Field Electromagnetic Energy. **IEEE Antennas and Wireless Propagation Letters**, v. 15, p. 654 - 657, 2015.
- 59 SOLYMAR, L.; SHAMONINA, E. Magnetoinductive waves I. In: SOLYMAR, L.; SHAMONINA, E. **Waves in Metamaterials**. London, U.K.: Oxford Univ. Press, 2009. Cap. 7.
- 60 SOLYMAR, L.; SHAMONINA, E. Magnetoinductive waves II. In: SOLYMAR, L.; SHAMONINA, E. **Waves in Metamaterials**. London, U.K.: Oxford Univ. Press, 2009. Cap. 8.

- 61 DE ALMEIDA, J. V.; FEITOZA, R. S. Metamaterial-Enhanced Magnetic Coupling: An Inductive Wireless Power Transmission System Assisted by Metamaterial-Based Mu-Negative Lenses. **IEEE Microwave Magazine**, v. 19, n. 4, p. 95 - 100, 2018.
- 62 CHU, S. et al. **Analytical Solution for the Magnetic Coupling of Two Coils Immersed in a Conductive Medium**. 2017 11th International Congress on Engineered Materials Platforms for Novel Wave Phenomena (Metamaterials). Marseille, France: IEEE. 2017.
- 63 LIU, F. et al. Propagation Modeling of Point Source Excited Magnetoinductive Waves Based on a New Plane Wave Expansion Approach. **Mathematical Problems in Engineering**, v. 2015, n. 951718, p. 9, 2015.
- 64 IORDACHE, M.; DUMITRIU, L.; NICULAE, D. Power Transfer by Magnetic Induction Using Coupled-Mode Theory. In: AGBINYA, J. I. **Wireless Power Transfer**. 2. ed. [S.l.]: River Publishers, 2016. Cap. 1, p. 1 - 72.
- 65 MEI, H. et al. Design, Analysis, and Optimization of Magnetic Resonant Coupling Wireless Power Transfer Systems Using Bandpass Filter Theory. In: AGBINYA, J. I. **Wireless Power Transfer**. 2. ed. [S.l.]: River Publishers, 2016. Cap. 16, p. 543 - 586.
- 66 BAGCHI, A. C. et al. **Small-Signal Phasor Modeling of an Underwater IPT System in Constant Current Distribution**. 2019 IEEE Applied Power Electronics Conference and Exposition (APEC). Anaheim, CA, USA: IEEE. 2019.
- 67 ARAKAWA, T. et al. Optimizing Wireless Power Transfer From Multiple Transmit Coils. **IEEE Access**, v. 6, p. 23828 - 23838, 2018.
- 68 DE ALMEIDA, J. V. Virtual Magnetic Transmission Lines, Rio de Janeiro, RJ, M.Sc. Eng. thesis, Pontifical Catholic Univ. Rio de Janeiro, Rio de Janeiro, Brazil, 2017.
- 69 HAMILL, D. C. Lumped Equivalent Circuits of Magnetic Components: The Gyrator-Capacitor Approach. **IEEE Transactions on Power Electronics**, v. 8, n. 2, p. 97 - 103, 1993.

- 70 FARIA, J. A. B.; PIRES, M. P. Theory of Magnetic Transmission Lines. **IEEE Transactions on Microwave Theory and Techniques**, v. 60, n. 10, p. 2941 - 2949, 2012.
- 71 BALANIS, C. A. **Antenna Design Theory**. Hoboken, New Jersey: John Wiley & Sons, Inc, 2005.
- 72 DUARTE, R. M.; FELIC, G. K. Analysis of the Coupling Coefficient in Inductive Energy Transfer Systems. **Active and Passive Electronic Components**, 2014, Article ID 951624, 6 pages, 2014.
- 73 GAO, J. Traveling Magnetic Field for Homogeneous Wireless Power Transmission. **IEEE Transactions on Power Delivery**, v. 22, n. 1, p. 507, 2007.
- 74 GADANI, D. H. et al. Effects of Salinity on the Properties of Water. **Indian Journal of Pure & Applied Physics**, v. 50, p. 405-410, 2012.
- 75 BERGMAN, J. Windows to the Universe, 16 fev. 2011. Disponível em: <<https://www.windows2universe.org/earth/Water/temp.html>>. Acesso em: 01 jan. 2021.
- 76 ZHENG, Z. et al. Three-stage Vertical Distribution of Seawater Conductivity. **Scientific Reports**, v. 8, n. Article number: 9916, 2018.
- 77 BILOTTI, F.; TOSCANO, A.; VEGNI, L. Design of Spiral and Multiple Split-Ring Resonators for the Realization of Miniaturized Metamaterial Samples. **IEEE Transactions on Antennas and Propagation**, v. 55, n. 8, p. 2258 - 2265, 2007.
- 78 CHO, Y. et al. Thin Hybrid Metamaterial Slab With Negative and Zero Permeability for High Efficiency and Low Electromagnetic Field in Wireless Power Transfer Systems. **IEEE Transactions on Electromagnetic Compatibility**, v. 60, n. 4, p. 1001-1009, 2018.
- 79 KIM, D. W. Society for Underwater Technology - 2019 AUT Conference, 23 out. 2019. Disponível em: <[https://www.sut.org/wp-content/uploads/2018/06/Dowon-Kim-v2-2019\\_AUT\\_Conference\\_Revised.pdf](https://www.sut.org/wp-content/uploads/2018/06/Dowon-Kim-v2-2019_AUT_Conference_Revised.pdf)>. Acesso em: 01 fev. 2021.
- 80 GREBENNIKOV et al. **Switchmode RF and Microwave Power Amplifiers**. [S.l.]: Academic Press, 2012.

- 81 SKLAR, B.; HARRIS, F. **Digital communications: Fundamentals and Applications.** [S.I.]: Prentice Hall, 2017.
- 82 OREKAN, T.; ZHANG, P. Future Research. In: OREKAN, T.; ZHANG, P. **Underwater Wireless Power Transfer: Smart Ocean Energy Converters.** 1. ed. Cham, Switzerland: Springer International Publishing, 2019. Cap. 6, p. 93 - 97.
- 83 TAUB, H.; SCHILLING, D. L. **Principles of Communication Systems.** [S.I.]: McGraw-Hill, 1986.
- 84 LIVECCHI et al. **Powering the Blue Economy: Exploring Opportunities for Marine Renewable Energy in Maritime Markets.** Washington, D.C. 2019.

## A

### Published and accepted papers

The following scientific works were published during the realization of this thesis:

#### a) Journals

- ✓ DE ALMEIDA, J. V. et al. A Parametric Study of Inductive SWIPT Systems Assisted by Metamaterial using Virtual Magnetic TL-based Channel Modeling. **Journal of Microwaves, Optoelectronics and Electromagnetic Applications**, v. 20, n. 1, p. 195 - 207, 2021.
- ✓ DE ALMEIDA, J. V. et al. Mu Negative Metamaterials Seen as Band Limited Non-Foster Impedances in Inductive Power Transmission Systems. **Journal of Microwaves, Optoelectronics and Electromagnetic Applications**, v. 18, n. 4, p. 492 - 504, 2019.

#### b) Magazine

- ✓ DE ALMEIDA, J. V.; FEITOZA, R. S. Metamaterial-Enhanced Magnetic Coupling: An Inductive Wireless Power Transmission System Assisted by Metamaterial-Based Mu-Negative Lenses. **IEEE Microwave Magazine**, v. 19, n. 4, p. 95 - 100, 2018.

**c) Conference proceedings**

- ✓ DE ALMEIDA, J. V. et al. **Virtual Magnetic TL-based Channel Modeling of SWIPT Systems assisted by MTMs**. 19<sup>o</sup> SBMO - Simpósio Brasileiro de Micro-ondas e Optoeletrônica e 14<sup>o</sup> CBMag. Niterói: MOMAG. 2020.
  
- ✓ DE ALMEIDA, J. V. et al. **Effects on the antenna's radiation pattern due to metamaterial-based sub-wavelength insulation**. 2017 IEEE 3rd Global Electromagnetic Compatibility Conference (GEMCCON), 2017, Sao Paulo - Brazil. 2017 IEEE 3rd Global Electromagnetic Compatibility Conference (GEMCCON), 2017. p. 1.
  
- ✓ DE ALMEIDA, J. V. et al. **Mu-negative metamaterials seen as band-limited non-Foster impedances for magnetic coupled systems**. Meta'17 - The 8th International Conference on Metamaterials, Photonic Crystals and Plasmonics, 2017, Incheon - Korea. Meta'17 Conference Proceedings, 2017.

The following scientific work was accepted for the 11th International Conference on Metamaterials, Photonic Crystals and Plasmonics (Meta'21), to be held in Warsaw - Poland, in July 2021:

- ✓ DE ALMEIDA, J. V. et al. **Metamaterial-assisted Inductive Power Transfer using Transmission-Line Mode**. Meta'21 - the 11th International Conference on Metamaterials, Photonic Crystals and Plasmonics, 2021, Warsaw - Poland.

**B****Student design competition award**

During the realization of this thesis, one of the IPT prototypes conceived at PUC-Rio received the **First Place Award in Student Design Competition for Wireless Power Transmission Consumer Electronics Application**, from IEEE Microwave Theory and Technique Society (MTT) at the 2017 International Microwave Symposium (IMS 2017) held in Hawaii – USA. The results regarding this prototype were summarized in the following publication:

- ✓ DE ALMEIDA, J. V.; FEITOZA, R. S. Metamaterial-Enhanced Magnetic Coupling: An Inductive Wireless Power Transmission System Assisted by Metamaterial-Based Mu-Negative Lenses. **IEEE Microwave Magazine**, v. 19, n. 4, p. 95 - 100, 2018.

## C

### MATLAB code

The following MATLAB code that was used to obtain the results presented in section 3.3:

```

%% Initialization
clc
clear all
close all

%% Constants
eps0=8.854e-12;
mu0=4*pi*1e-7;
z0=sqrt(mu0/eps0);
c0=1/sqrt(mu0*eps0);
sigmacopper=5.8*1e7;

%% MTM characteristics
N1=1; %Number of slabs (integer starting at zero)
f0=32*1e6; %operating frequency
F=-0.43; %Coupling coefficient between unit-cells, F is negative because the cells are co-planar
Q=100; %Quality Factor
a=2.3e-2; %Cell period

%% Simulation's parameters
syms Vm Im Rm Ce Gm Le km w

rv = [4 5 6]; %Radius of the drivers in cm
L0=620*1e-9; %Drivers' coil self-inductance
C0=0.28*1e-12; %Drivers' coil self-capacitance
Gm=0; %Magnetic conductance of the TL
Ge=0;

f=[1:0.1:50]*1e6; %Frequency range

figure
%% Transfer Function
for p=1:1:size(rv,2)
r=rv(p)*1e-2;
w=2*pi*f;

d12=16*1e-2;

Le=L0./d12;
Ce=C0./d12;
M12=-mu0*pi*(r.^4)./sqrt(4*(r.^2)+(d12.^2))./d12.^2;
km=M12/L0;
Rm=abs(1./M12/(r^2));

```

```
kmMTM=2*km; %Approximation of the coupling between the MTMs and the drivers
```

```
s=d12/(N1+1); % case when MTMs get coupled
```

```
if s<a
```

```
w0=2*pi*f0/sqrt(N1);
```

```
else
```

```
w0=2*pi*f0;
```

```
end
```

```
LMTM=mu0*(1+(F*w.^2)./(w0.^2-w.^2-j*w*w0/Q)); % distributed inductance
```

```
ZMTM=j*w.*LMTM;
```

```
Zm=Rm./j./w+j.*w.*Ce.*km.^2+Ge.*km.^2;
```

```
Ym=Gm.*km.^2+j.*w.*Le.*km.^2+N1*ZMTM.*kmMTM^2;
```

```
Z0m=sqrt(Zm./Ym); %siemens
```

```
gammam=sqrt(Ym.*Zm); %rad/meter
```

```
alpha=real(gammam); %nepster/meter
```

```
beta=imag(gammam); %rad/meter
```

```
ZTX=50+j*w*L0; %impedance of the TX
```

```
ZL=50+j*w*L0;%impedance of the RX
```

```
S11=(ZL-1./Z0m)./(1./Z0m+ZL);
```

```
VSWR=(1+abs(S11))./(1-abs(S11));
```

```
H=exp(-gammam.*d12).*(1-S11)./(1-S11.*exp(-2*gammam.*d12));
```

```
%
```

```
Im1=1; %at d=-d12, input current
```

```
Im2=Im1.*exp(-gammam.*d12)./(1+S11.*exp(-2*gammam.*d12)); %output current
```

```
Vm1=Im1./Z0m;
```

```
Vm2=Vm1.*exp(-gammam.*d12)./(1-S11.*exp(-2*gammam.*d12));
```

```
PIN=abs((Im1.^2)./ZTX)/2;
```

```
POUT=(abs(H).^2).*real(ZL);
```

```
plot(f*1e-6,10*log10(abs(H)), 'linewidth',2) %Module
```

```
ylabel('Transfer Function (dB)')
```

```
xlabel('freq (MHz)')
```

```
set(gca,'fontsize',14)
```

```
axis([1 50 -60 -25])
```

```
hold on
```

```
PIN=0
```

```
POUT=0;
```

```
Zm=0;
```

```
Ym=0;
```

```
Z0m=0;
```

```
H=0;
```

```
end
```

```
figure
```

```
%% VMGTL Alpha
```

```
for p=1:size(rv,2)
```

```
r=rv(p)*1e-2;
```

```
w=2*pi*f;
```

```

d12=16*1e-2;

Le=L0./d12;
Ce=C0./d12;
M12=-mu0*pi*(r.^4)./sqrt(4*(r.^2)+(d12.^2))./d12.^2;
km=M12/L0;
Rm=abs(1./M12/(r.^2));

kmMTM=2*km; %Approximation of the coupling between the MTMs and the drivers

s=d12/(N1+1); % case when MTMs get coupled
if s<a
w0=2*pi*f0/sqrt(N1);
else
w0=2*pi*f0;
end

LMTM=mu0*(1+(F*w.^2)./(w0.^2-w.^2-j*w*W0/Q));
ZMTM=j*w.*LMTM;

Zm=Rm./j./w+j.*w.*Ce.*km.^2+Ge.*km.^2;
Ym=Gm.*km.^2+j.*w.*Le.*km.^2+N1*ZMTM.*kmMTM.^2;

Z0m=sqrt(Zm./Ym); %siemens
gammam=sqrt(Ym.*Zm); %rad/meter
alpha=real(gammam); %nepster/meter
beta=imag(gammam); %rad/meter

ZTX=50+j*w*L0; %impedance of the TX
ZL=50+j*w*L0;%impedance of the RX

S11=(ZL-1./Z0m)./(1./Z0m+ZL);
VSWR=(1+abs(S11))./(1-abs(S11));

H=exp(-gammam.*d12).*(1-S11)./(1-S11.*exp(-2*gammam.*d12));

%
Im1=1; %at d=-d12, input current
Im2=Im1.*exp(-gammam.*d12)./(1+S11.*exp(-2*gammam.*d12)); %output current

Vm1=Im1./Z0m;
Vm2=Vm1.*exp(-gammam.*d12)./(1-S11.*exp(-2*gammam.*d12));

PIN=abs((Im1.^2)./ZTX)/2;
POUT=(abs(H).^2).*real(ZL);

plot(f*1e-6,alpha,'linewidth',2)
ylabel('Attenuation Constant (Np/m)')
xlabel('freq (MHz)')
set(gca,'fontsize',14)
hold on
end

figure
%% VMGTL Beta
for p=1:1:size(rv,2)
r=rv(p)*1e-2;
w=2*pi*f;

```

```

d12=16*1e-2;

Le=L0./d12;
Ce=C0./d12;
M12=-mu0*pi*(r.^4)./sqrt(4*(r.^2)+(d12.^2))./d12.^2;
km=M12/L0;
Rm=abs(1./M12/(r.^2));

kmMTM=2*km; %Approximation of the coupling between the MTMs and the drivers

s=d12/(N1+1); % case when MTMs get coupled
if s<a
w0=2*pi*f0/sqrt(N1);
else
w0=2*pi*f0;
end

LMTM=mu0*(1+(F*w.^2)./(w0.^2-w.^2-j*w*W0/Q));
ZMTM=j*w.*LMTM;

Zm=Rm./j./w+j.*w.*Ce.*km.^2+Ge.*km.^2;
Ym=Gm.*km.^2+j.*w.*Le.*km.^2+N1*ZMTM.*kmMTM.^2;

Z0m=sqrt(Zm./Ym); %siemens
gammam=sqrt(Ym.*Zm); %rad/meter
alpha=real(gammam); %nepster/meter
beta=imag(gammam); %rad/meter

ZTX=50+j*w*L0; %impedance of the TX
ZL=50+j*w*L0;%impedance of the RX

S11=(ZL-1./Z0m)./(1./Z0m+ZL);
VSWR=(1+abs(S11))./(1-abs(S11));

H=exp(-gammam.*d12).*(1-S11)./(1-S11.*exp(-2*gammam.*d12));

%
Im1=1; %at d=-d12, input current
Im2=Im1.*exp(-gammam.*d12)./(1+S11.*exp(-2*gammam.*d12)); %output current

Vm1=Im1./Z0m;
Vm2=Vm1.*exp(-gammam.*d12)./(1-S11.*exp(-2*gammam.*d12));

PIN=abs((Im1.^2)./ZTX)/2;
POUT=(abs(H).^2).*real(ZL);

plot(f*1e-6,beta,'linewidth',2)
ylabel('Propagation Constant (rad/m)')
xlabel('freq (MHz)')
set(gca,'fontsize',14)
hold on

end

%% Simulation with no MTM

N1=0;
figure

```

```

%% Transfer Function
for p=1:1:size(rv,2)
r=rv(p)*1e-2;
w=2*pi*f;

d12=16*1e-2;

Le=L0./d12;
Ce=C0./d12;
M12=-mu0*pi*(r.^4)./sqrt(4*(r.^2)+(d12.^2))./d12.^2;
km=M12/L0;
Rm=abs(1./M12/(r^2));

kmMTM=2*km; %Approximation of the coupling between the MTMs and the drivers

s=d12/(N1+1); % case when MTMs get coupled
if s<a
w0=2*pi*f0/sqrt(N1);
else
w0=2*pi*f0;
end

LMTM=mu0*(1+(F*w.^2)./(w0.^2-w.^2-j*w*w0/Q)); % distributed inductance
ZMTM=j*w.*LMTM;

Zm=Rm./j./w+j.*w.*Ce.*km.^2+Ge.*km.^2;
Ym=Gm.*km.^2+j.*w.*Le.*km.^2+N1*ZMTM.*kmMTM^2;

Z0m=sqrt(Zm./Ym); %siemens
gammam=sqrt(Ym.*Zm); %rad/meter
alpha=real(gammam); %nepster/meter
beta=imag(gammam); %rad/meter

ZTX=50+j*w*L0; %impedance of the TX
ZL=50+j*w*L0;%impedance of the RX

S11=(ZL-1./Z0m)./(1./Z0m+ZL);
VSWR=(1+abs(S11))./(1-abs(S11));

H=exp(-gammam.*d12).*(1-S11)./(1-S11.*exp(-2*gammam.*d12));

%
Im1=1; %at d=-d12, input current
Im2=Im1.*exp(-gammam.*d12)./(1+S11.*exp(-2*gammam.*d12)); %output current

Vm1=Im1./Z0m;
Vm2=Vm1.*exp(-gammam.*d12)./(1-S11.*exp(-2*gammam.*d12));

PIN=abs((Im1.^2)./ZTX)/2;
POUT=(abs(H).^2).*real(ZL);

plot(f*1e-6,10*log10(abs(H)),'linewidth',2) %Module
ylabel('Transfer Function (dB)')
xlabel('freq (MHz)')
set(gca,'fontsize',14)
axis([1 50 -60 -35])
hold on
end

```

```

figure
%% VMGTL Alpha
for p=1:1:size(rv,2)
r=rv(p)*1e-2;
w=2*pi*f;

d12=16*1e-2;

Le=L0./d12;
Ce=C0./d12;
M12=-mu0*pi*(r.^4)./sqrt(4*(r.^2)+(d12.^2))./d12.^2;
km=M12/L0;
Rm=abs(1./M12/(r^2));

kmMTM=2*km; %Approximation of the coupling between the MTMs and the drivers

s=d12/(N1+1); % case when MTMs get coupled
if s<a
w0=2*pi*f0/sqrt(N1);
else
w0=2*pi*f0;
end

LMTM=mu0*(1+(F*w.^2)./(w0.^2-w.^2-j*w*w0/Q));
ZMTM=j*w.*LMTM;

Zm=Rm./j./w+j.*w.*Ce.*km.^2+Ge.*km.^2;
Ym=Gm.*km.^2+j.*w.*Le.*km.^2+N1*ZMTM.*kmMTM.^2;

Z0m=sqrt(Zm./Ym); %siemens
gammam=sqrt(Ym.*Zm); %rad/meter
alpha=real(gammam); %nepster/meter
beta=imag(gammam); %rad/meter

ZTX=50+j*w*L0; %impedance of the TX
ZL=50+j*w*L0;%impedance of the RX

S11=(ZL-1./Z0m)./(1./Z0m+ZL);
VSWR=(1+abs(S11))./(1-abs(S11));

H=exp(-gammam.*d12).*(1-S11)./(1-S11.*exp(-2*gammam.*d12));

%
Im1=1; %at d=-d12, input current
Im2=Im1.*exp(-gammam.*d12)./(1+S11.*exp(-2*gammam.*d12)); %output current

Vm1=Im1./Z0m;
Vm2=Vm1.*exp(-gammam.*d12)./(1-S11.*exp(-2*gammam.*d12));

PIN=abs((Im1.^2)./ZTX)/2;
POUT=(abs(H).^2).*real(ZL);

plot(f*1e-6,alpha,'linewidth',2)
ylabel('Attenuation Constant (Np/m)')
xlabel('freq (MHz)')
set(gca,'fontsize',14)
hold on
end

```

```

figure
%% VMGTL Beta
for p=1:1:size(rv,2)
r=rv(p)*1e-2;
w=2*pi*f;

d12=16*1e-2;

Le=L0./d12;
Ce=C0./d12;
M12=-mu0*pi*(r.^4)./sqrt(4*(r.^2)+(d12.^2))./d12.^2;
km=M12/L0;
Rm=abs(1./M12/(r^2));

kmMTM=2*km; %Approximation of the coupling between the MTMs and the drivers

s=d12/(N1+1); % case when MTMs get coupled
if s<a
w0=2*pi*f0/sqrt(N1);
else
w0=2*pi*f0;
end

LMTM=mu0*(1+(F*w.^2)./(w0.^2-w.^2-j*w*W0/Q));
ZMTM=j*w.*LMTM;

Zm=Rm./j./w+j.*w.*Ce.*km.^2+Ge.*km.^2;
Ym=Gm.*km.^2+j.*w.*Le.*km.^2+N1*ZMTM.*kmMTM.^2;

Z0m=sqrt(Zm./Ym); %siemens
gammam=sqrt(Ym.*Zm); %rad/meter
alpha=real(gammam); %nepster/meter
beta=imag(gammam); %rad/meter

ZTX=50+j*w*L0; %impedance of the TX
ZL=50+j*w*L0;%impedance of the RX

S11=(ZL-1./Z0m)./(1./Z0m+ZL);
VSWR=(1+abs(S11))./(1-abs(S11));

H=exp(-gammam.*d12).*(1-S11)./(1-S11.*exp(-2*gammam.*d12));

%
Im1=1; %at d=-d12, input current
Im2=Im1.*exp(-gammam.*d12)./(1+S11.*exp(-2*gammam.*d12)); %output current

Vm1=Im1./Z0m;
Vm2=Vm1.*exp(-gammam.*d12)./(1-S11.*exp(-2*gammam.*d12));

PIN=abs((Im1.^2)./ZTX)/2;
POUT=(abs(H).^2).*real(ZL);

plot(f*1e-6,beta,'linewidth',2)
ylabel('Propagation Constant (rad/m)')
xlabel('freq (MHz)')
set(gca,'fontsize',14)
hold on

end

```